Novel electronic and optoelectronic interactions in two-dimensional materials

Thesis by

Duxing Hao

In Partial Fulfillment of the Requirements for

the degree of

Doctor of Philosophy

CALIFORNIA INSTITUTE OF TECHNOLOGY

Pasadena, California

2025

(Defended May 16th, 2025)

Duxing Hao
ORCID: 0000-0002-8907-9776

ACKNOWLEDGEMENTS

In the summer of 2016, after two years of algebra, analysis, o(p)de, analytic physics courses, I nearly burnt out as a physics sophomore student wishing to work on experimental sciences, stretching my head with equations, problem sets and exams every day. At the time, the course *Introduction to nanoscience and technology* taught by Professor Nai-Chang Yeh enlightened me and showed me to the beautiful quantum world built by nanoscience and technology. Although it was as short as two weeks of a crash course, it refueled me with confidence, and more importantly, motivation for nanoscience and quantum world. Magically inspired by the motivation following hard work in the junior year, those equations and matrices that made no sense to me before, suddenly interconnected with each other, and the motivation was so strong that I went over the algebra textbook – which I slept over for most of the sophomore semester in the early morning – twice in the quantum mechanics and statistical mechanics courses. For the first time I felt I could touch and interwind all that knowledge along the central line of nanotechnology and quantum science, and self-motivated to join the Yeh group as visiting summer students one year later.

The journey of an experimental condensed matter physicist began in 2018, I had never absorbed knowledge as quickly and broadly as before. As an experimental physicist, I started with an instrumentation project with optical components, vacuum systems and cryogenic systems, where I started to learn fundamentals of optical components, vacuum and cryogenic technology. With the designed parts, I transited into a role of mechanical engineer and machined those parts with my own hands at the machine shop. Later in my first year and mainly towards my second year, I started to become a material scientist specializing in graphene growth and electrical engineering by working in electrical circuit design and electrical transport measurements. After the pandemic, I formally entered the new world of nanoscience by actively fabricating nanoscale devices at the Kavli nanoscience institute and once one of the heaviest users of the year. After another two years of cryogenic electrical transport measurements, I revolutionized myself again, recharged with capability of Python-coding and combining the knowledge of optics, becoming a designer and principal software engineer for the cryogenic scanning photocurrent spectroscopy setup for structured light-matter interactions.

All those broad exposures of techniques ensure a fruitful deep dive in scientific problems, and all along, I'd like to give my sincere thanks to my advisor, Professor Nai-Chang Yeh for her invaluable advice, tireless dedication and heartfelt support along this journey. It had never been a smooth and

unobscured road to any science problems. Twists, turns, pits and falls along the way. Without her tremendous support, I would not be able to travel this long journey and finish this thesis. We spent countless hours together discussing fresh data, technical details, and setbackss. Her insights had always been helpful and the emerging passion, endless enthusiasm for science behind the discussion always inspires and drives me further. Thank you for allowing me for freedom of occasional crazy ideas and navigate me through the blind spots.

I'd also like to thank the Yeh group members. Chen-Chih Hsu, Dr. Marcus Teague, Jiaqing Wang, you were excellent mentors. My close collaborators who provided valuable insights and helped over the experimental studies: Dr. Wen-Hao Chang (and his two lovely kids), Akiyoshi Park (and his newborn baby) and Chen-Hsuan Lu. My office mates who we shared not only scientific but also philosophical ideas and more important, up and downs, happiness and joy – Adrian llanos, Deepan Kishore Kumar, Jacob Bagley, and Dr. Wen-Hao Chang. My diligent and resourceful fellow staff scientists and lab members: Dr. David Boyd, Wei-Hsiang Lin, Chien-Chang Chen, Daniel Anderson and Jen-Te Chang. And our kind administrative supporter, Loly Ekmekjian for her consistent support and kindness. I'd like to thank the wonderful mentees I worked with over the SURF/VURP program at Caltech, Mai H. Nguyen, Yinan Chen, Siyuan Qiu, Ziqi Sun and Beining Rao. It had always been a pleasure to work with you and thank you for being motivated, diligent and always enthusiastic over the programs.

I had benefited a lot from my collaborators. I'd like to thank Professor Yann-Wen Lan and Professor Ting-Hua Lu for their dedicated support and insightful discussions; Yu-Chen Chang, Hector Chang, and Ye-Ru Chen for collaboration over the MoS_2 and PCS projects; Professor Patrick A. Lee, and Dr. Cyprian Lewandowski for useful discussion and theoretical ideas about graphene strain-engineering.

No research group alone can retain specialized knowledge and experiences for all fields, and therefore I really appreciate the community at Caltech, where a broad range of the brightest scientists and experienced engineers collaborate warmly. Those include my thesis advisory committee members in addition to my advisor, Professor David Hsieh, Professor Jason Alicea, Professor Patrick A. Lee. Thank you for providing detailed feedback over the years and especially thanks to Professor Patrick A. Lee for providing theoretical insights into the graphene projects. I'd like to thank Professor George R. Rossman for sharing both the setup and insights on Raman spectroscopy and photoluminescence spectroscopy experiments. For the work at Kavli nanoscience institute, I'd like to thank Dr. Guy A.

DeRose for dedicated help during my membership at the KNI, especially providing training to the best quality over the hardest months during pandemic; Alex Wertheim, you had great knowledge of deposition, sputtering systems, AFM, 3D printing, tea and coffee; Bert M. Mendoza, the ever-reliable "KNI daddy" for taking care of optical lithography and all the supporting tools and essential for daily running; Alireza Ghafari, kind and warmful support for SEMs, optical lithography knowledge and offering me TA-ship support in his course; Annalena Wolf, thank you for resourceful support and guidance with the SEM and FIB systems; Nathan S. Lee, your thorough introduction to the reactive ion etching system and continued lab support made a lasting difference; Kelly McKenzie, thank you for creative ideas to resolve complex etching problems in within limited selection of gas using RIE systems; Tiffany Kimoto and Sydney Garstang, thank you for administrative support and most importantly, building and maintaining the powerful community around the center of nanofabrication, where mouth to mouth tricks, shortcuts and recipes saves countless research hours. For the cryogenic transport measurement, I'd like to thank Professor Daniel M. Silevitch, Stevephen Armstrong and Christopher Tang from the Presidential Professor Rosenbaum's group for sharing tremendous amounts of valuable information, tools and direct help over customized cryogenic systems and probes, PPMS and electrical transport measurement always in a timely manner whenever I needed. I'd like to thank insightful opinions and suggestions by Professor Michael L. Roukes and Professor Kenneth G. Libbrecht over low-level measurement circuits. I'd like to thank Dr. Alan P. Rice and Joe Benson for providing training and supervision over the machine shop projects. I'd like to thank Mika Walton, Nam K. Ung, Laura Flower Kim and Daniel S. Yolder for consistent support and administrative effort during the entire physics graduate program.

I feel extremely lucky to have the smartest and friendliest cohort. I'd like to thank Xuejian Shen, Yiran Zhang, Chirstina Wang, Lue Wu, Jiajing Mao, Fukang She, Tianqing Zhang, Hengyu Li for heartfelt support over the years, where everyday laughter was multiplied, and sorrow was divided. I'd like to thank Akiyoshi Park, Adrain llanos, Deepan Kishore Kumar, Stephen Armstrong, for deep philosophical and intercultural discussions, especially for Adrian and Stepehen, who helped me the come cross the period of cultural shock by kindly answering tons of how-to questions about almost every aspect of life in the U.S. It had been a great pleasure to journey together with Haoyu Li, Tian Xie, Yuchun Sun, Tianzhe Xie, Yuchen Han, Yihong Huang, Chen Li, Junyi Shan, Ding Zhong, Xiang Li, Ruizhi Cao, Jieyu Zheng, Yalu Chen, Yuelin Shi, Canran Wang, Yunqing Wang, Yinan Chen, Kaiwen Luo, Junxuan Shen, Alex Buser, Yulu Cao, Enze Zhang throughout the years of Ph.D.

Finally, I'd like to thank my family, who support me and always witness my growth. To my parents, paternal grandparents whom I have not seen in person for five years during and past the pandemic, thank you all for unconditionally support and affirmation that kept me going after novelty and creativity, and encouraged me and cheered me when failures fe;;. To my maternal grandparents that witness those in above, thank you for raising me and supporting me over the years. And for Yachun, thank you for bringing love, care and courage to journey forward.

ABSTRACT

Two-dimensional (2D) materials host a rich set of emerging physical phenomena such as superconductivity, ferroelectricity, quantum magnetism, and circular dichroism. Moreover, these phenomena are highly tunable by crystalline composition variations and crystalline structural phase modifications and are sensitive to external conditions such as temperature, magnetic field and optical excitation, substrate and gate tuning. Therefore, 2D material-based devices are highly desirable for modern electronic and optoelectronic devices applications. In this thesis, we employed a fully scalable approach to synthesize materials and fabricate 2D material-based devices such as those based on graphene and 1H-Molybdenum disulfide (1H-MoS_2), and explore their electronic and optoelectronic properties in cryogenic conditions under various excitation sources, such as external magnetic field and structured light.

In the first part of the thesis (Chapters 2 and 3), we provide experimental details for achieving nanoscale strain engineering of monolayer (ML)-graphene and demonstrate that periodic patterns of nanoscale strain distributions in ML-graphene can lead to local giant pseudomagnetic fields as well as global modifications to the electronic properties of ML-graphene, including strain-induced valley Hall and anomalous Hall effects in the absence of external magnetic fields, nonlocal valley-polarized currents and evidence of quantum valley Hall effect under external magnetic field. These findings suggest new approaches towards developing emerging quantum states with tunable electronic correlation based on graphene straintronics.

The second part of the thesis (Chapters 4 and 5) focus more on the semiconducting monolayer transition metal dichalcogenides (ML-TMDs), whose broken inversion symmetry and strong spin-orbit coupling result in spin-valley lock-in effects so that the valley degeneracy may be lifted by external magnetic fields, potentially leading to real-space structural transformation.

In Chapter 4, we report magnetic field (B)-induced giant electric hysteretic responses to back-gate voltages in ML-MoS_2 field-effect transistors (FETs) on SiO_2/Si at temperatures < 20 K. The observed hysteresis increases with $|B|$ up to 12 T and is tunable by varying the temperature. Raman spectroscopic and scanning tunneling microscopic studies reveal significant lattice expansion with increasing $|B|$ at 4.2 K, and this lattice expansion becomes asymmetric in ML-MoS_2 FETs on rigid SiO_2/Si substrates, leading to out-of-plane mirror symmetry breaking and the emergence of a tunable

out-of-plane ferroelectric-like polar order. This broken symmetry-induced polarization in ML-MoS_2 shows typical ferroelectric butterfly hysteresis in piezo-response force microscopy, adding ML-MoS_2 to the single-layer material family that exhibit out-of-plane polar order-induced ferroelectricity, which is promising for such technological applications as cryo-temperature ultracompact non-volatile memories, memtransistors, and ultrasensitive magnetic field sensors. Moreover, the polar effect induced by asymmetric lattice expansion may be further generalized to other ML-TMDs and achieved by nanoscale strain engineering of the substrate without magnetic fields.

In Chapter 5, we further demonstrate the design and application of a novel instrument that integrates scanning spectroscopic photocurrent measurements with structured light of controlled spin and orbital angular momentum. For structured photons with wavelengths between 500 nm to 700 nm, this instrument can perform spatially resolved photocurrent measurements of 2D materials or thin crystals under magnetic fields up to ±14 Tesla, at temperatures from 300 K down to 3 K, with either spin angular momentum (SAM) $\ell\hbar$ or orbital angular momentum (OAM) $\pm \ell\hbar$ (where $\ell = 1, 2, 3\ldots$ is the topological charge), and over a (35 ×25) μm^2 area with ~ 1 μm spatial resolution. These capabilities of the instrument are exemplified by magneto-photocurrent spectroscopic measurements of monolayer 2H-MoS_2 field-effect transistors, which not only reveal the excitonic spectra but also demonstrate monotonically increasing photocurrents with increasing $|\ell|$ as well as excitonic Zeeman splitting and an enhanced Landé g-factor due to the enhanced formation of intervalley dark excitons under magnetic field. These studies thus demonstrate the versatility of the scanning photocurrent spectrometry for investigating excitonic physics, optical selection rules, and optoelectronic responses of novel quantum materials and engineered quantum devices to structured light.

Finally, we summarize the research accomplishments of this thesis work in Chapter 6 and discuss the outlook for new research directions associated with these 2D quantum materials.

PUBLISHED CONTENT AND CONTRIBUTIONS

Hao, Duxing, Chun-I Lu, Ziqi Sun, Yu-Chen Chang, Wen-Hao Chang, Ye-Ru Chen, Akiyoshi park et al. "Cryogenic scanning photocurrent spectroscopy for materials responses to structured optical fields". Under review at Review of Scientific Instruments. 2025.
D.H. conceived the idea of the experiment together with N.-C.Y., Y.-W.L., T.-H.L., and C.-I.L. D.H. and C.-I.L. designed instrument hardware. D.H., C.-I.L., A.P. and S.Q. fabricated the instrument. D.H. led and implemented the software development of the instrument. D.H. carried out room temperature and cryogenic calibration and experiment on ML-MoS_2 FET with assistance from W.-H.C., Z.S., and B.R., D.H. led and implemented formal data analysis and visualization. D.H. and N.-C.Y. wrote the first draft and final version of the paper with input from all other authors.

Hao, Duxing*, Wen-Hao Chang*, Yu-Chen Chang, Wei-Tung Liu, Sheng-Zhu Ho, Chen-Hsuan Lu, Tilo H. Yang et al. "Magnetic Field-Induced Polar Order in Monolayer Molybdenum Disulfide Transistors." Advanced Materials 36, no. 52 (2024): 2411393.
DOI: 10.1002/adma.202411393
D.H. carried out temperature and magnetic field dependent electrical transport measurements, where hysteretic behavior was first discovered at cryogenic temperature under finite magnetic fields. D. H., W.-H. C., Y.-W. L., and N.-C. Y. wrote the first drafts of the paper with assistance from all other authors, and D. H. and N. -C. Y. completed the final version of the paper.
*These authors contributed equally to this work.

Lu, Chen-Hsuan, Duxing Hao, and Nai-Chang Yeh. "A perspective of recent advances in PECVD-grown graphene thin films for scientific research and technological applications." Materials Chemistry and Physics (2024): 129318.
DOI: 10.1016/j.matchemphys.2024.129318
D.H. designed the experiment, synthesized some of the graphene and fabricated some of the devices, performed some of the experimental characterizations and measurements, and assisted in writing the Chapter 5 of the manuscript.

TABLE OF CONTENTS

LIST OF ILLUSTRATIONS

LIST OF TABLES

NOMENCLATURE

1H-MoS_2. Molybdenum disulfide monolayer in 1H phase.

2D. Two-dimensional.

AFM. Atomic force microscopy or atomic force microscope.

AHE. Anomalous Hall effect.

AQHE. Anomalous quantum Hall effect.

CVD. Charge neutrality point.

CVD. Chemical vapor deposition.

DI. Deionized.

DOS. Density of states.

EBL. Electron-beam lithography. Also abbreviated as e-beam lithography.

EDS. Also abbreviated as **EDX**. Energy-Dispersive X-ray Spectroscopy.

FET. Field-effect transistor.

HOPG. Highly ordered pyrolytic graphene.

IPA. Isopropyl alcohol.

LCP. Left circularly polarized light.

LL. Landau levels.

MD. Molecular dynamics. Refers to the molecular dynamics simulation.

MIBK. Methyl Isobutyl Ketone.

ML. Monolayer.

OAM. Orbital angular momentum.

PEC. Proximity effect correction.

PECVD. Plasma-enhanced chemical vapor deposition.

PLL. Pseudo Landau levels.

PMF. Pseudo magnetic field.

PMMA. Poly(methyl methacrylate).

QHE. Quantum Hall effect.

RCP. Right circularly polarized light.

RIE. Reactive ion etching.

SAM. Spin angular momentum. Also known as the circular polarization in the context of light.

SCCM. Standard cubic centimeter per minute (sccm). Unit of gas flow rate.

SEM. Scanning electron microscopy or scanning electron microscope.

TMD(c). Transition metal dichalcogenide.

VHE. Valley Hall effect.

XPS. X-ray photoelectron spectroscopy.

Chapter 1

INTRODUCTION

1.1 Introduction

Modern electronic and optoelectronic devices demand increasingly smaller dimensions alongside ever-improving performance. Therefore, it is of vital importance to identify new materials that not only support smaller device sizes but also introduce novel physical mechanisms capable of enhancing functionalities. Two-dimensional (2D) quantum materials,[1–4] naturally thinner than bulk materials, provide not only a physical advantage in size but also distinguish electronic bandstructures where novel quantum phenomena emerge, such as ferroelectricity[5], superconductivity,[6] and selective optical excitation.[7] Understanding the physical origin of those mechanisms thereby devising a mean of controlling various degrees of freedom to achieve the desirable functionalities are thus important for advancing the application of 2D quantum materials in the next-generation technologies.

Graphene, a monolayer (ML) of carbon atoms forming a honeycomb lattice structure and arguably the most well-known member of the 2D materials, exhibits a wide range of novel properties such as 2D massless electron with high mobility near its Dirac point,[8] integer and fractional quantum Hall effects[9–11].The honeycomb lattice consists of two inequivalent sublattices in the real space and thus two inequivalent K and K' valleys in the momentum space. On the other hand, the preservation of inversion symmetry in honeycomb lattice implies a degenerate valley degree of freedom.[12] In contrast, although ML transition metal dichalcogenides (TMDs) share a similar hexagonal Bravais lattice with graphene, their constituent atoms lack inversion symmetry, thus leading to the intrinsic valley symmetry breaking. Generally speaking there are three important characteristics of the TMD family

that differ from graphene: 1) different choices of elements would result in different electronic bandstructure. 2) the three-atomic-layer structure allows for accommodation of out-of-plane orders and phases in a ML of material. 3) a sizeable energy gap (~2eV) usually appears in these materials, thus allowing for electronic and optoelectronic applications in the semiconductor industry.

The tuning knobs for controlling the properties of these 2D materials may be categorized by their origin, *i.e.* structural or nonstructural. Crudely speaking, the structural tuning knobs may include, but are not limited to, structural phase engineering, strain-engineering, layer stacking or twisting, doping, and defect engineering, *etc*. These structural modifications shape the fundamental electronic bandstructure of the material, and therefore the resulting effect generally tends to be drastic. The nonstructural tuning knobs, such as temperature, external magnetic field, electrical doping, and laser excitation, usually provide a finer control while being viable, likely reversable, and externally tunable once device were made.

This thesis mainly focuses on three specific scenarios. Firstly, in ML-graphene transistors, we utilize nanoscale architected structures on the substrate to induce inversion symmetry breaking, nonlocal currents, enhanced electronic correlation, and valley Hall effect. Secondly, in monolayer MoS_2 transistors, we discover the emergence of out-of-plane polar order due to asymmetric lattice expansion over silicon oxide substrate under magnetic field at cryogenic temperatures. Thirdly, we design and fabricate a structured light-enabled cryogenic scanning photocurrent spectroscopy (PCS) instrument and demonstrate its versatility for investigating 2D quantum materials by applying photons with spin and orbital angular momentum (SAM/OAM) to ML-MoS_2 transistors, which reveal enhanced OAM light-matter interaction and magnetic field-enhanced Landé *g*-factor under SAM light.

This thesis is organized as follows: Chapter 1 briefly summarizes the basic properties of graphene, ML 2H-MoS_2, and the theoretical background for structured light; Chapter 2 discusses the synthesis of 2D materials, fabrication processes for developing electronic and

optoelectronic devices, and measurement methodologies employed in this thesis; Chapter 3 describes the strain-induced valley and potential spin symmetry breaking, and the resulting phenomena observed in ML-graphene field effect transistors (FETs); Chapter 4 covers the discovery of magnetic field-induced polar order, which emerges at cryogenic temperature in ML-MoS_2 FET; Chapter 5 describes the development of a novel instrumentation for cryogenic scanning photocurrent spectroscopy, which is capable of researching structured light-matter interactions and is applied to the studies of ML-MoS_2 FETs; Chapter 6 summarizes the key findings of this thesis and discusses the outlook of the research.

1.2 Electronic properties of graphene

The electronic properties of graphene have been extensively discussed in numerous theoretical and review articles.[13–16] Therefore, this section only provides a concise summary of the most relevant, tailored to serve the objectives of this thesis.

Tight-binding model of graphene and its low-energy character near the Dirac point

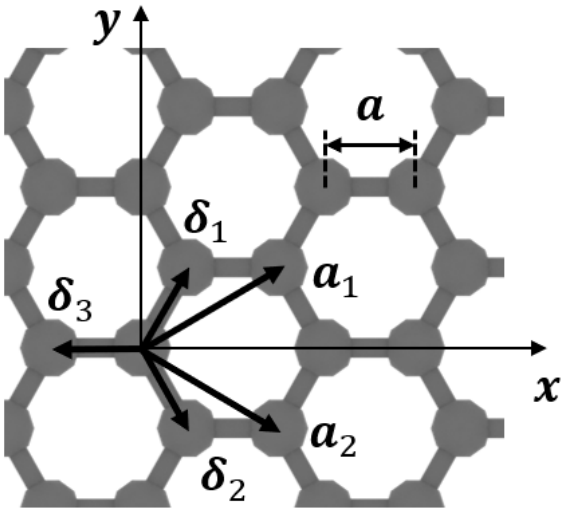

Figure 1.1 Honeycomb lattice of graphene.

The honeycomb lattice structure of graphene may be described by a hexagonal (triangular) Bravais lattice with a two-atom basis. The Bravais lattice vector in the real space may be denoted as follows:

$$\boldsymbol{a}_1 = \frac{a}{2}\left(3, \sqrt{3}\right), \boldsymbol{a}_2 = \frac{a}{2}\left(3, -\sqrt{3}\right), \tag{1.1}$$

where $a \approx 0.142nm$ is the distance between two carbon atoms. The nearest neighbor may be denoted by the following three vectors:

$$\boldsymbol{\delta}_1 = \frac{a}{2}\left(1, \sqrt{3}\right), \delta_2 = \frac{a}{2}\left(1, -\sqrt{3}\right), \boldsymbol{\delta}_3 = -a(1,0), \tag{1.2}$$

The tight-binding approximations assume that there is possible electron hopping between nearest neighbors and next-nearest neighbors (equation 1.3),[13] whose amplitude is proportional to the nearest neighborhood hopping energy $t \approx 2.8\ eV$ and the next-nearest neighborhood hopping energy $t' \approx 0.07\ eV$.[13] The off-diagonal Hamiltonian is described as the following:

$$\begin{aligned} H_{hopping} = -t \sum_{\langle i,j\rangle_{nn},\sigma} & \left(a^{\dagger}_{\sigma,i} b_{\sigma,j} + b^{\dagger}_{\sigma,j} a_{\sigma,j}\right) \\ -t' \sum_{\langle i,j\rangle_{nnn},\sigma} & \left(a^{\dagger}_{\sigma,i} a_{\sigma,j} + b^{\dagger}_{\sigma,i} b_{\sigma,j} + a^{\dagger}_{\sigma,j} a_{\sigma,i} + b^{\dagger}_{\sigma,j} b_{\sigma,i}\right), \end{aligned} \tag{1.3}$$

where simplification with $\hbar = 1$ was used. Neglecting the next nearest neighbor hopping terms and writing equation (1.3), considering the degeneracy of the two spins and substituting the nearest neighbors' vectors (equation (1.2)), we obtain:

$$H_{hopping} = -t \sum_{nn=1,2,3} e^{-i\boldsymbol{k}\cdot\boldsymbol{\delta}_{nn}} = -t\left(e^{-ik_x a} + 2e^{-\frac{ik_x a}{2}} \cos\frac{k_y a\sqrt{3}}{2}\right) \equiv -t\Delta_{\boldsymbol{k}}. \quad (1.4)$$

The diagonal term of the Hamiltonian gives the orbital energy of the 2p level plus higher order overlapping integral between electronic wavefunctions in the nearby Bravais lattice. Therefore the explicit form of Hamiltonian is given by[16]

$$H = \begin{pmatrix} \epsilon_{2p} & -t\Delta_{\boldsymbol{k}} \\ -t\Delta_{\boldsymbol{k}}^{\dagger} & \epsilon_{2p} \end{pmatrix}. \quad (1.5)$$

Solving the Hamiltonian and assuming that the overlap integral is zero between the two nearest atoms in a different sublattice, we obtain equation (1.6):

$$E_{\boldsymbol{k}} = \epsilon_{2p} \pm t\sqrt{|\Delta_{\boldsymbol{k}}|^2} = \epsilon_{2p} \pm t\sqrt{3 + 4\cos\left(\frac{3ak_x}{2}\right)\cos\left(\frac{\sqrt{3}ak_y}{2}\right) + 2\cos\left(\sqrt{3}ak_y\right)}, \quad (1.6)$$

Following a similar procedure and bringing back the next nearest neighbor hopping gives equation (1.7):[13]

$$E_{\boldsymbol{k}} = \epsilon_{2p} \pm t\sqrt{3 + 4\cos\left(\frac{3ak_x}{2}\right)\cos\left(\frac{\sqrt{3}ak_y}{2}\right) + 2\cos\left(\sqrt{3}ak_y\right)} - 4t'\cos\left(\frac{3ak_x}{2}\right)\cos\left(\frac{\sqrt{3}ak_y}{2}\right) + 2\cos\left(\sqrt{3}ak_y\right). \quad (1.7)$$

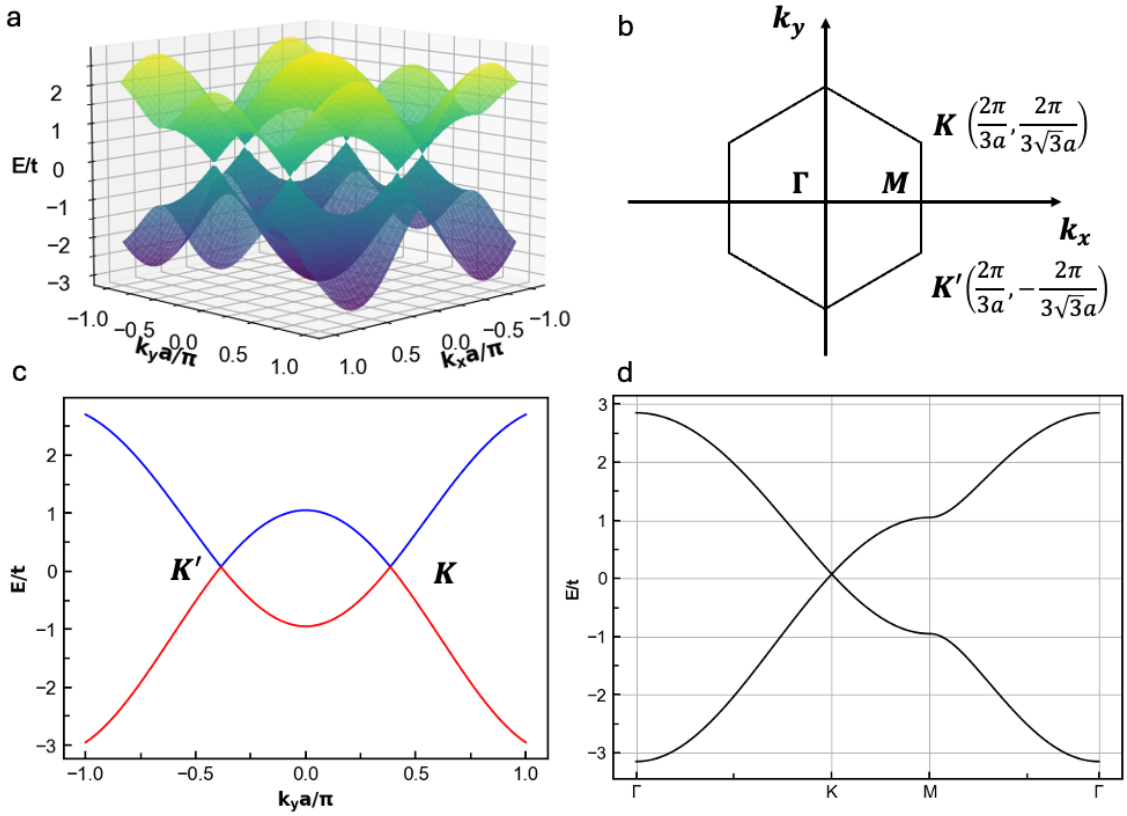

Figure 1.2 Tight-binding bandstructure of graphene. (a) Electronic bandstructure of the tight binding model. $\epsilon_{2p} = 0$, $t = 2.8$ eV, $t' = 0.07$ eV, and $\hbar = 1$ was used in the calculation. (b) Brillouin zone of the reciprocal lattice. (c) Linecut of the bandstructure along $k_x = \frac{2\pi}{3a}$, showing linear energy dispersive relationship near the vicinity of $\boldsymbol{K'}$ and $\boldsymbol{K}$ points. The blue (red) line corresponds to the plus (minus) sign of the energy dispersive relationship in equation (1.7) in the main text. (d) Electronic bandstructure along high-symmetry lines.

Setting $\epsilon_{2p} = 0$, $t = 2.8$ eV, $t' = 0.07$ eV, and $\hbar = 1$ gives results shown in Figure 1.2(a). The Dirac cone structure at the boundary of the Brillouin zone corresponds to two "valleys" at $\boldsymbol{K}$ and $\boldsymbol{K'}$ point (Figure 1.2(b)) given in terms of the reciprocal lattice vector in equation (1.8):

$$\boldsymbol{K} = \left(\frac{2\pi}{3a}, \frac{2\pi}{3\sqrt{3}a}\right), \boldsymbol{K'} = \left(\frac{2\pi}{3a}, -\frac{2\pi}{3\sqrt{3}a}\right). \tag{1.8}$$

Expanding the Hamiltonian near the Dirac point $\boldsymbol{k} = \boldsymbol{K} + \boldsymbol{q}$ where $|\boldsymbol{q}/\boldsymbol{K}| \ll 1$ gives Hamiltonian and energy dispersive relationship near the Dirac point:

$$H_{\boldsymbol{K}}(\boldsymbol{q}) = \frac{3ta}{2}\boldsymbol{\sigma_P} \cdot \boldsymbol{q}, \qquad E_{\boldsymbol{K}}(\boldsymbol{q}) = \pm\frac{3ta}{2}|\boldsymbol{q}| + o\left(\left|\frac{\boldsymbol{q}}{\boldsymbol{K}}\right|^2\right), \tag{1.9}$$

where $v_F \equiv \frac{3ta}{2}$ is the Fermi velocity and $\boldsymbol{\sigma_P}$ is the Pauli spin matrices. Here we denote the Pauli spin matrices as $\boldsymbol{\sigma_P}$ to distinguish it from the symbol of conductivity tensor $\boldsymbol{\sigma}$ later in the text. Similar can be done near the ***K'*** as shown in Figure 1.2(c). The energy dispersive relationship near the Dirac point is linear and particle hole symmetry is preserved if the next nearest neighbor hopping is not considered. The electronic bandstructure along high symmetry lines is shown in Figure 1.2(d).

Fundamentals of electrical transport properties of pristine graphene transistors

The magnetic field-induced effects may be measured in electrical transport measurement in the graphene field-effect transistor. In a typical Hall configuration (See Section 2.7 and Figure 2.12), the longitudinal resistivity ρ_{xx} and Hall resistivity ρ_{xy} are derived by dividing a small excitation current *I* in longitudinal direction by voltage measured across longitudinal pair of contacts (V_{xx}) and transverse pair of contacts (V_{xy}), respectively:

$$\rho_{xx} = \frac{V_{xx}}{I}, \qquad \rho_{xy} = \frac{V_{xy}}{I}, \qquad \boldsymbol{\rho} = \begin{pmatrix}\rho_{xx} & \rho_{xy}\\ \rho_{yx} & \rho_{yy}\end{pmatrix}. \tag{1.10}$$

The conductivity tensor $\boldsymbol{\sigma}$ is the inverse of the resistivity tensor $\boldsymbol{\rho}$. In pristine graphene FET, with $\rho_{xx} = \rho_{yy}$ and $\rho_{xy} = -\rho_{yx}$, we have

$$\sigma_{xx} = \frac{\rho_{xx}}{\rho_{xx}^2 + \rho_{xy}^2}, \quad \sigma_{xy} = \frac{-\rho_{xy}}{\rho_{xx}^2 + \rho_{xy}^2}. \tag{1.11}$$

In pristine graphene FET, the inversion symmetry guarantees $\rho_{xy} = -\rho_{yx}$; however, in the strained graphene FET device, where the graphene is under substantial anisotropic strain applied by nanostructures, ρ_{xy} can thus be substantially different from ρ_{yx}.

The Fermi level is tuned by using a back gate (or also commonly used, a top gate) voltage assuming a parallel capacitor model, as shown in Figure 1.4. The carrier density (n_c) in the parallel capacitor model is thus

$$n_c = C_g(V_g - V_{CNP}) = \frac{\varepsilon_0 \varepsilon_r (V_g - V_{CNP})}{de}, \tag{1.12}$$

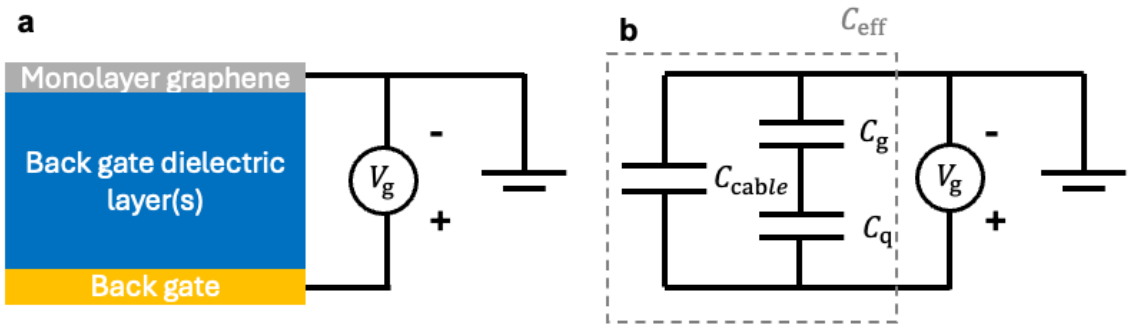

Figure 1.3 Parallel capacitor model of graphene FET. (a) Simplified parallel capacitor model for back gate capacitance. (b) Electric circuit diagram from effective capacitance (C_{eff}) that consists of back gate capacitance, quantum capacitance of graphene, and cable capacitance.

where C_g is capacitance per unit area of the back gate contributed by the dielectric layer, V_g is applied DC gate voltage, ε_0 is the vacuum permittivity, ε_r is the relative permittivity of the dielectric (ε_r= 3.7~3.9 for SiO_2 and ε_r= 3.26 ~ 3.76 for different thickness of h-BN.[17]), V_{CNP} is the gate voltage of the charge neutrality point, d is the thickness of the dielectric layer, and

e is the elementary charge. In practice, the total effective capacitance per unit area (C_{eff}) is used instead of C_{g} to provide full description of the back-gate doping effect, which typically consists of quantum capacitance of graphene (C_{q}) in series with the gate capacitance (C_{g}) and the cable capacitance (C_{cable}) in parallel to the above combined, as shown in Figure 1.3(b).[18,19]

Under the simple Drude model, we have the field-effect mobility (μ_{FE})

$$\mu_{\mathrm{FE}} = \frac{\sigma_{xx}(V_{\mathrm{g}})}{en(V_{\mathrm{g}})}, \tag{1.13}$$

where $\sigma_{xx}(V_{\mathrm{g}})$ is the longitudinal conductivity measured at gate voltage V_{g} and $n(V_{\mathrm{g}})$ is computed using equation (1.12). Note that even though combining equation (1.12) and (1.13) gives a reasonable estimate of field effect mobility at a reasonably large carrier concentration, they failed to explain the experimental data near the Dirac point because equation (1.12) did not capture spatially distributed electron and hole puddles[20] in the real device, where the carrier concentration never reaches zero. In this context J. Gosling et al. employs a more careful methodology to characterize the mobility for the low carrier concentration scenario.[20]

Additionally, we note that the Fermi level relative to the charge neutrality point with carrier density n may be derived as

$$E_F(n) = \hbar v_F \sqrt{\pi n}. \tag{1.14}$$

External magnetic field and integer quantum Hall effect

Under an external magnetic field, the Hamiltonian near the Dirac cone can be written in terms of momentum of electrons substitution $\boldsymbol{p} \rightarrow \boldsymbol{p} + \boldsymbol{eA}$, where $\boldsymbol{A}$ is the vector potential of the externally applied magnetic field (B_{ext}).

$$H_K(\boldsymbol{q}) = v_F \boldsymbol{\sigma} \cdot \boldsymbol{q} \rightarrow v_F \boldsymbol{\sigma} \cdot (\boldsymbol{p} + \boldsymbol{eA}), \tag{1.14}$$

Assuming a Landau gauge and solving the Hamiltonian results in energy eigenvalues as follows:[21]

$$E_n = \mathrm{sgn}(n)\sqrt{2e\hbar v_F^2 |n| B_{\mathrm{ext}}}, \tag{1.15}$$

where n is the carrier density and e is the elementary electron charge. We found that the conduction band split into discrete Landau levels whose energy is proportional to square root of the carrier density $\sqrt{|n|}$.

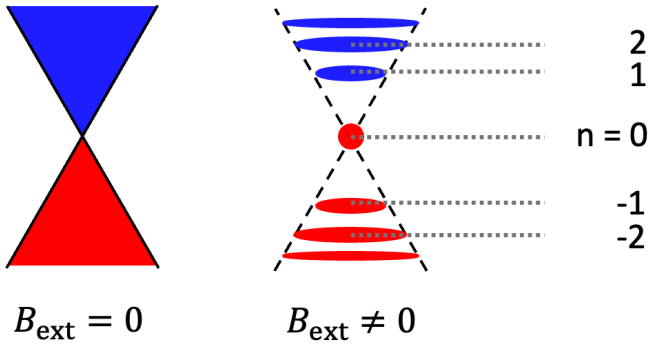

Figure 1.4 Illustration of Landau levels for electron (blue) and hole (red) under external magnetic field near the Dirac point.

Under an out-of-plane external magnetic field, the discrete nature of Landau levels manifests the magnetic field-induced quantum fluctuation of the conductivity of the device, known as the Shubnikov–de Haas (SdH) oscillations. Here, the Fermi level is fixed while Landau levels moves in the energy scale (as shown in Figure 1.5(a)) as magnetic field increases.[10] Alternatively, we can keep the Landau levels fixed with a constant magnetic field while changing the Fermi level, and quantum oscillation should still be seen in Figure 1.5(b).[10]

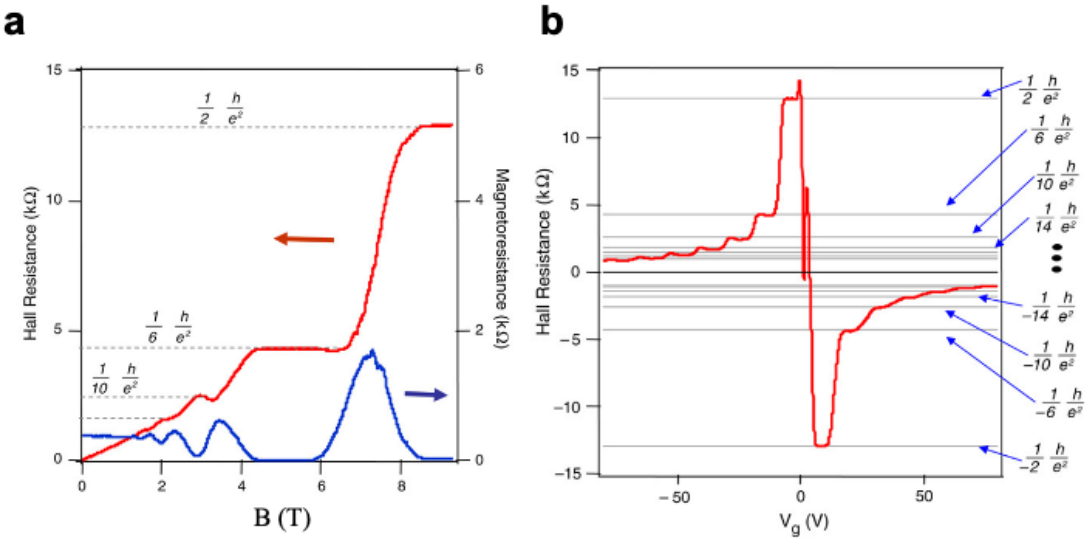

Figure 1.5 Integer quantum Hall effect in graphene transistors. (a) Quantized magnetoresistance and Hall resistance of a graphene device where $n \approx 10^{12}$ cm^{-2} and $T = 1.6$ K. The horizontal lines correspond to the inverse of the multiples e^2/h. The QHE in the electron gas is demonstrated by at least two quantized plateaus in R_{xy} with vanishing R_{xx} in the corresponding magnetic field regime. (b) The Hall resistance as a function of gate voltage at fixed magnetic field $B = 9$ T, measured at 1.6 K. The horizontal lines correspond to the inverse of integer multiples of e^2/h values. Both figures reprinted from Solid State Communications 143, 14, Z. Jiang, Y. Zhang, Y.-W. Tan, H. L. Stormer, and P. Kim, Quantum Hall effect in graphene, (2007) with permission from Elsevier.

In the low-field regime where the Hall resistance is linearly proportional to the external magnetic field, the Hall mobility μ_{Hall} may be extracted as

$$\mu_H = en_B\sigma_{xx}, \qquad n_B = \frac{1}{e}\frac{dR_{xy}}{d\,B}, \tag{1.16}$$

where the n_B is the carrier density extracted from the Hall measurements, R_{xy} is the measured Hall resistance.

1.3 Electronic bandstructure and optoelectronic interaction of monolayer MoS_2

Group VI transition metal dichalcogenides (TMDs, with chemical composition MX_2), whose unit cell consists of one transition metal (M = Mo, W, etc) and two chalcogen atoms (X = S, Se, Te) include a broad family of layered materials. The diversity of the structural phases of the bulk MX_2 materials arises from variations in both interlayer stacking order and intralayer atomic arrangements.[22,23]

Crystalline structure and electronic bandstructure of 1H-MoS_2

In the case of monolayer molybdenum disulfide (ML-MoS_2), 1H (as known as ML 2H phase), 1T, 1T′, 1T″ (also known as d1T), and 1T‴ phase were identified as shown in Figure 1.6.[24–26] It is worth noting that 1H phase is the stable phase, while all other phases need to be obtained via chemical-assisted approaches[27] or using post-growth chemical treatments.[26,27] Those various crystalline structure host rich physics, such as superconductivity in 1T phase,[28] and ferroelectricity and 1T' phases.[26]

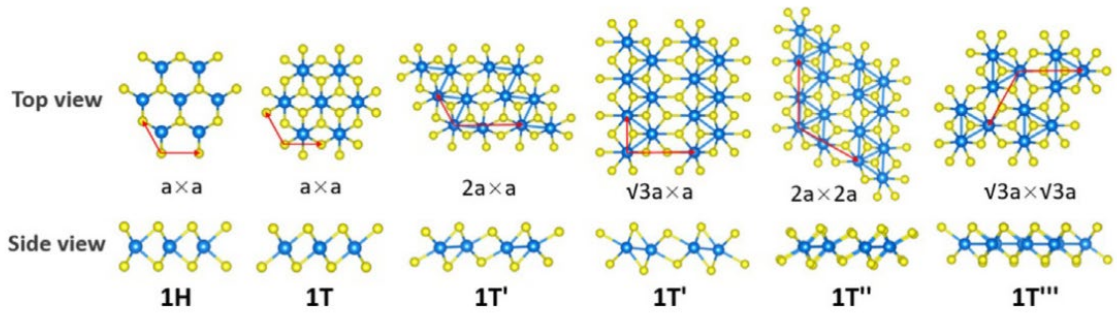

Figure 1.6 Top view and side view of the atomic structures of MoS_2 monolayers with different polymorphs, including 1H, 1T, 1T′, 1T″, and 1T‴ phases. The unit cells are marked by red arrows. Mo-Mo dimerization can be seen in 1T' phase and Mo-Mo trimerization can be seen in 1T″ and 1T‴ phases. Reprinted from ref.[29] with permission from John Wiley and Sons.

This thesis mainly focuses on the stable 1H-phase due to its semiconducting nature and its direct bandgap whose size is within photons of visible wavelength, which are crucial for both field-effect transistor application and optoelectronic interaction studies. The 1H-MoS_2 features a three-layer structure where the hexagonal plane of molybdenum atoms sandwiched by two hexagonal planes of sulfur atoms (Figure 1.7(a)), forming a trigonal prismatic coordination between one molybdenum atom and six surrounding sulfur atoms as shown in Figure 1.7(b).

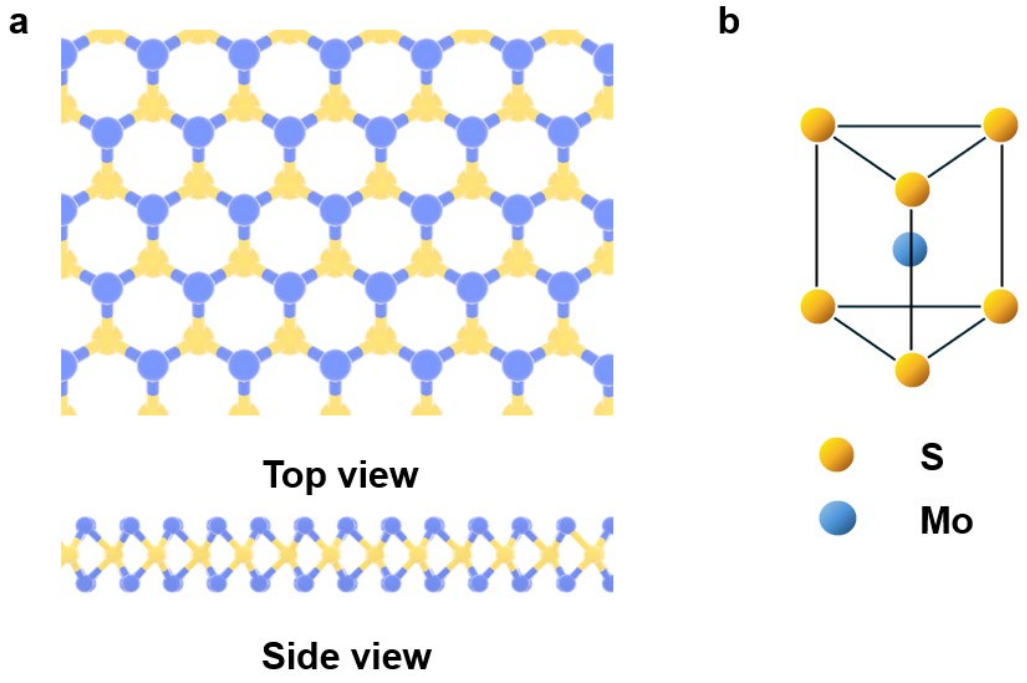

Figure 1.7 Atomic structures of 1H-MoS_2. (a) Top view and side view of the hexagonal crystal structure. (b) Trigonal prismatic coordination between one molybdenum atom and six surrounding sulfur atoms.

Its electronic structure can be computed directly using first-principle approach,[30–32] or be described by tight-binding model with three,[33] five,[34] and eleven-bands[35] whose parameters

fit from the first-principle results. Here we follow the five-band tight-binding model to construct the ground states, where five Mo d-bands were d_{z^2}, d_{xy}, $d_{x^2-y^2}$, d_{xy}, and d_{yz}.[34] The Hamiltonian is given by[36,37]

$$\mathcal{H}_{\vec{k}} = \lambda \vec{L} \cdot \vec{S} + I_2 \otimes \mathcal{H}_0(\vec{k}), \tag{1.17}$$

where the first spin-orbit coupling term comprises orbital angular momentum $\vec{L}$ and spin angular momentum $\vec{S}$ with a couple constant λ=0.073eV. The second term is the direct product of 2×2 identity matrix I_2 in spin-space and 5×5 Hamiltonian in orbital space with the above five orbitals. There exact form of the $\mathcal{H}_0(\vec{k})$ is given by equation (A2-A5) in reference[36] and equation (13-24) in reference[37]. Its solution gives energy bands as illustrated in Figure 1.8.

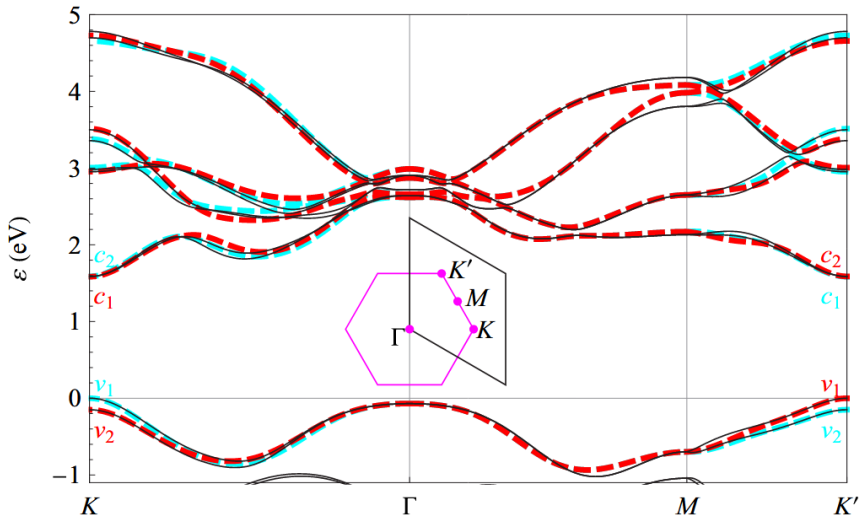

Figure. 1.8 Quasiparticle band structure of monolayer MoS_2. The solid curves were obtained using the QUANTUM ESPRESSO package[38] with fully relativistic pseudopotentials under the Perdew-Burke-Ernzerhof generalized-gradient approximation, and a $16 \times 16 \times 1$ k grid.

The dashed curves were calculated from the tight-binding model, with cyan (red) representing states that are even (odd) under mirror operation with respect to the Mo plane. $v_{1,2}$ and $c_{1,2}$ label the bands close to the valence- and conduction-band edges near the K and K′ points. The inset shows the hexagonal Brillouin zone (pink) associated with the triangular Bravais lattice of MoS_2 and an alternate rhombohedral primitive zone (black), and labels the principle high-symmetry points in reciprocal space. Note that the valence-band maxima at is only slightly lower in energy than the valence-band maxima at K, K. Reprinted figure with permission from F. Wu, F. Qu, and A. H. MacDonald, Phys. Rev. B 91, 075310, (2015). Copyright 2015 by the American Physical Society.

There are three most notable properties of the electronic bandstructure. 1) The 1H-MoS_2 is a semiconducting material with a direct bandgap of ~1.9eV, and therefore its field-effect transistor shows a standard on-off characteristics controlled by a back gate voltage (for example, see Figure 5.8(b)). The direct bandgap of the 1H-MoS_2 allows for direct excitonic transitions at K/K′ point, as compared to its multilayer and bulk form with an indirect bandgap (Figure 1.9). 2) The inherent inversion symmetry breaking leads to valley-distinct transport and valley-selective optical excitation. 3) The strong spin-orbital coupling created a sizable splitting near the conduction band maximum, allowing for further spin-controlled excitations via spin-valley locking.[39] The spin-orbital coupling near the conduction band minimum is orders of magnitude smaller, and therefore usually omitted.

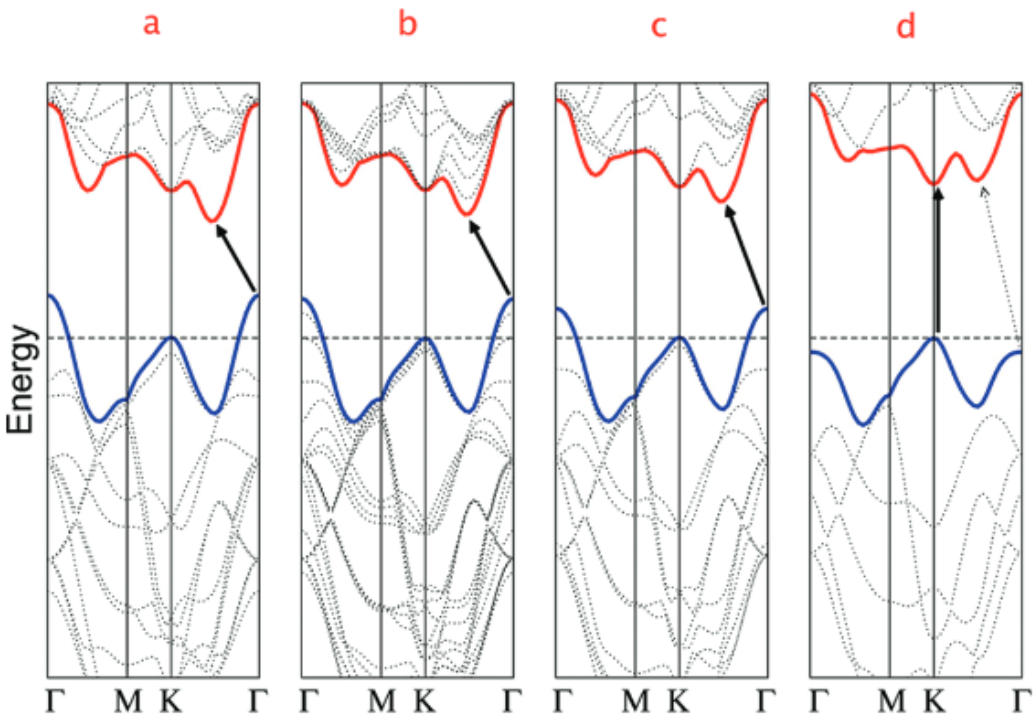

Figure. 1.9 Calculated band structures of (a) bulk MoS_2, (b) quadrilayer MoS_2, (c) bilayer MoS_2, and (d) ML-MoS_2. The solid arrows indicate the lowest energy transitions. Bulk MoS_2 is characterized by an indirect bandgap. The direct excitonic transitions occur at high energies at K point. With reduced layer thickness, the indirect bandgap becomes larger, while the direct excitonic transition barely changes. For ML-MoS_2 in (d), it becomes a direct bandgap semiconductor. Reprinted with permission from Nano Lett. 10, 1271, (2010). A. Splendiani, L. Sun, Y. Zhang, T. Li, J. Kim, C.-Y. Chim, G. Galli, and F. Wang, Emerging Photoluminescence in Monolayer MoS_2. Copyright 2010 American Chemical Society.

Excitonic bandstructure and optical transition of 1H-MoS_2

Fengcheng et al. formulated the exciton quasiparticle Hamiltonian of ML-MoS_2 by a two part Hamiltonian with H_0 as described the five-band Hamiltonian in equation (1.17) and an additional term H_I as the Keldysh interaction potential[40,41] for dielectric screening:[36]

$$H = H_0 + H_{\mathrm{I}},$$
$$H_{\mathrm{I}} = \frac{1}{2}\sum_{\vec{R},\vec{R'}} V_{|\vec{R}-\vec{R'}|} a^{\dagger}_{\vec{R}v} a^{\dagger}_{\vec{R}'v'} a_{\vec{R}'v'} a_{\vec{R}v}, \tag{1.18}$$

where $a^{\dagger}_{\vec{R}v}$ ($a_{\vec{R}'v'}$) is the creation (annihilation) operator for orbital v at Mo site $\vec{R}$. The orbital v denotes a pair of orbital label and spin label for the electron collectively. Solving the Hamiltonian and shifting the bandstructure rigidly according to experimental values, the result is shown in Figure 1.10.[36]

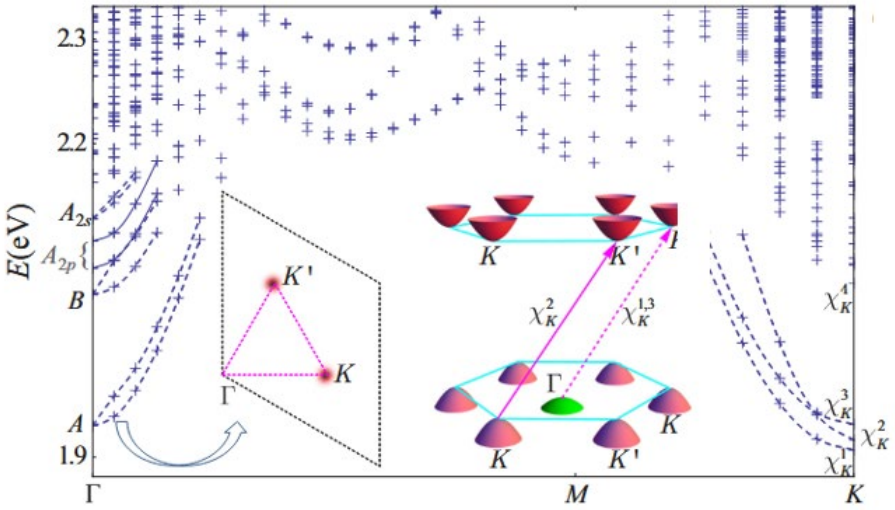

Figure 1.10 Energies of bright excitons as a function of center-of-mass momentum $\vec{Q}$. This figure is based on a calculation performed using a 45 × 45 k grid. The lines were added as a guide to the eye. Solid (dashed) lines represent states that are doubly (singly) degenerate. The labels of the excitons with $\vec{Q}$ = 0 are explained in the main text. Excitons with $\vec{Q}$ = $\boldsymbol{K}$ are labeled by χ_K^1, χ_K^2 , and so on in ascending order of energy. The left inset is a k-space map plot of $P_{\vec{Q}}(k)$ [see Eq. (4) in ref[36]] for the $\vec{Q}$ = 2/45 M exciton in the lower energy branch evolving from A. The right inset schematically illustrates the dominant electron-hole transitions which contribute to the χ_K^1, χ_K^2, and χ_K^3 exciton states. Reprinted figure with

permission from F. Wu, F. Qu, and A. H. MacDonald, Phys. Rev. B 91, 075310, Copyright (2015) by the American Physical Society.

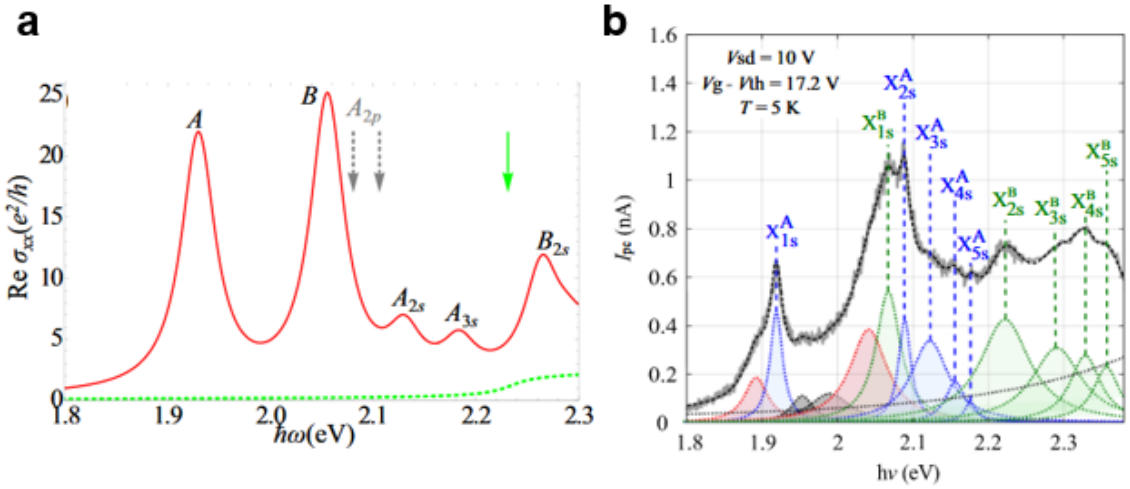

Figure 1.11 (a) Real part of the optical conductivity with (solid red curve) and without (dashed green curve) electron-hole interactions. Note that we have rigidly shifted the excitation energy spectrum by a constant, so that the A exciton energy is at 1.93 eV as measured by photoluminescence experiments.[42–45] Reprinted figure with permission from F. Wu, F. Qu, and A. H. MacDonald, Phys. Rev. B 91, 075310, (2015). Copyright 2015 by the American Physical Society. (b) Photocurrent spectrum for the monolayer MoS_2 device (grey, solid line) and fit to a multiple-peak Lorentzian function (black, dashed line). The individual Lorentzian functions corresponding to Rydberg series of excitons X^A and X^B are shown in blue and green, respectively. Reprinted from ref. [46] under CC-BY license.

The exciton bandstructure at point Γ (Figure 1.10) corresponds to the direct transition at K/K' valley and the excitonic labels A, and B corresponds to the transition from the v_1 to c_2 and

v_2 to c_1 band, respectively, as labeled in Figure 1.8. The subscript of A and B, namely A_{2s}, A_{2p}, A_{3s}, is analogous to 2D hydrogen model of the excitonic quasiparticle, where similarly we find A_{2s}, A_{3s}, etc. are the of Rydberg series carrying excitonic orbital angular momentum of 1, 2, etc. Figure 1.11(a) shows the real part of the computed optical conductivity in longitudinal direction,[34] which may be revealed by photocurrent spectroscopy measurements[47] or photon absorption spectrum measurements.[45] In Fig 1.11(b), Rydberg series of A and B exciton were observed in photocurrent spectroscopy measurements, showing similar structure as predicted by the tight-binding model. [47]

The bright A and B excitons were three-fold degenerated as protected by C_3 and time-reversal symmetry and therefore possess optical transition rules associated with the circular polarization of the excitation photon. This phenomenon is known as the circular dichroism and may be exploited to achieve valleytronics applications by combining spin-valley locking properties of 1H-MoS_2.[48] As shown in Figure 1.12, with right circularly polarized (RCP) light (colored in red), the A-exciton and B-exciton in K valley may be excited by matching photon energy. Similarly in K′ valley, A-exciton and B-exciton may be excited by left circularly polarized (LCP) light (colored in blue).

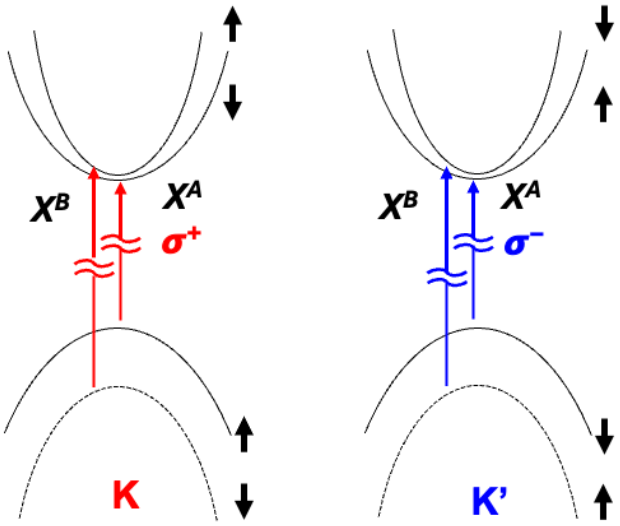

Figure 1.12 Schematics of Spin-valley locking in ML-MoS_2 and valley-selected excitation using circular polarization of photon.

Besides the bright A, B exciton series, there are other types of excitons as shown in Figure 1.13. In the direct transition from K and K′ valley, the spin-forbidden dark exciton X^D ($\uparrow\downarrow - \uparrow\downarrow$) may be excited with in-plane magnetic field[49] while the grey exciton X^G ($\uparrow\downarrow + \uparrow\downarrow$) may be excited by out-of-plane polarized light. [50] The intervalley exciton may be realized via short-range exchange action[51], Dixter-like interactions and strain-engineering approach[52]. As shown in Figure 13(b), the bright A, B exciton (which is an electron-hole pair) may couple to an additional excess electron in the conduction band and form lower-energy trion state T^A and T^B, respectively.[45]

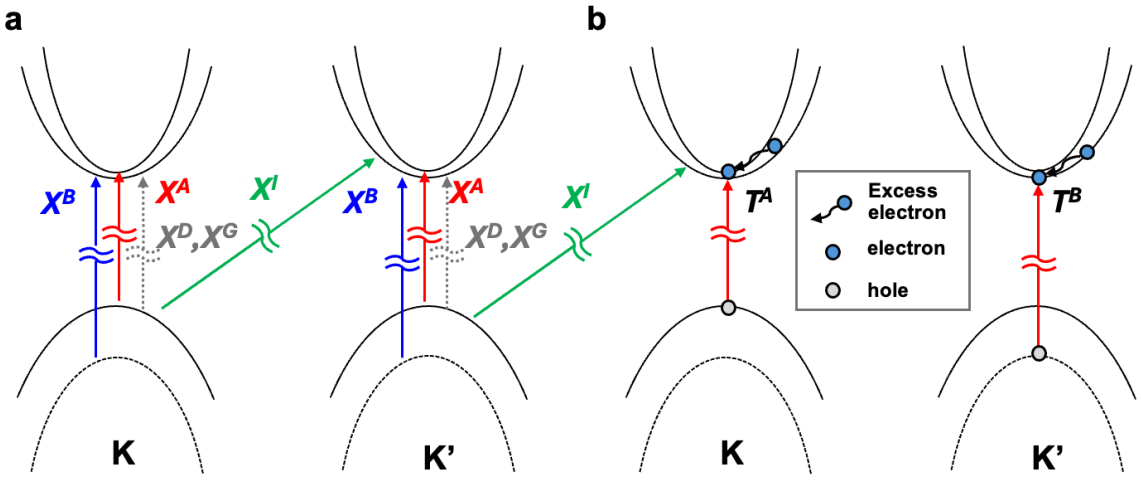

Figure 1.13 Schematics of excitons and trions in ML-MoS_2. (a) Intravalley bright A exciton (red), bright B-exciton (blue), dark and grey A exciton (grey), and intervalley exciton (green) in ML-MoS_2. (b) Schematics of A and B-trion in ML-MoS_2.

1.4 2D structured light: orbital angular momentum of light

Structured light refers to custom light field whose intensity, polarization, and phase are modulated.[53] It has been widely utilized in the field of modern fiber communication,[54] microscopic object manipulation,[55,56] and developing novel mechanisms of light-matter interaction.[57,58] 2D structured light further assumes the light propagates along the z-direction, with its properties structured in the x–y plane orthogonal to the direction of propagation. Among the various ways to structure light, two intrinsic degrees of freedom—spin angular momentum (SAM) and orbital angular momentum (OAM)—play central roles in defining the angular momentum properties of optical fields. Light with SAM, also known as the circularly polarized light, carries $+\hbar$ momentum per photon in the form of right circularly polarized (RCP) light and $-\hbar$ momentum per photon in the form of left circularly polarized

(LCP) light. In contrast, light with OAM (also known as the twisted light), may carry $\ell\hbar$ orbital momentum per photon, where $\ell \in \mathbb{Z}$ represent the topological charge. In this section, we will narrow down the scope to discuss the origin, generation of the orbital angular momentum of light, and its application in novel optoelectronic interaction.

The origin and properties of orbital angular momentum of light

To elucidate the origin of the orbital angular momentum, we first find the Maxwell equation that describes the light propagation

$$\nabla^2 \boldsymbol{E} - \mu_0 \epsilon_0 \frac{\partial^2 \boldsymbol{E}}{\partial t^2} = 0, \tag{1.19}$$

where μ_0 is the vacuum permeability and ϵ_0 is the vacuum permittivity. The monochromic assumption assumes

$$\boldsymbol{E}(\mathrm{r}, \mathrm{t}) = \boldsymbol{E}(\mathrm{r})\mathrm{e}^{-\mathrm{i}\omega \mathrm{t}}, \tag{1.20}$$

where ω is the angular frequency of the light. Combining equation (1.19) to (1.20) give rise to the Helmholtz equation:

$$\nabla^2 E + (\frac{\omega}{c})^2 E = 0, \tag{1.21}$$

where c is the speed of light in vacuum. The paraxial approximation assumes the beam travels in z direction, taking the form

$$E(r) = \psi e^{ikz}, \tag{1.22}$$

where k is the wave vector. Substituting equation (1.22) into equation (1.21) in Cartesian coordinates gives

$$\frac{\partial^2\psi}{\partial x^2}+\frac{\partial^2\psi}{\partial y^2}-2ik\frac{\partial\psi}{\partial z}=0, \tag{1.23}$$

or in cylindrical coordinates:

$$\left[\frac{1}{r}\frac{\partial}{\partial r}\left(r\frac{\partial}{\partial r}\right)+\frac{1}{r^2}\frac{\partial^2}{\partial\phi^2}-2ik\frac{\partial}{\partial z}\right]\psi(r,\phi,z)=0,. \tag{1.24}$$

The separation of variable takes the form

$$\psi(r,\phi,z)=u_{p,\ell}(r,z)\cdot e^{i\ell\phi}. \tag{1.25}$$

Substituting equation (1.25) into equation (1.24) gives a solution known as the Laguerre-Gaussian (LG) profile labeled by parameter p and ℓ:

$$\psi_{p\ell}(r,\phi,z)=\frac{C_{p,\ell}}{w(z)}\left(\frac{\sqrt{2}r}{w(z)}\right)^{|\ell|}L_p^{|\ell|}\left(\frac{2r^2}{w(z)^2}\right)\cdot e^{i\ell\phi}\cdot\exp\left(-\frac{r^2}{w(z)^2}\right)\cdot e^{i\Phi(z)}, \tag{1.26}$$

where $C_{p,\ell}=\left(\frac{2p!}{\pi(p+|\ell|)!}\right)^{1/2}$ is the normalization constant, $w(z)$ is the beam waist width as a function of z, $L_p^{|\ell|}\left(\frac{2r^2}{w(z)^2}\right)$ is the generalized Laguerre polynomial of degree p and order $|\ell|$, $\Phi(z)$ is the phase term that includes wavefront curvature and Gouy phase of the beam whose exact form can be found in reference[59,60].

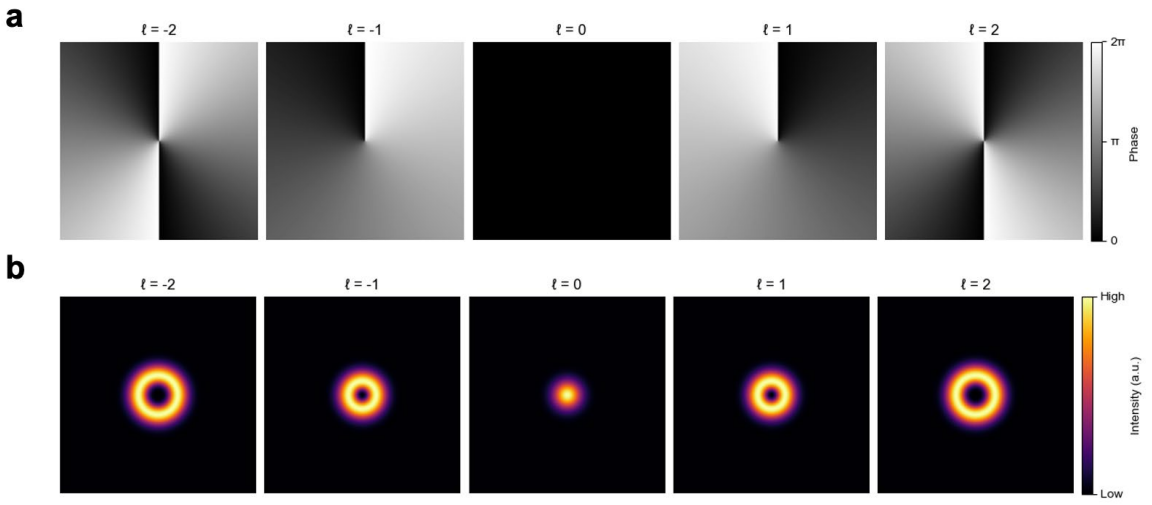

Figure 1.14 Illustration of (a) azimuthal phase and (b) spot intensity distribution for Laguerre-Gaussian mode with $p = 0$, $\ell = -2, -1, 0, 1, 2$. Here $w(z) \equiv 1$, $C_{p,\ell} \equiv 1$, and $\Phi(z) \equiv 0$ was used and the intensity was not normalized to same scale for visual clarity at higher ℓ values.

In equation (1.26), The C_ℓ symmetry was encoded in the azimuthal phase term $e^{i\ell\phi}$ as shown in the Figure 1.14(a). The intensity, characterized by $\left|\psi_{p\ell}(r, \phi, z)\right|^2$, shows a donut-like spot shape in the case of $p = 0$ due to phase singularity at the center of the spot (Figure 1.14(b)). The intensity profile of the LG modes is shown in Figure 1.15. Higher order LG modes can be generalized with a combination of (ℓ, p) value pairs, as shown in Figure 1.16.

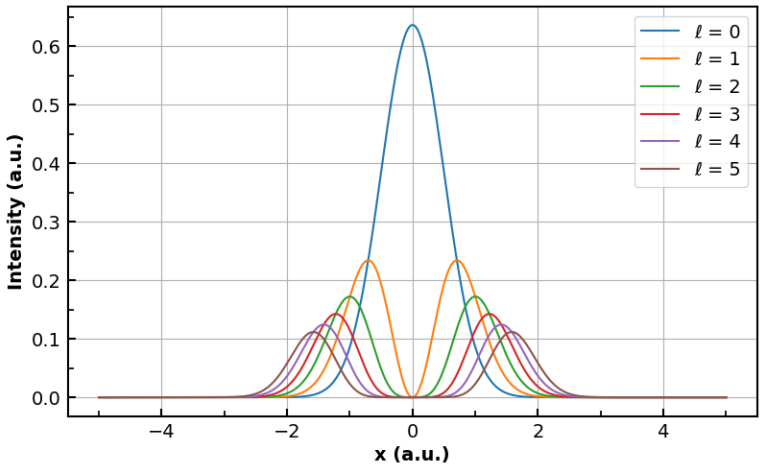

Figure 1.15 Intensity distribution along x-axis of the beam spot of the LG mode with $\ell = 0, 1, 2, 3, 4, 5$.

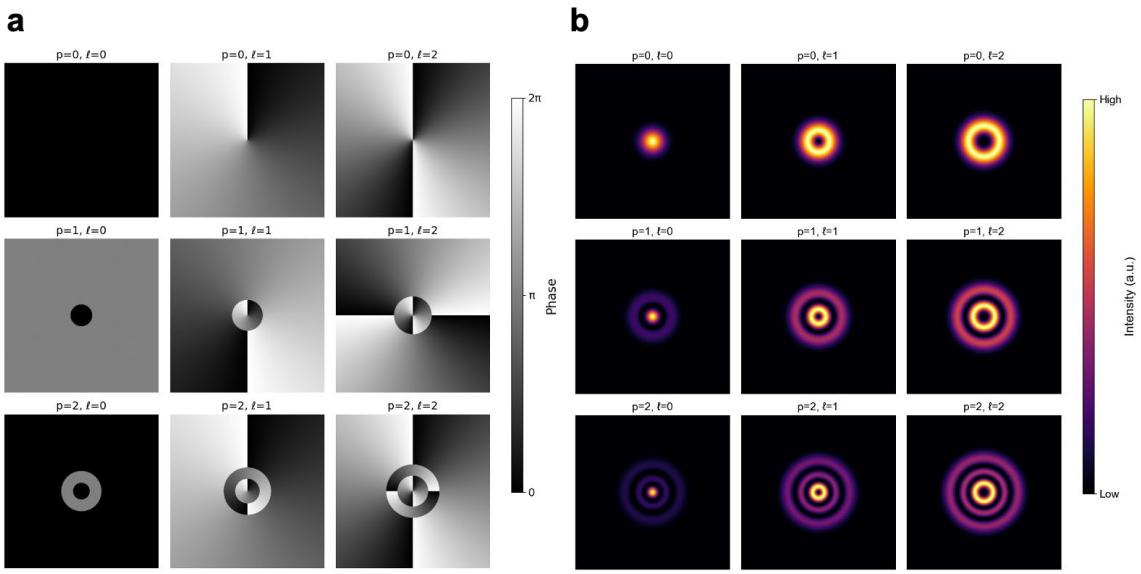

Figure 1.16 Illustration of (a) azimuthal phase and (b) intensity for Laguerre-Gaussian beam spots with various (ℓ, p) modes. Here $w(z) \equiv 1$, $C_{p,\ell} \equiv 1$, and $\Phi(z) \equiv 0$ was taken and the intensity was not normalized to the same scale for visual clarity at higher ℓ values.

Generation of OAM

As evident in equation (1.26) and Figure 1.14(a), the key properties of the orbital angular momentum of light arise from the modulation of phase in azimuthal direction. Therefore, precise spatial modulation of phase is the key to accurate OAM generation. In real space, the spatial phase modulation is equivalent to spatial optical path modulation. Therefore, cavity physics-based resonator approach,[61,62] nanofabrication-based metasurface approach,[63,64] and liquid crystal-based approach[65] have been employed to achieve tunable spatial phase modulation, with each of them has their unique pros and cons. For example, the cavity-based approach provides at-source modulation, [61,62] but direct tuning over the laser cavity is needed. Therefore, it is increasingly undesired in research that demands a high level of laser stability. While the titanium oxide nanopillar meta surface achieving a high purity of OAM light with astonishing $\ell = 100$,[63] there is no feasible way of tuning ℓ once the metasurface is made. On the contrary, the liquid crystal-based spatial light modulator (LC-SLM) struggles to provide $|\ell| > 10$ due to finite pixel resolution,[66] it provides most flexibility accommodating reasonable range of ℓ values and a relatively broad range of wavelength of the incident light. Furthermore, the ability to flexibly tune phase patterns can be integrated with various optical algorithms to enable precise control over spot focus and position. This provides a powerful and useful tool for light manipulation, as demonstrated in Chapter 5 of this thesis.

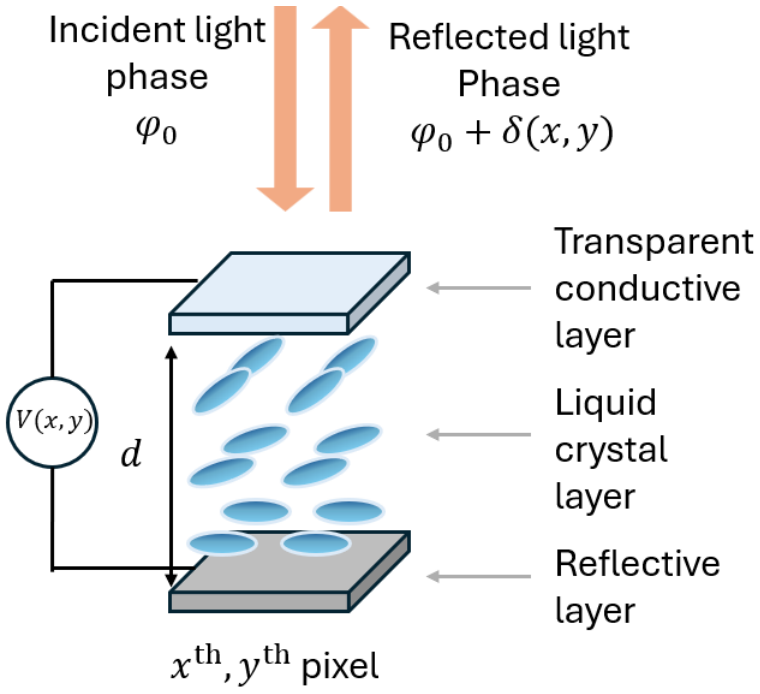

Figure 1.17 Typical structure of a pixel liquid crystal-based reflective spatial light modulator.

a typical pixel structure of LC-SLM is shown in Figure 1.17, where the phase modulation (δ) for the incident light of wavelength (λ) at pixel location (x, y) is[65]

$$\delta(x,y) = 2 \times \frac{2\pi}{\lambda} \int_0^d (n_e(\theta) - n_o) dz, \tag{1.27}$$

where d is the thickness of the liquid crystal layer, n_o is the reflective index of ordinary light, and $n_e(\theta)$ is the reflective index of extraordinary light) given by [65]

$$n_e(\theta) = \frac{n_e \cdot n_o}{\sqrt{n_e \sin^2\theta + n_o \cos^2\theta}}, \tag{1.28}$$

where θ is defection angle depending on the applied voltage (V) at pixel (x, y) of the panel, threshold voltage (V_C) for liquid crystal molecule, and scaling factor V_0: [65]

$$\theta(x,y) = \begin{cases} 0 & V \le V_C \\ \frac{\pi}{2} - 2\tan^{-1}\left\{\exp\left[-\left(\frac{V(x,y) - V_C}{V_0}\right)\right]\right\} & V > V_C \end{cases}. \quad (1.29)$$

The effective Jones matrix in the basis of $|n_e\rangle$ and $|n_o\rangle$ for an ideal SLM is thus

$$\begin{bmatrix} e^{-i\delta(x,y)} & 0 \\ 0 & 1 \end{bmatrix}. \quad (1.30)$$

Therefore, with a careful choice of $V(x, y)$ for the liquid crystal display, generation of OAM light with desired ℓ may be achieved.

Novel optoelectronic interaction using light with OAM

The light-matter interaction between light with OAM and optoelectronic materials are ultimately dominated by conservation of energy, linear momentum, and angular momentum. In macroscopic scale, angular momentum transferred from the incident light leads to rotation of micron-size graphite particles,[67] or manipulated single molecule or cell by an optical tweezer.[55,56]

In an even smaller scale, OAM of light exerts an effective centrifugal force on charge carriers, leading to circular photogalvanic effect and circular photovoltaic effect that may be used for energy harvesting in semiconducting materials.[68–70] In ML-MoS_2, K. B. Simbulan *et al*. demonstrated increased photovoltaic effect in ML-MoS_2 transistors where increased photocurrent was observed under light with higher OAM (Figure1.18(a)).[70] The OAM-dependent photoluminescence experiments showed a spectral blue shift due to the momentum transfer (Figure 1.18(b)).[71] Generally, twisted light-semiconductor interaction is formulated by G. F. Quinteiro and P.I. Tamborenea with a two-band model,[72] which

demonstrated that angular momentum carried by the light may increase accessible excited states in a cone-like fashion.

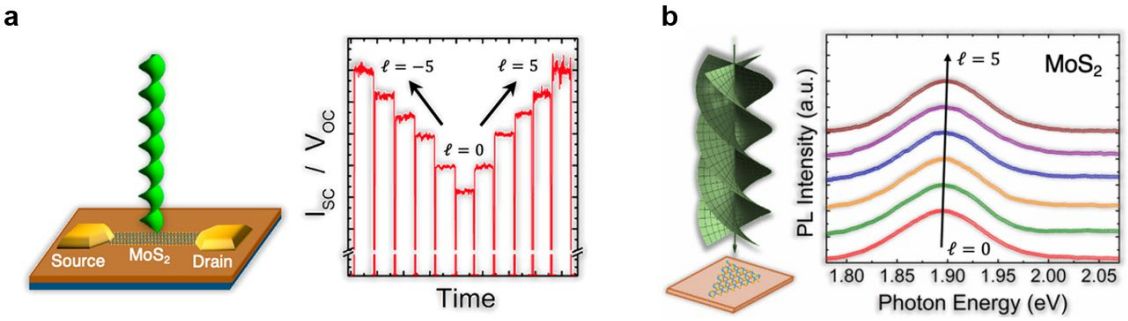

Figure 1.18 (a) OAM of light-induced photocurrent enhancement in ML-MoS_2 FET. Reprinted with permission from K. B. Simbulan, Y.-J. Feng, W.-H. Chang, C.-I. Lu, T.-H. Lu, and Y.-W. Lan, Twisted Light-Enhanced Photovoltaic Effect, ACS Nano 15, 14822 (2021). Copyright 2021 American Chemical Society. (b) Spectral blue shift of photoluminescence in ML-MoS_2 single crystal. Reprinted with permission from K. B. Simbulan et al., Selective Photoexcitation of Finite-Momentum Excitons in Monolayer MoS_2 by Twisted Light, ACS Nano 15, 3481 (2021). Copyright 2021 American Chemical Society.

The nature of the alternating electromagnetic field character of the light may affect electrical dipole and quadruple transition, leading to selection rule under OAM, even in the ultimately small scattering cross-section limit of an individual atom.[73] Christian T. Schmiegelow *et al.* first observed the predicted selection rule under OAM light in $^{40}Ca^{+}$ ion as shown in Figure 1.19(a).[73,74] L.A. Sordillo *et al.* found varying degree of polarized electron under different SAM and OAM in GaAs device, where the optical selection rule shown in Figure1.19(b) was tested.[75]

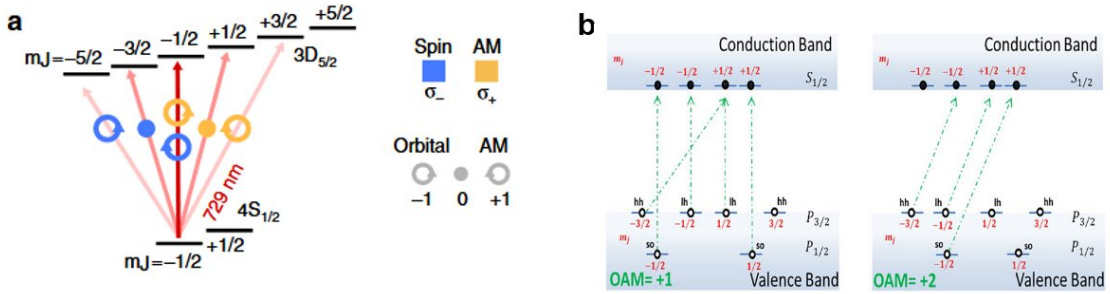

Figure 1.19 Transition selection rules associated with the OAM of light. (a) Optical transition rules between $4S_{1/2}$ states to $3D_{5/2}$ states in $^{40}Ca^{+}$ ion system and GaAs system. Reprinted from ref.[74] under CC-BY license. (b) Optical transition rules for light with OAM $\ell = 1$ (left) and $\ell = 2$ (right). Reprinted from L. A. Sordillo, S. Mamani, M. Sharonov, and R. R. Alfano, The interaction of twisted Laguerre-Gaussian light with a GaAs photocathode to investigate photogenerated polarized electrons, Applied Physics Letters 114, 041104 (2019), with the permission of AIP Publishing.

In summary, the orbital angular momentum of light may be used to tune light-matter interaction in semiconducting materials and are primarily focused on angular momentum transfer to photoexcited electrons. Therefore, it would be very interesting to investigate twist light interaction with other quasiparticles in quantum materials, such as excitons, exciton polaritons, or plasmon polaritons.

Chapter 2

MATERIAL SYNTHESIS AND DEVICE FABRICATION

2.1 Introduction

Controlled synthesis of high quality 2D material and consistent nanofabrication procedure are vital for their application.[76–78] To achieve the ultimate goal of real-world manufacturing, a scalable approach must be taken in all processes.

In terms of materials synthesis, pulsed laser deposition (PLD),[79] molecular beam epitaxy (MBE),[80,81] atomic layer deposition (ALD),[82–84] and chemical vapor deposition (CVD) [76,77,85] as well as its variants such as plasma enhanced chemical vapor deposition (PECVD)[76,86,87] and metal organic chemical vapor deposition (MOCVD)[88–90] are techniques capable of producing large-scale 2D materials.[77] Among those available techniques, the ALD, PECVD and MOCVD methods offer bottom-up solutions for wafter-scale synthesis and are most feasible for industrialization because they are capable of delivering uniform thin films with high crystallinity on a variety of substrates without the need of excessively high growth temperature, while being cost-effective.[77] In this chapter, we will discuss PECVD growth of ML-graphene in Section 2.2 and thermal CVD synthesis of MoS_2 in Section 2.3. Meanwhile mechanically exfoliated 2D materials by adhesive tapes, although intrinsically non-scalable, played an important role in understanding 2D materials in the clean limit. The tape-assisted approach has been the primary driving force for the discoveries of important phenomena the 2D materials such as integer (fractional) quantum Hall effect,[9,91] unconventional superconductivity[92], and unconventional ferroelectricity.[93] Thus, we used measurements on mechanically exfoliated ML-graphene and TMDs as an important benchmark for our studies of PECVD-grown ML-graphene and CVD-grown ML-TMDs in this thesis, which are detailed in Section 2.5 and Section 3.8.

After synthesizing 2D materials, we characterized them using various techniques to ensure high quality materials. A summary of these techniques used in this thesis is provided in Section 2.5. Nanofabrication techniques for material transfer and device fabrication, such as electron-beam lithography, reactive ion etching, and metal deposition are covered in Section 2.6. Finally, electrical transport measurement configuration and setups is discussed in Section 2.7.

2.2 Plasma-enhanced chemical vapor deposition of ML-graphene

Plasma-enhanced chemical vapor deposition (PECVD) is known to be a controlled deposition of high-quality ML-graphene over various substrate and surfaces[76,94–96]. It provides a rich chemical reaction environment with a mixture of radicals, ions, and molecules, enabling substrate oxide etching and low-strain, low-defect ML-graphene growing at low temperature[97]. Our original experimental setup is shown in Figure 2.1, which was slightly modified for this thesis work by adding a high-resolution low-flow-rate mass flow controller (MFC, ALICAT, MC-10SCCM) in parallel to traditional leak valve and mass flow controller line for methane.

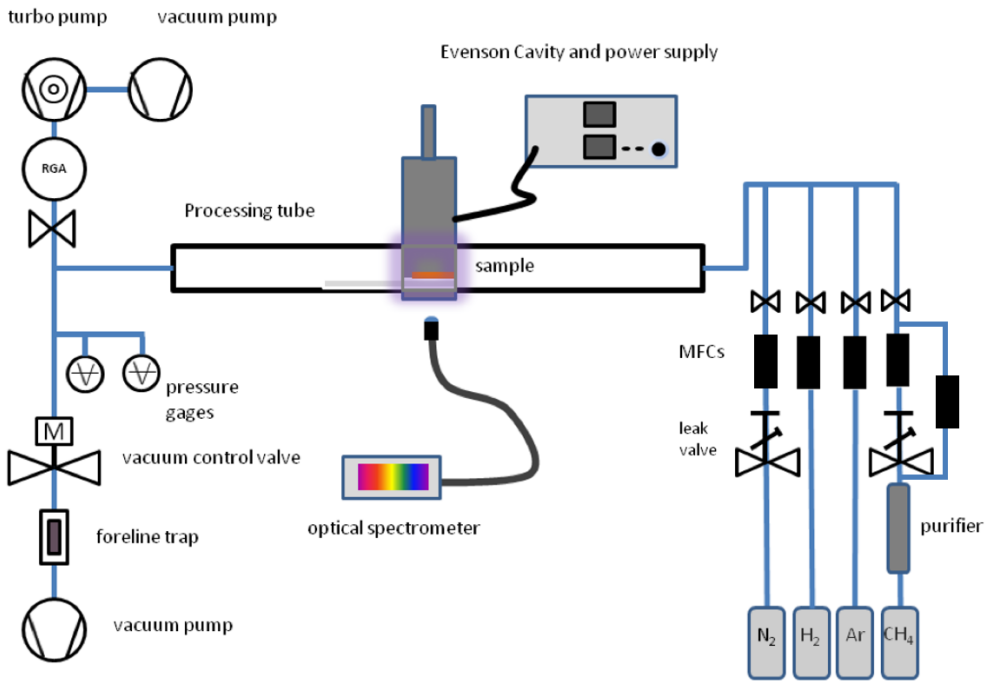

Figure 2.1 Schematics of plasma-enhanced chemical vapor deposition (PECVD) system. Adapted from ref.[97]with permission from Springer Nature.

Preparation

To minimize contamination, the half-inch diameter quartz processing tube and the quartz sample carrier were first cleaned with acetone, isopropanol (IPA), rinsed by deionized (DI) water, and then baked dry at 100 °C in an oven dryer. If the processing tube and quartz carrier were used in a previous run and coated with carbon and copper, 70% nitric acid followed by a DI water rinse are used before the cleaning procedures described above would be carried out to ensure a clean growth environment.

Copper foil (Alfa Aesar, P/N 10950, 0.025 mm thickness, 99.999%) were used as a substrate for growth, which was kept in an argon gas-filled glovebox (<0.01 ppm water and oxygen). The copper foil was first cleaned by an ultrasonic cleaner in acetone and IPA for 15 minutes

each. Then the foil was cut into a typical rectangle shape of 1.2cm ×0.7cm with the top-right corner cut off by using a clean scissor. To minimize undesired deformation during cutting, the foil was carefully hold with two clean microscope slides and only the desired amount of copper foil to be cut was exposed. The corner cut at the top-right was to help identify the side of the foil with ML-graphene after growth. The foil was subsequently flattened by sandwiching it between two clean microscope slides and carefully applying forces with fingers.

All sample handling tools, including tweezers, quartz carrier loader, microscope slides and scissors, must be cleaned in DI water, acetone, IPA, (ultrasonic cleaner, 15 minutes each) prior to the experiment and must covered with a Kimwipe whenever not in use.

Pre-growth plasma cleaning

After loading the quartz tube and quartz sample carrier and properly adjusting its levelness, the system is pumped down to a base pressure (<3 mTorr) for 15 hours. It is also wise to pump down the residual gas analyzer (RGA) and start the recording such that a stabilized baseline composition of the environment is recorded at the end of the following process.

Close the side valve to the RGA and begin flowing O_2 (with a flow rate of 2sccm) and Ar (5sccm) until the chamber pressure reaches the setpoint of 500 mTorr. Wait at least 2 minutes to establish a steady flow. With RF power of 50 W, first stabilize then gradually move the Evenson cavity along the quartz tubing to clean the chamber and quartz sample carrier with O_2 plasma for a total of 30 minutes. Adjust the positioning of the Evenson cavity, its ceramic tuning handle, and threaded tuning stub at its top to minimize the reflection power. Typically, under 50 W forward power, the reflected power should be less than 3 W at this stage. Ensure the plasma head stays at the growth position of the quartz sample carrier for more than 2 minutes. Pump down the residue gas while flushing the chamber with Ar. Repeat the procedure with H_2 plasma, using H_2 2 sccm and Ar 5 sccm. Vent the chamber and load the

sample using cleaned quartz sample carrier. Adjust the position of the copper foil after loading using the quartz sample carrier loader, making sure that the copper foil stays at the center of the quartz sample carrier. Pump down to base pressure and then open the side valve to RGA until the reading from the filament stabilizes. Record the base composition.

ML-graphene growth by PECVD

Set the H_2 flow rate to 2 sccm and chamber pressure of 500 mTorr. Gently ramp up the CH_4, and N_2 MFCs to the open position so that the respective leak valve will be in primary flow control. With the reading from the RGA, gently adjust the CH_4 and N_2 leak valves such that the desired partial pressure ratio of about $CH_4/N_2 = 1.6 \sim 1.8$ is achieved. Note that a lower ratio would lead to a higher cyano radical concentration during the growth, and therefore would result in etching excess copper foil other in addition to removing the surface copper oxide. Practically in a 10-minute growth with 40W of plasma, if the CH_4/N_2 ratio read prior to the growth is below 1.5, there would likely be either no copper foil left after the growth, or there are plasma-etched holes everywhere on the copper foil such that the sample became useless for transfer purposes. For each adjustment, wait for at least 20 minutes, which is about three times the exponential decay constant for the partial pressure reading in RGA after each incident of MFC/leak valve change, to ensure that the RGA reading is stabilized. Ignite the plasma at 40 W forward power at the downstream of the sample, and gently move the plasma on to the sample position. Wait for a desired period. Turn off plasma power and pump down the residue gas to immediately stop the process. Repeat the growth procedure from downstream to upstream at all sample locations. Finally, vent the chamber using Ar gas with a slowly ramping flow rate manner to avoid foil being carried by the sudden blast of flow.

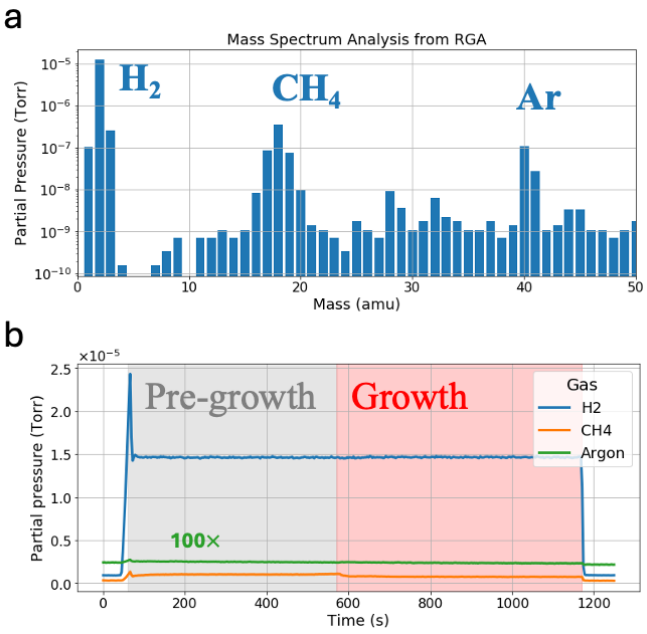

Figure 2.2 Typical RGA data during the ML-graphene growth by PECVD. (a) Snapshot of gas partial pressure captured using mass spectrometer mode of RGA at the end of pre-growth stabilization process. (b) H_2, CH_4, and Ar partial pressure recorded over a typical growth cycle.

The RGA recording for a typical growth cycle is shown in Figure 2.2. Another heuristic indication of a successful growth would be the deposition of copper on both the quartz tube and the quartz sample carrier, as shown in Figure 2.3. If a high resolution MFC for CH_4 is used instead of the leak valve, the optimal flow rate setpoint should be around 0.001 sccm and the nitrogen flow rate is controlled by the leak valve according to the partial pressure measured.

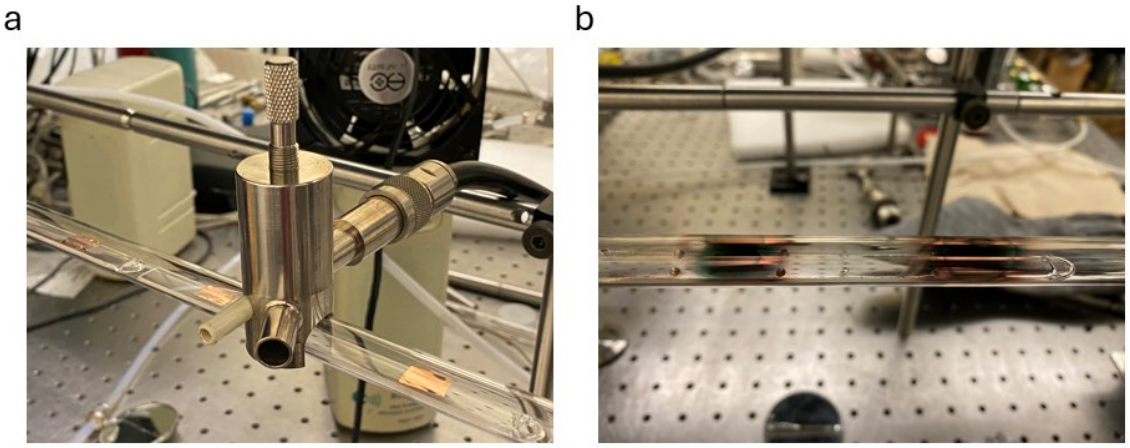

Figure 2.3 Photograph of the quartz tube before and after ML-graphene PECVD. (a) Cleaned quartz tube before growth. (b) Typical copper deposition inside the quartz tube after the PECVD growth of graphene, showing a shiny orange-red color.

2.3 Chemical vapor deposition of MoS_2

Chemical vapor deposition of 2D materials has been a very popular method of 2D material synthesis, which covers a variety of III-V compounds with controllable growth of various structural phase and number of layers.[85,98] The principle of the CVD process is similar to the PECVD process mentioned above, where vaporized precursors react and form a target crystalline structure at the surface of substrate, whose lattice constant usually matches that of the target to promote deposition. The differences between CVD and PECVD methods are mainly the source of energy that initiates the chemical bond-breaking of the vaporized precursors. For example, in the deposition of ML-graphene, the former is provided by heat transfer from furnace, which is usually maintained around 1000 ºC during growth,[99] whereas the latter is from electromagnetic microwave by a microwave generator, enabling a lower growth temperature around 160 - 425 ºC depending on the microwave power.[97]

In this thesis, the ML-MoS_2 samples were mostly synthesized on sapphire substrates using the thermal CVD method similar to previous articles.[100–102] by Dr. Yann-Wen Lan's group at the national Taiwan Normal University unless otherwise specified. The main steps were summarized below based on Dr. Lan's narrative and my experience growing and observing 2D materials at Dr. Yeh's group at California Institute of Technology.

1. Clean three quartz boat and a desired sapphire substrate by acetone and IPA.

2. Put 0.6 g of MoO_3 at the center of the quartz boat and place the loaded boat at the center of the furnace.

3. Load another quartz boat with sulfur and place it upstream of MoO_3 boat right outside the furnace. This is typically 18~20cm distance. Wrap the quartz tube with heating tape at the location of the sulfur boat. Since the CVD growth of MoS_2 requires a sulfur-rich environment, the amount of sulfur placed in the boat is not critical as long as it is reasonably excessive.

4. Place the sapphire substrate over an upside-down quartz boat and place the boat near the downstream of the MoO_3 boat.

5. Pump down the quartz boat base pressure to remove air and moisture. Flow 70 sccm of Argon gas while maintaining 40 Torr of chamber pressure.

6. Heat up the furnace at a rate of 32 ºC/min to 750 ºC (Typical range 700-850 ºC) and maintain for 15 minutes for crystal growth. Preheat the heat tape such that the sulfur boat is maintained at 190 ºC throughout the 15-minute growth period.

7. Pump down the chamber to stop the growth process immediately and allow the furnace to cool down naturally.

2.4 Exfoliation of 2D materials

While this thesis aims to investigate scalable technologies for future applications, significant efforts have been made to optimize process consistency and minimize contamination using existing instrumentation at California Institute of Technology. However, under typical research laboratory conditions, 2D materials obtained through dry exfoliation and devices fabricated with hexagonal boron nitride (h-BN) encapsulation are still expected to exhibit better intrinsic characteristics. Therefore, in addition to PECVD grown and CVD-grown materials, exfoliated 2D materials were also studied as a reference. Here we use the Scotch tape method to exfoliate ML-graphene, h-BN, and MoS_2 following the exfoliation methodology for these materials commonly described in literature. The mechanically exfoliated MoS_2 sample will serve as an example for discussion in this section.

1. Prepare diced SiO_2/Si chips of 2cm×2cm size. Scratch one corner with razor blade for consistent identification of the chip direction. Clean the substrate using an ultrasonic cleaner with DI water, acetone and IPA for 15 minutes each. Blow dry the substrate with a nitrogen gun gently. Prepare the substrate with O_2 plasma (PIE Scientific, Tergeo Plus) of 150W, 6 sccm flow rate for 2 minutes under immersion mode. Quickly put the substrate on a standard microscope slide with double-sided tape.

2. Prepare a Scotch tape (3M, Magic) of 15cm long (as the “mother tape”) on a cleaned and flat table surface with tape side up. Visually examine the uniformity of the glue layer of the tape and make sure there is no obvious bubble and dust contamination. Fold ~1cm of the tape at each end for handling. Tape it on the table. Put on bulk crystal of MoS_2 (2D Semiconductors, BLK-MOS2-SYN-FLX) that is thin and flat on both sides at one end of the mother tape. Fold and exfoliate the mother tape a few times to scatter the bulk crystal to cover an area of 2cm×2cm. This usually takes 3~5 times. For the sake of documentation, assume it takes 5 times to spread and denote the tape as #5.

3. Prepare a scotch tape of ~7cm long (as a "son tape") and tape over one end of the mother tape (#5). Exfoliate. This son tape may be the new mother tape if necessary (denote as #5.6 since it was the 6th exfoliation from the mother tape #5). Fix it on the table with crystal side up with additional tape and treat it as new mother tape if necessary.

4. Prepare additional son tape and exfoliate until one has a series of son tapes (#7, # 8, …), as shown in Figure 2.4. Stop at the desired thickness or if there is visually nothing left on the son tapes. Find the best son tape from the thinnest to the thickest by stamping the son tape on the prepared SiO_2/Si substrate (described below) and visually examining the yield rate of monolayer per chip. Stop at son tape (for example #11 in Figure 2.4) with desired yield rate.

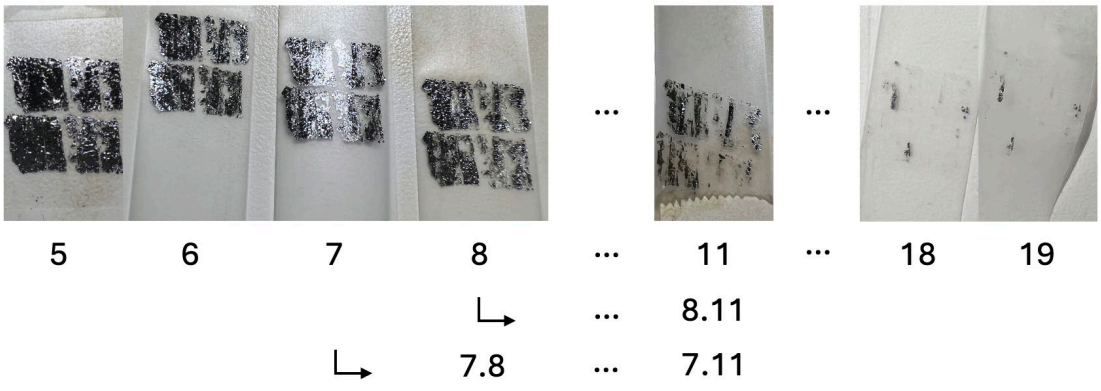

Figure 2.4 Photograph of a typical son tape series during bulk MoS_2 exfoliation.

To stamp on the SiO_2/Si substrate, first align and stamp the crystal area of the son tape with the substrate and then cover with another layer of tape for protection purposes. Press on with cotton-head swab (Puritan 806-WC) as heavy as possible to promote adhesion and remove all bubbles. Wait for about 5 minutes and then heat it with a hot plate at 115 ºC for 1 minute. Put it on the table to cool for about 10 seconds, then remove the son tape by pulling the protective tape as slow as possible. Examine the yield rate under optical microscope by comparing the optical color and contrast with sample of known thickness.

5. Now use existing son tape series and an additional new son tape to achieve the same optimal number of exfoliations, i.e. exfoliate one more time on #10 so two of the #10.11 will be achieved. Similarly, obtain #7.11, #8.11 and so on for further production.

A similar procedure may be followed for exfoliation from HOPG (2D Semiconductors, BLK-HOPG) and bulk h-BN (2D Semiconductors, BLK-hBN-LG). However, there are two exceptions for exfoliating h-BN. Firstly, minimal forces should be applied during the step of cotton-head swab pressing. Secondly, a different type of Scotch tape (3M, Magic Greener) with higher adhesion is preferred for making the mother tape. Optical microscope image of typical exfoliated 2D materials is shown in Figure 2.5.

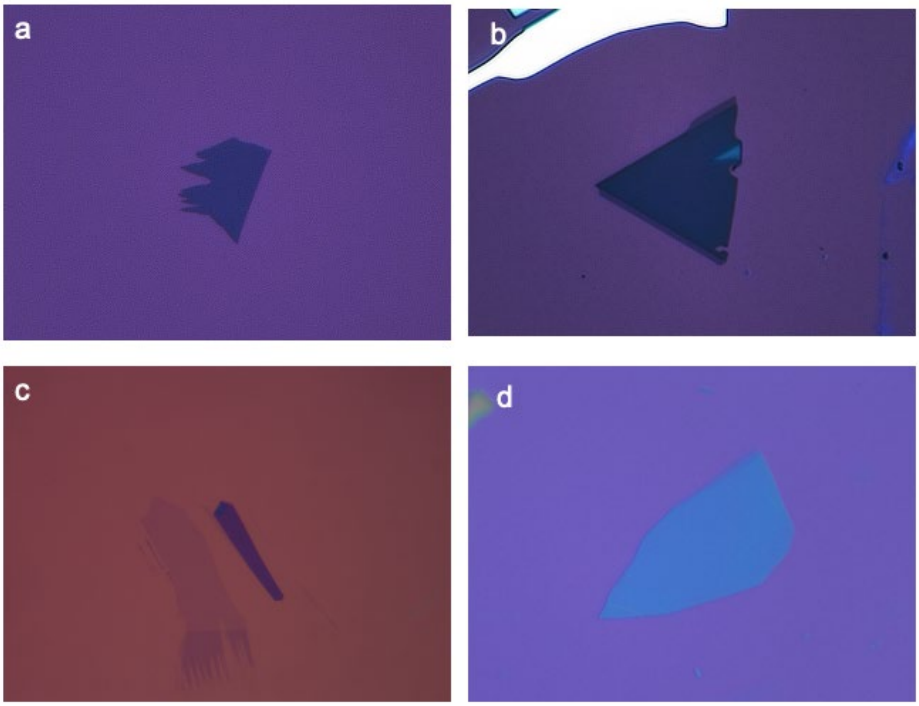

Figure 2.5 Optical image of exfoliated 2D materials. (a) Monolayer MoS_2 (b) Bilayer MoS_2. (c) ML (left) and few layer (right) graphene. (d) h-BN.

2.5 Basic characterization of 2D materials and its devices

After sample synthesis, Raman spectroscopy and photoluminescence (PL) spectroscopy experiments were performed to verify the sample quality. The Raman spectroscopy and PL spectroscopy experiments were performed over Raman microscope (Renishaw InVia) at Mineral Spectroscopy lab at Caltech under the excitation of 514nm laser with a grating of 1800 lines/mm or 3000 lines/mm. Typical Raman spectra of as-grown ML-graphene on cp[er foil was shown in Figure 2.6(a), where a strong copper background is seen besides ML-graphene's signature D, G, and 2D Raman mode manifested as peaks located near 1353 cm^{-1}, 1587 cm^{-1}, and 2685 cm^{-1}, respectively. Sample with a low D peak intensity are selected for transferring process, and a representative Raman spectrum is shown in Figure 2.6 (b).

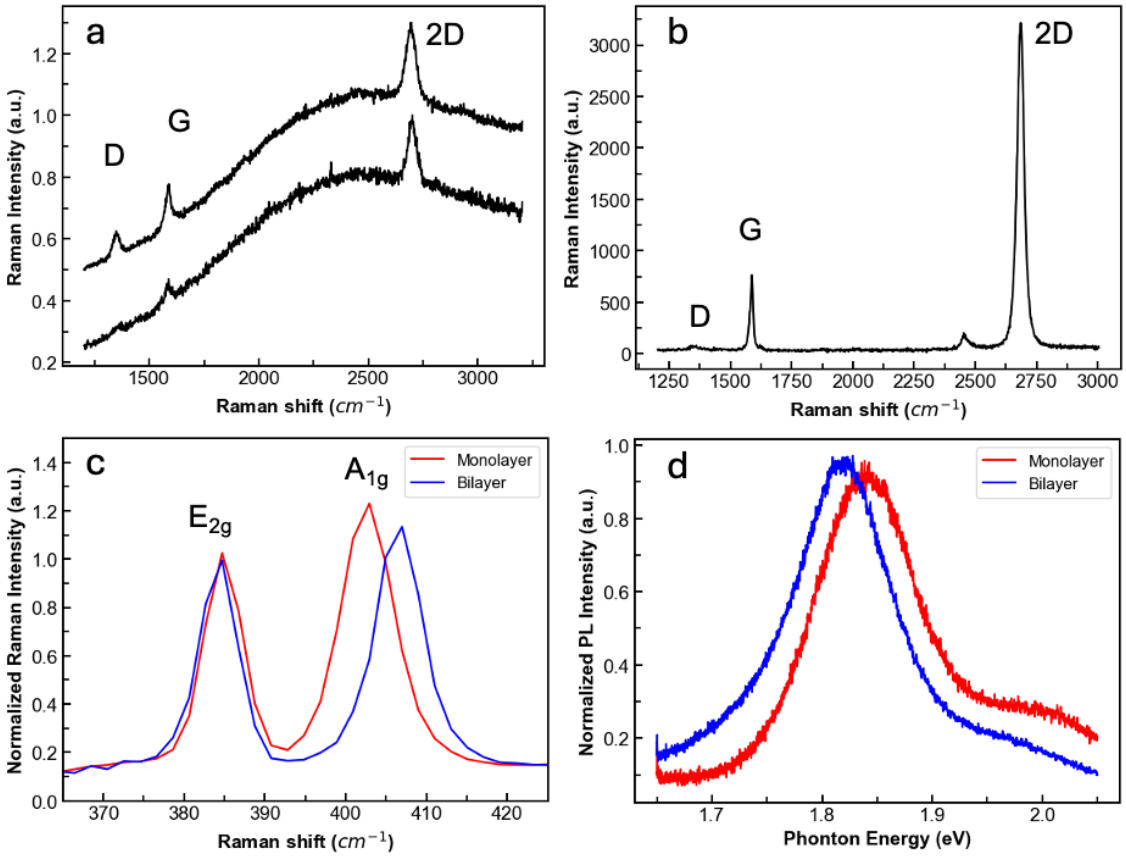

Figure 2.6 Raman spectroscopy and photoluminescence spectroscopy characterization over ML-graphene and MoS_2 samples. (a) Typical Raman spectroscopy of an as-grown ML-graphene on copper foil. The spectra were vertically offset by 0.3 for clarity. (b) Raman spectroscopy of ML-graphene after transferred to SiO_2/Si substrate. (c) Raman spectroscopy of monolayer ML-MoS_2 (solid line) and bilayer MoS_2 (dashed line) on SiO_2/Si substrate. (d) Normalized photoluminescence spectroscopy of ML-MoS_2 and bilayer MoS_2 after device fabrication.

The exfoliated sample is first classified by its color and contrast on SiO_2/Si substrate under optical microscopy (customized dry transfer stage in the Yeh group and Keyence, VHX-7000 at the Kavli Nanoscience Institute, Caltech), and then verified by Raman spectroscopy

(Figure 2.6(c)). The separation between the two prominent Raman peaks, i.e. the E_{2g} and the A_{1g} Raman peak was used to distinguish monolayer (17~19 cm^{-1}) and bilayer (~22 cm^{-1}).

Atomic force microscopy (AFM) was used to study the topography of the devices as exemplified in Figure 2.7. They were also used to study the surface topography of ML-graphene, which was transferred to nanostructures. Furthermore, scanning the device using the contact mode of AFM may be useful to clean the polymer residue over the 2D material surfaces.

AFM topography experiments were performed over Bruker Dimension Icon setup at the Kavli Nanoscience Institute (KNI) and the Molecular Materials Research Center (MMRC) at Caltech, using noncontact peak force tapping mode with a commercial AFM probe (Bruker, SA-AIR, SA-AIR-HPI for non-contact topography and TESPA-v2 for contact-mode cleaning). Kelvin probe force microscopy (KPFM) measurements were performed over Bruker Dimension Icon setup at the MMRC using a conductive AFM probe (Bruker, PFTUNA) with a customized PC Board to obtain spatially dependent work function of the material.

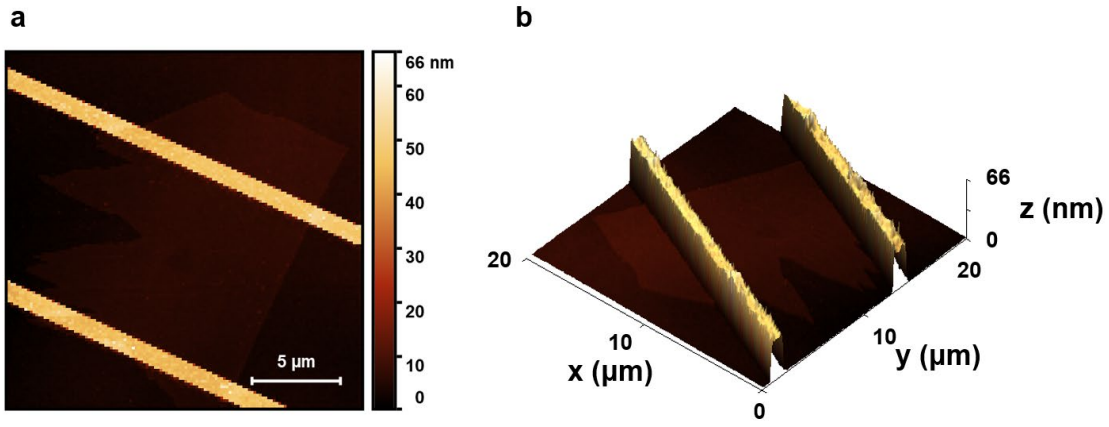

Figure 2.7 (a) AFM topography and (b) 3D reconstruction of the ML-MoS_2 device.

Scanning electron microscopy provides another aspect of sample surface topographic information through secondary electrons. It was such a frequently used tool that there were more than 4812 SEM images taken for this thesis work, with an accumulated image exposure time exceeding 30 hours in total. The applications of images may be mainly divided into three categories as shown in Figure 2.8.

For the synthesis MoS_2 and ML-graphene, SEM topography was used to image the time evolution of sample growth by stopping the CVD process at different growth times and then examining the SEM images of the resulting sample surface, which leads to the discovery of an intriguing self-assembly process in MoS_2. The spatially dependent energy dispersive X-ray spectroscopy (EDS) was used to examine the atomic composition of the unknown substance appearing on the sample surface; thus helping identify and then eliminate the potential contamination sources to ensure clean synthesis of ML-graphene growth by PECVD. In the process of nanofabrication, SEM imaging was used to provide process check points, assist wet-etching process of nano-pillars and provide insights into process failure analysis over the entire process of device nanofabrication. Gallium focused ion beam (FIB) was used to mill down the excessive metal that caused accidental short of contacts in the rare case of lift-off failure, or to create a sample cross-section for providing a fresh view angle of the sample. Furthermore, SEM topographic imaging played a vital role in device characterizations. For example, a topographic study of the transmission line method (TLM)-style contacts lithographed under linearly scaled electron area dose (between 600 to 1400 $\mu C/cm^2$ with step of 50 $\mu C/cm^2$) help select the best area dose for making fine structures with feature size less than 30nm. Topography images over a ML-graphene sample that was transferred over periodic nano pillars showed periodic ridges-like structures and provided information about regions with crack formation due to excessive local strain.

It is worth noting that the line-by-line scanning nature of the SEM image exposure may also be exploited to provide information on contact electrical connectivity in a ML-graphene

device: During the process of obtaining a large-scale topography image of the device, about 2.7×10^{-6} μC/cm^2 area dose (98pA, 30μs exposure per pixel with field of view of 4mm by 4mm) was deposited to the metal contacts sequentially so that the top-most contacts were imaged first and the bottom-most contacts were imaged last. If the top and bottom contact were electrically well connected, by the time the scanning electron beam reached the bottom contact, the accumulated charge transferred from the top contact to the bottom contact via the ML-graphene device, would deflect the electrons and cause the bottom contact to appear darker than the top contact in the resulting image. The electron damage during this process should be minimal as its area dose (10^{-6} μC/cm^2) was orders of magnitude smaller than the effective area dose (10^2 μC/cm^2) typically required to penetrate the ~400nm-thick PMMA layer and reach the ML-graphene layer during e-beam lithography.

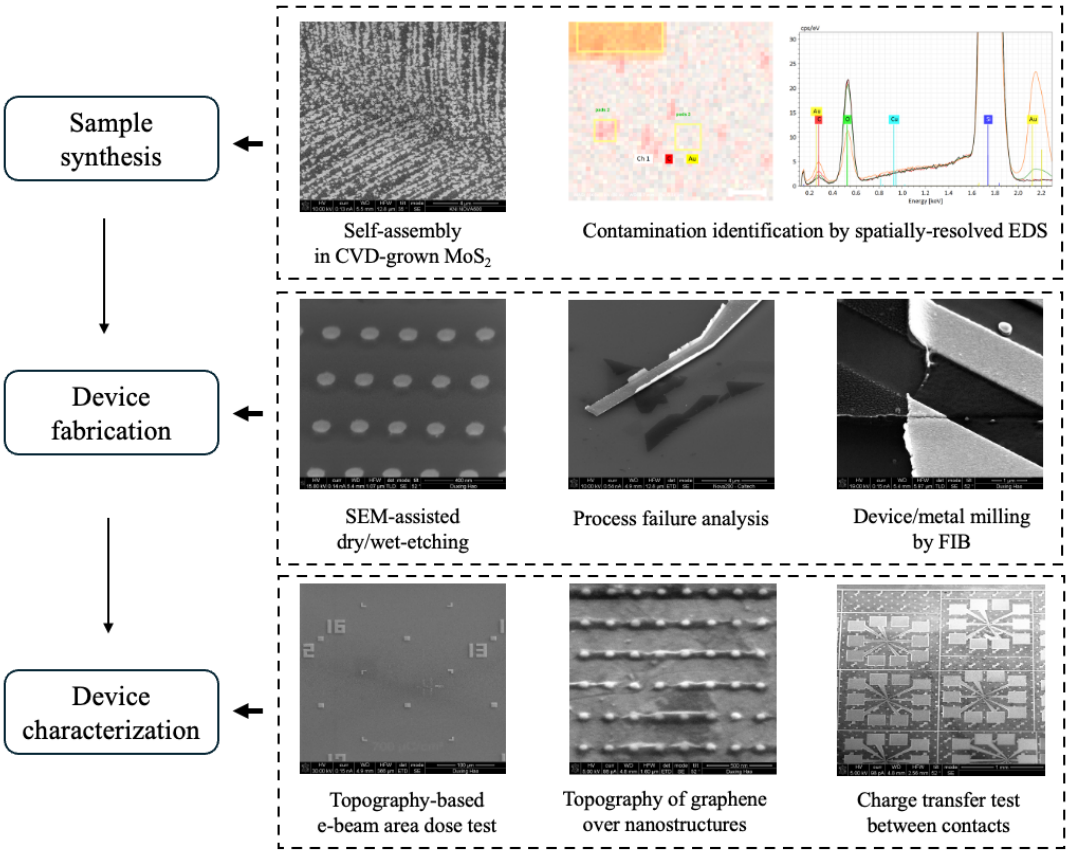

Figure 2.8 Typical applications of scanning electron microscopy (SEM) and its related technology employed in this thesis.

These experiments were performed with different SEM systems, including Thermofisher Quanta 200F and Thermofisher Nova200/600 NanoLab at KNI. For 2D materials, the SEM imaging was generally carried out either at a sacrificial site or after all other non-destructive experiments were completed, with a low electron energy and current setting typically at 5kV and 98pA, respectively. For metal contact/thin film characterization, 30kV with 1nA may be used to achieve higher resolution of the surface or cross-section. The gallium focused ion beam (FIB) milling of Ti/Au contacts employs a 30kV gallium ion beam of 0.3nA.

2.6 Nanofabrication processes

Wet transfer of ML-graphene and h-BN

The ML-graphene grown by PECVD method was transferred to a standard SiO_2/Si marker substrate using the PMMA-assisted method as follows:

1. Clean the substrate with acetone/IPA via sonicating for about 10 minutes each and then blow it dry.

2. Pre-bake the copper chip at 180 ºC for 60 seconds. Use acetone to clean the o-ring that will host the copper foil. Take the ML-graphene/Cu chip and spin-coat PMMA 495A4 at 2000prm. Post-bake the PMMA-coated sample at 180 ºC for 60 seconds. The result is shown in Figures 2.9 (a) and 2.9(b).

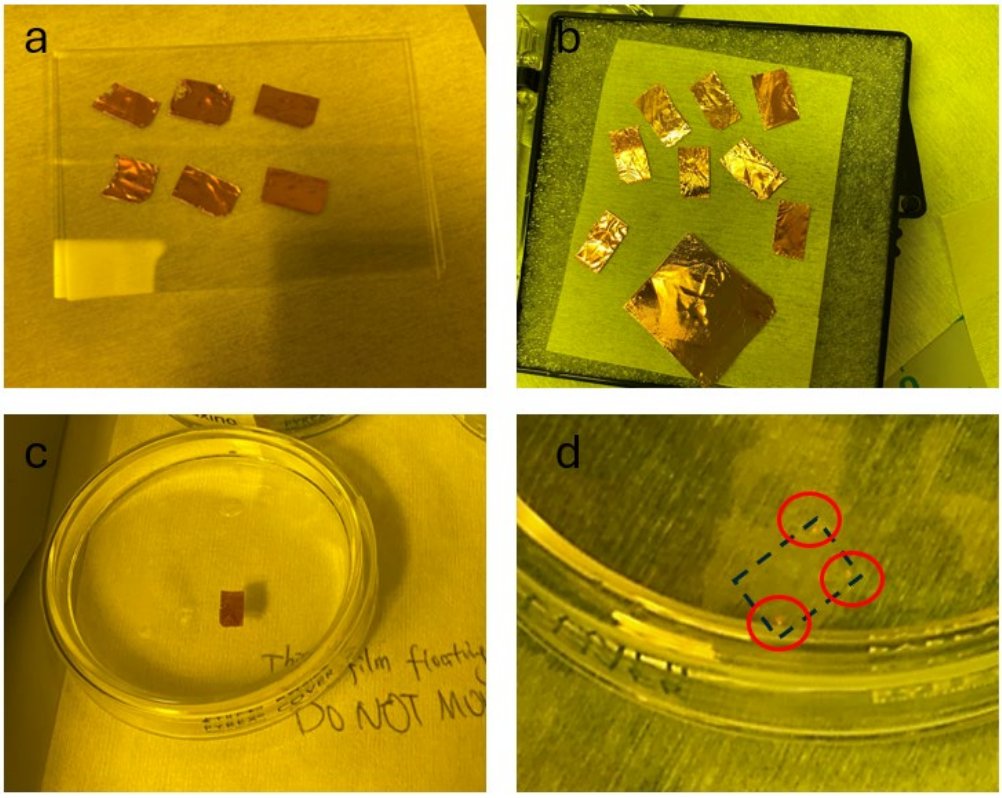

Figure 2.9 PMMA-assisted wet transfer of 2D materials. (a) PMMA-coated ML-graphene on copper foil. (b) PMMA-coated ML h-BN on copper foil (c) PMMA-coated ML-graphene floating on the copper etchant. (d) About four hours after wet etching, only PMMA/ML-graphene (blue dashed line) was floating with residue copper at corners (red circle).

3. Use O_2 plasma (Plasma-therm, SLR 720) to clean the graphene on the unprotected backside at 20 mTorr total pressure,10 sccm flow of O_2, and 80 W power for 60 seconds. Alternatively, use Q-tip to drip ammonium persulfate 0.2M and rub the backside of the copper foil until a new shiny layer of copper is seen.

4. Fresh 0.2M ammonium persulfate solution is used as the copper etchant to fill half of a standard petri dish. With the PMMA-coated side up, put the chip in the etchant for about 1~3 hours (Figure 2.9(c)).

5. Prepare three beakers filled with DI water. Use a spoon to carefully transfer PMMA/ML-graphene to DI water. Do it three times to fully rinse the PMMA/ML-graphene. When spin-coating PMMA, there is an inevitable chance that some PMMA will accumulate on the backside of the chip, particularly near the corners. In these regions, the PMMA forms a sandwich-like structure with the copper, making it difficult to etch. As a result, residual copper remains at the corners, serving as a precise indicator of their position (Figure 2.9(d)).

6. Scoop up the PMMA/ML-graphene film using a target substrate that is pretreated with O_2 plasma. Let the chip dry overnight and then soak the chip in acetone overnight followed by IPA rinse. Blow the chip dry carefully by a nitrogen gun. One must not use a hot plate to bake the chip because this process would most likely (with nearly 100% probability) break those ML-graphene sheets transferred to substrate with nanopillar array.

Similar procedures may be applied to h-BN. For CVD-grown over MoS_2 SiO_2/Si or sapphire substrate, pre-cut three and a half sides of the PMMA along the chip edge before soaking in etchant of 3M NaOH (for SiO_2/Si substrate) heated to 65 ºC for 10 minutes in a hot bath of 14.5% ammonia solution (for sapphire substrate) at room temperature for 30 minutes to 2 hours. The transferred MoS_2/SiO_2/Si sample is then cleaned by N-methyl-2-pyrrolidone (NMP) solution heated to 70 ºC for 30 minutes in a hot bath and followed by IPA rinse.

Electron-beam Lithography

Current (nA)	Aperture (μm)	Resist	Area dose ($\mu C/cm^2$)	Application
0.15	300	PMMA 495 A4 (4000 rpm) / PMMA 950 A4 (4000 rpm)	700-900*	Very fine TLM pattern with 30nm contact spacing.
0.5	300	PMMA 495 A2 4000 rpm	850*	Nanodot arrays of diameter 20-50 nm.
3	300	PMMA 495 A4 (4000 rpm) / PMMA 950 A4 (4000 rpm)	1300	Fine area of RIE process pattern for etching. Fine electrical connections. Chip identifiers.
100	300	PMMA 495 A4 (4000 rpm) / PMMA 950 A4 (4000 rpm)	1100	RIE pattern, electrical contact pads and electrical connections with feature size > 10 μm.
200	400	PMMA 495 A4 (4000 rpm) / PMMA 950 A4 (4000 rpm)	1100	Wafer scale writing of standard markers.

Table 2.1 Typical e-beam lithography current profile and its typical application in this thesis. *Depending heavily on specific pattern/PEC profile therefore practically determined by the pattern/PEC-specific dose test.

The electron-beam lithography is performed over dedicated electron beam pattern generator (Raith, EBPG 5200/5000+) 100kV at KNI. The electron beam lithography process typically uses different current and aperture combinations for various feature sizes and choice of resist, which are summarized in Table 3.1. For patterns with feature size <100nm, proximity effect correction (PEC) was achieved by importing resist/substrate-specific electron scattering profile obtained by Monte Carlo simulation (GenISys, Tracer) to layout software (GenISys, Layout Beamer) and utilizing shape/corner-specific proximity effect correction algorithm. With the proximity effect correction, a pattern-specific electron dose test was performed to find the optimal area dose.

After e-beam exposure, the sample is then developed in Methyl isobutyl ketone (MIBK):IPA=1:3 solution for 60 seconds and soaked in IPA for another 60 seconds. The sample is then blow-dried by nitrogen.

Reactive ion etching

The silicon oxide etching was achieved using C_4F_8/O_2 (40/3sccm) plasma over reactive ion etching setup (Oxford Instruments, Plasmalab System 100). The process was performed at 7 mTorr, ICP Generator power of 2100W and RF forward power for 200W. The etch rate was measured by linear fitting etch rate curve as shown in Figure 2.10(a) and did not show a discernable difference between wet oxide (University Wafer) and dry oxide (Sil-tronix). The thickness of the SiO_2 layer before and after etching was measured using spectroscopic reflectometry (Olympus, BX51M and Filmetrics, F40, calibrated over a 1266.6nm known SiO_2/Si sample).

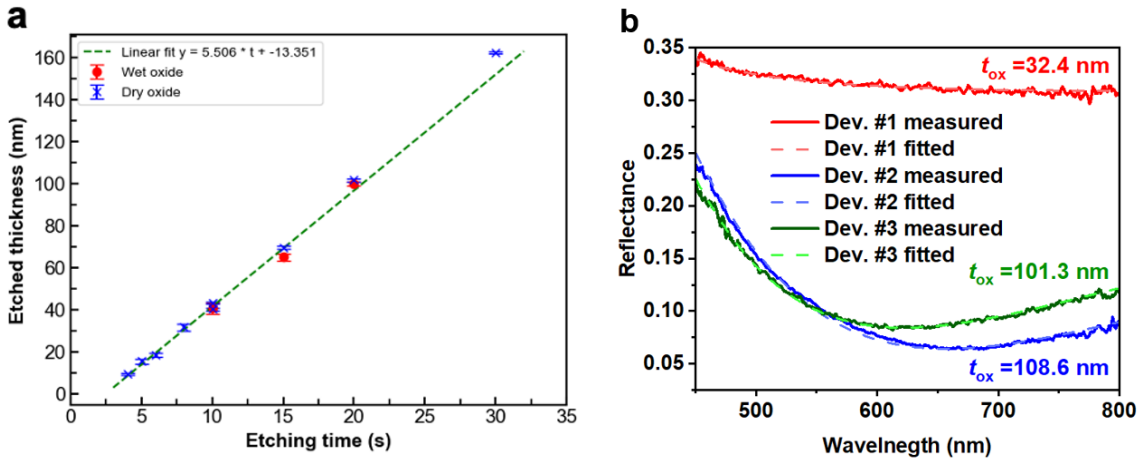

Figure 2.10 Measurement of etch rate of SiO_2 by reactive ion etching. (a) Etched thickness versus etching time yielded etch rate about 5.5 nm/s. (b) Typical spectroscopic reflectometric measurements of SiO_2 thickness tox for three devices. The solid lines were the measurement data and the dashed lines were the numerical fitting results.

The ML-graphene/graphite etching was achieved using O_2 (10 sccm) plasma over reactive ion etching setup (Plasma-Therm, SLR 720). The process was conducted at a pressure of 20 mTorr with 80 W plasma power, and the process time varied between 45 seconds to 120 seconds depending on the sample thickness and was usually done with a 15-second increment followed by visual check over optical microscope after the initial 45-second etch.

The h-BN and MoS_2 etching was achieved using CHF_3/O_2 (40/4 sccm) plasma over reactive ion etching setup (Plasma-Therm, SLR 720). The process was carried out at a pressure of 40 mTorr with 60 W plasma power. Alternatively, the process may be carried out in SF_6/O_2 (20/20 sccm) plasma using Plasmalab System 100 at a process pressure of 100mTorr and 1500/100 ICP Generator/ RF forward power. The process time varied between 30 seconds to 90 seconds depending on the sample thickness and was usually done with a 15/5-second increment followed by visual check over optical microscope after the initial 30 second etch.

Metal deposition

After the device geometry was patterned by the reactive ion etching, metal contacts were deposited to form electrical contacts of desired pattern. For ML-graphene devices, Ti/Au (5nm/50nm) contacts were deposited by e-beam evaporation (Kurt J. Lesker, Labline, base pressure $<1\times10^{-7}$ Torr) at a rate of 1/1 Å/s. For exfoliated MoS_2 devices, Bi/Au (10nm/40nm) contacts were deposited by e-beam evaporation (AJA, Orion ATC, base pressure $<9\times10^{-10}$ Torr) at a rate of 0.5/1 Å/s. For CVD-grown MoS_2 devices, Bi/Au (20nm/40nm) contacts was deposited by thermal evaporation at a rate of 0.1/1 Å/s at national Taiwan normal university.

The 15nm-thick nickel protective disk for silicon oxide nanopillar etching was deposited by e-beam evaporation (CHA, Mk40, base pressure $<5\times10^{-7}$ Torr and AJA, Orion ATC, base pressure $<9\times10^{-10}$ Torr) at a rate of 1 Å/s.

After metal deposition, the chip was lift-off in an acetone environment followed by IPA rinse.

2.7 Electrical transport measurement

The fabricated chip was then cut in to 7 ×7mm or smaller sizes using a diamond-tip pen and pasted to the center of a customized PC board using silver paint, with the PC board soldered to puck assembly (Quantum design, 8084-100, Appendix A), as shown in Figure 2.11. For devices used in photocurrent spectroscopy measurements, the specific device needs to be centered relative to the puck to one's best ability. After curing the silver paint for 2 hours at 93.3 ºC (with ~10 minutes of temperature ramping up from room temperature at rate of 450 ºC/hour), devices were bounded to the PC board with aluminum wire using wedge-wedge technique (Westbond, 7476D-79). The electrical connection was then tested over a PPMS user bridge (Quantum design) using Keithley 2450 source-measuring units (SMU) as shown in Figure 2.11(b), where electrical connections to the SMU were made via the LEMO connector on the side (not shown). Alternatively, when quick screening of devices was desired, a customized probe station may be used with Keithley 2450 SMUs with proper ESD-safe accessories, as shown in Figure 2.11(c).

Figure 2.11 Device wire bonding and electrical connection testing for transport measurements. (a) Optical image of device contact pads bonded by aluminum wires. (b)

PPMS puck assembly tested over a user bridge. (c) Device screening using a customized table-top probe station.

The cryogenic electrical transport measurement was performed in a Physical Property Measurement System (Quantum Design, PPMS), a shared facility in the Institute for Quantum Information and Matter (IQIM) at Caltech. The system provides temperatures from 1.8 K to 400 K and magnetic fields up to ±14 Tesla.

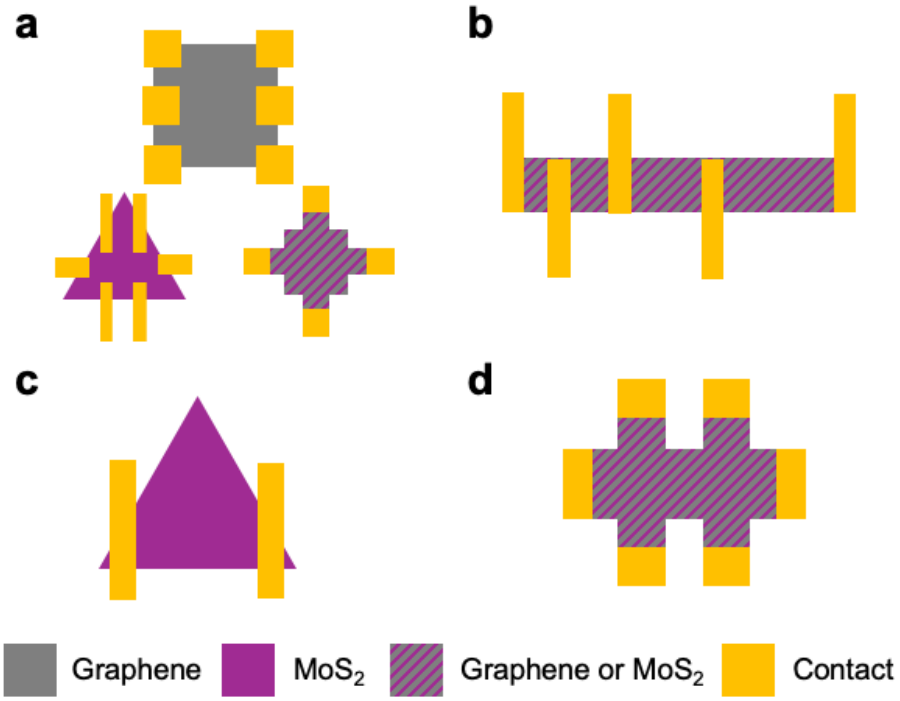

Figure 2.12 Illustration of the top view of different device geometries studied in this thesis, where the backgate contacts are not shown. (a) Van der Pauw (vdP) geometry. (b) Transmission line method (TLM) geometry. (c) Two-probe single crystalline field effect transistor geometry. (d) Hall bar geometry.

In this thesis, cryogenic electrical transport measurement of ML-graphene and ML-MoS_2 were studied in various device geometries, whose top views are illustrated in Figure 2.12 and exemplified in Figures 2.12 and 2.13. For ML-graphene devices, traditional two-probe and four-probe resistance measurements were performed with both DC and lock-in techniques in the quasi-DC limit. For example, DC four-probe measurements were performed to study gate-dependent and temperature-dependent resistance of ML-graphene using Keithley 2450 source-measuring unit (SMU). Four-probe AC measurements were performed to study the quantum Hall effect of ML-graphene using lock-in techniques in quasi-DC limit at 13 Hz (Stanford Research System, SRS 830, SRS 850). For MoS_2 devices, DC four-probe measurements were performed to study the gate-dependent and temperature-dependent resistance of ML-MoS_2 using Keithley 2450 SMUs. The photocurrent responses of MoS_2 field effect transistors were measured by using lock-in technique (Stanford Research System, SRS 830, SRS 850) with proper preamps (Stanford Research System, SRS560, SRS 551) under a DC bias voltage and a back-gate voltage applied by Keithley 2450 SMUs. A Detailed electrical circuits for these studies will be presented in later chapters.

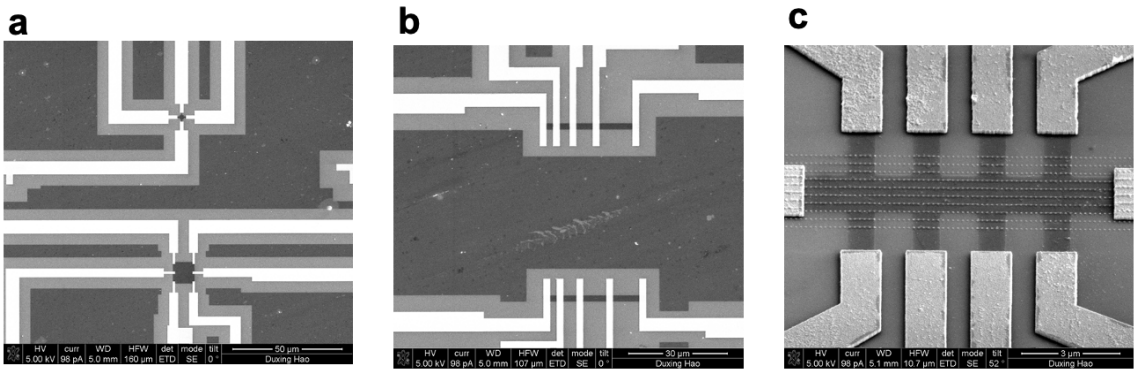

Figure 2.13 SEM images of typical ML-graphene devices in various geometries. (a) Four-probe (top) and six-probe (bottom) Van der Pauw geometry. (b) Transmission line method (TLM) geometry. (c) Hall bar geometry. In the false-color SEM images, the white area is the

Ti/Au contact, the dark grey area is ML-graphene, and the light grey area is the SiO_2/Si substrate.

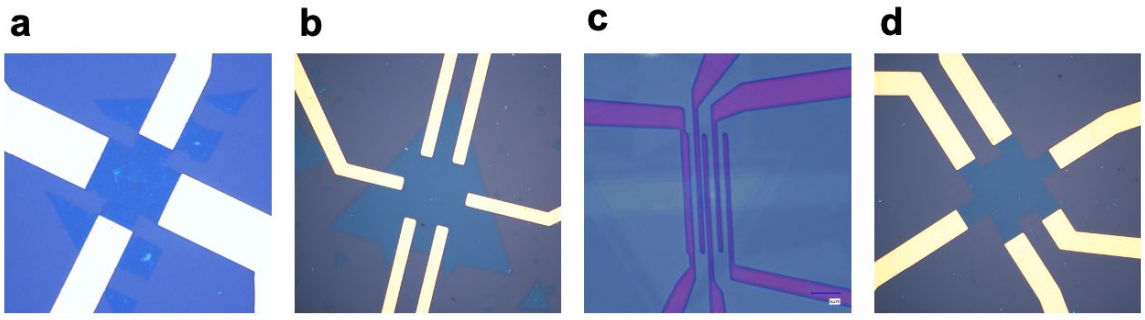

Figure 2.14 Optical micrograph (OM) of typical MoS_2 devices in various geometries. (a) Typical four-probe van der Pauw geometry. (b) Typical six-probe van der Paw geometry. (c) Transmission line method (TLM) geometry. (d) Hall bar geometry.

This chapter is temporarily embargoed.

Chapter 4

MAGNETIC FIELD-INDUCED POLAR ORDER IN MONOLAYER MOLYBDENUM DISULFIDE TRANSISTORS

4.1 Introduction

Polar order and its associated hysteretic behavior have played critically important roles in modern electronics applications. Ferroelectric materials, which feature a polar point group and polarization hysteresis upon switching external electric field, are crucial for high-density data storage, microwave devices, pyroelectric sensors, and non-volatile memories.[178–184] With the rapidly increasing demand for data storage capabilities, there is strong desire to reduce the dimensions of ferroelectric devices by exploring new materials, including 2D semiconductors such as 2H-TMDs. However, in the case of monolayer (ML) 2H-TMDs, the D_{3h} point group (space group P6m2) preserves the centrosymmetry and is therefore incompatible with ferroelectricity. If mirror symmetry about the horizontal plane of transition metal layer can be broken, such as in the case of ML-MoS_2 with a distorted-1T structure (C_{3V}, P3m1) where a slight vertical displacement of intralayer sulfur atoms results in broken mirror symmetry and a net electric polarization along the out-of-plane direction, then the lattice space group may reduce into a ferroelectric subgroup[185] and thus the emergence of ferroelectricity.[186–188] In this context, it is interesting to note that the shear-transformed bilayer 3R-MoS_2 system with broken mirror symmetry between the two MoS_2 monolayers reduces the symmetry group to C_{3v} (R3m), where ferroelectric response has been discovered recently.[189] Similarly, ferroelectricity has been reported in van der Waals (vdW) interfaces between two marginally twisted ML-vdW materials that lack polar point groups in their parent lattices, such as boron nitride (BN) and transition metal dichalcogenides (TMDs).[190–192]

In this chapter, we report giant ferroelectric-like hysteresis induced by out-of-plane magnetic field (B) in field-effect transistors (FETs) based on ML-MoS_2 single crystals on SiO_2/Si substrates at temperatures (T) below ~20 K. The counterclockwise hysteresis of the source-drain current (I_{DS}) as a function of the back-gate voltage (V_{GS}) can be enhanced by increasing the maximum V_{GS} value, increasing $|B|$, and lowering T. These robust findings from five distinct ML-MoS_2 FETs at low temperatures and under finite magnetic fields differ drastically from previous reports of high-temperature and zero-B hysteretic behavior in ML-MoS_2 FETs, the latter were attributed to mechanisms such as thermally-activated trapped states[193–195] absorbates,[196,197] and ordinary gate voltage-induced stress effects,[198] where clockwise hysteresis loops were observed near room temperatures without magnetic field dependences. We further present experimental evidence for magnetic field-induced lattice expansion in ML-MoS_2, which is associated with real-space structural transformation from lifting the valley degeneracy by magnetic field through spin-valley lock-in in ML-MoS_2. Based on these observations, we attribute the appearance of ferroelectric-like polar effects to asymmetric lattice expansion of ML-MoS_2 on rigid SiO_2/Si substrates, and we further corroborate this conjecture by demonstrating absence of polar effects in FETs consisting of ML-MoS_2 on substrates buffered with multilayers of hexagonal boron nitride (h-BN) with a thermal expansion coefficient (TEC) comparable to that of MoS_2 to prevent the occurrence of asymmetric lattice expansion.

4.2 Structural characterization of MoS_2-FETs

The MoS_2-FETs studied in this work were based on high quality 1H-MoS_2 single crystals (*a.k.a.* ML-MoS_2 with the 2H-phase) grown by chemical vapor deposition (CVD).[100–102] The ML-MoS_2 single crystals exhibited high degrees of homogeneity and were free from magnetic impurities, as verified by their optical and x-ray photoelectron spectroscopic characterizations exemplified Figures 4.1-4.3.

Figure 4.1(a) presents an optical microscope image of one of our ML-MoS_2 FETs. The ML-MoS_2 sample in the fabricated device exhibited high degrees of homogeneity according to optical spectroscopic characterizations, including a point spectrum and a spatial map of the photoluminescence (PL) under an excitation wavelength of 532 nm as demonstrated in Figures 4.1(b) and 4.1(c), respectively, showing a uniform PL optical band gap of∼1.81 eV. The representative single point spectrum and spatial maps of Raman spectra (Figures 4.1(d-g)) indicated a typical Raman peak separation between E_{2g} (∼ 387 cm^{-1}) and A_{1g} (∼ 404 cm^{-1}) of ∼17 cm^{-1} for ML-MoS_2.

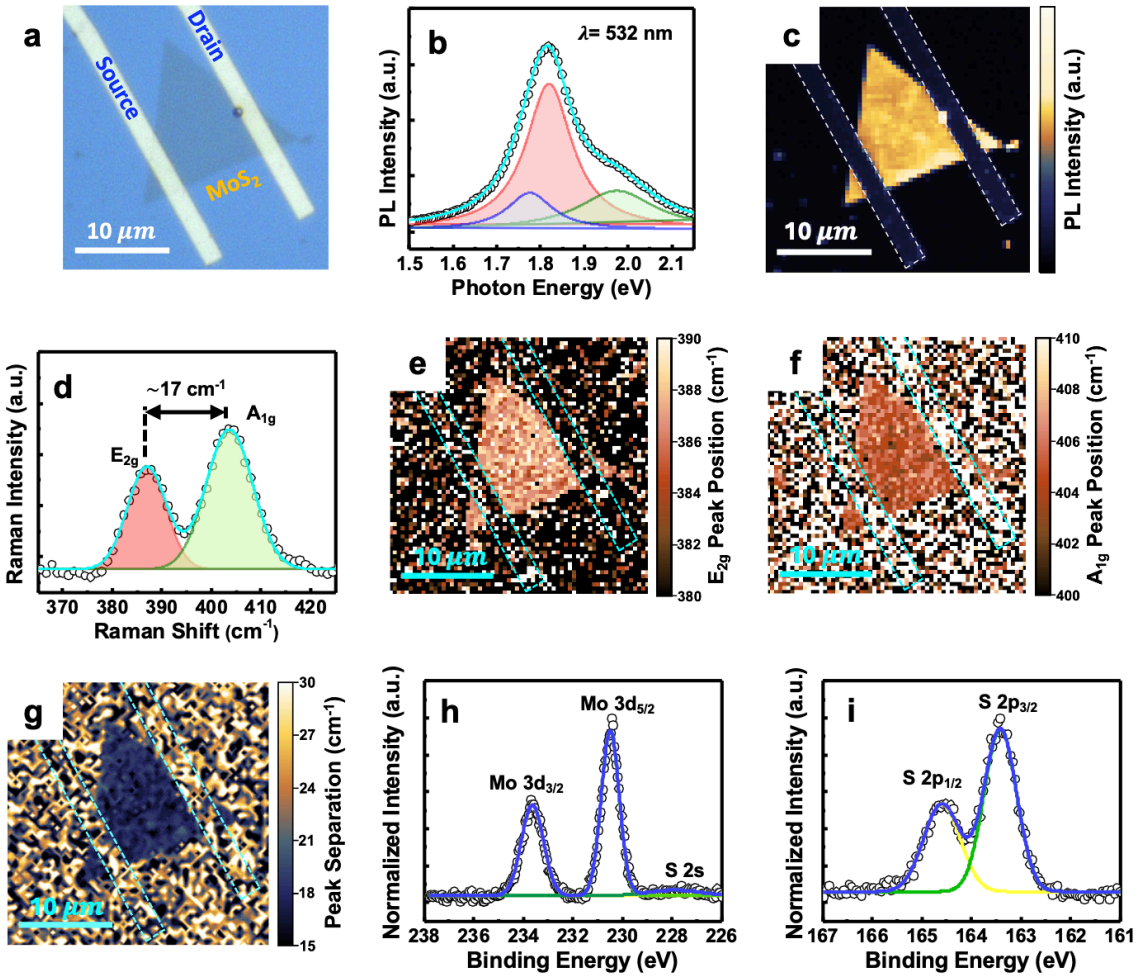

Figure 4.1 Spectroscopic characterizations of the monolayer MoS_2 field-effect transistor (FET). (a) Optical microscope image of a monolayer MoS_2 device #4. (b) Typical photoluminescence (PL) point spectrum and (c) spatial mapping presenting an optical bandgap of ~1.81 eV. (d) Typical Raman point spectrum and showing the peak position of E_{2g} at 387 cm^{-1}, A_{1g} at 404 cm^{-1}, and a peak separation of ~17 cm^{-1}. (e) Spatial mapping of E_{2g} peak position. (f) Spatial mapping of A_{1g} position. g) Spatial mapping of E_{2g} and A_{1g} peak separation. (h-i) X-ray photoelectron spectroscopy (XPS) spectra revealing the binding energy of Mo 3d and S 2p, respectively. All spectroscopic measurements were performed at T = 300 K.

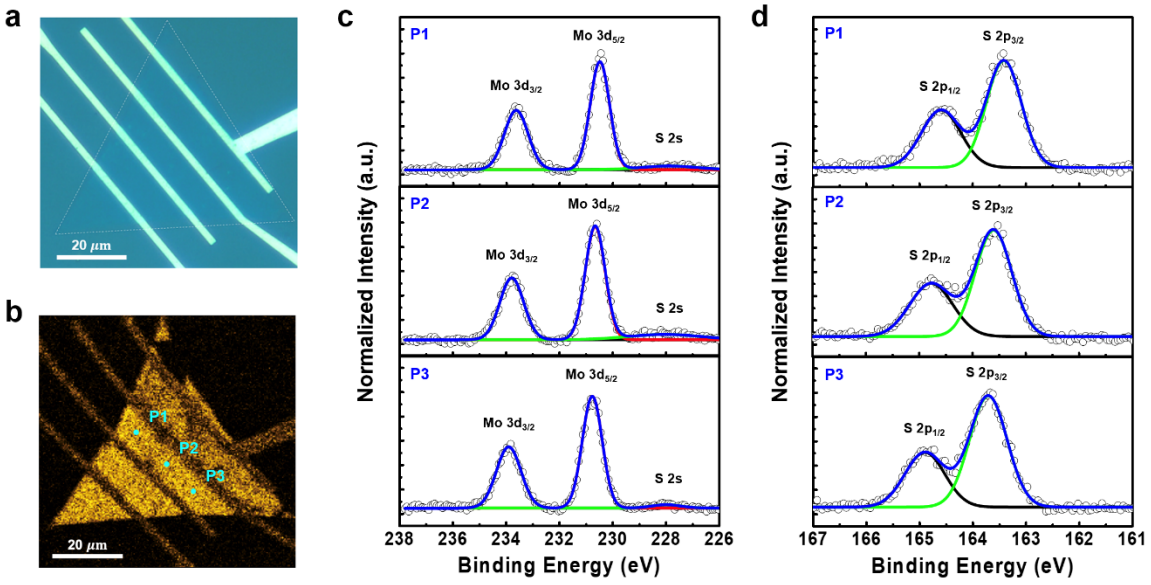

Figure 4.2 Spatially resolved XPS measurements. (a) Optical micrograph image of the monolayer MoS_2 FET. (b) The XPS Mo-3d map reveals the uniform quality of the monolayer MoS_2. (c-d) The XPS spectra of the Mo 3d and S 2p, respectively, for a measured device. The locations where the point spectra were taken are indicated as light-blue dots (P1 to P3) in the mapping image of (b).

The X-ray photoelectron spectroscopy (XPS) experiments, as exemplified in Figures 4.1(h-i) and Figure 4.2, were carried out using the scanning photoelectron microscopy (SPEM) endstation at beamline 09A1 of the National Synchrotron Radiation Research Center's Taiwan Light Source at ultra-high vacuum (UHV) conditions of ~ 10^{-9} Torr near 300 K, with a pre-annealing process of sample for 20 hours at ~ 400 K. Monochromatic soft X-rays (400 eV photon energy) were focused down to a ~200 nm spot using Fresnel-zone-plate-based focusing optics and photoelectrons are collected. These spectral and mapping characteristics of our samples after the polymer-based device fabrication process were still consistent with the values obtained from direct measurements on high quality single crystalline monolayer

MoS_2 samples reported previously.[199,200] The spatial mapping in Figure 4.2 revealed no signals of magnetic impurities across the device, which corroborated with the highly uniform crystalline structure seen in scanning tunneling electron microscopy (STEM) image (Figure 4.3) on a sample grown in the same batch.[199,200]

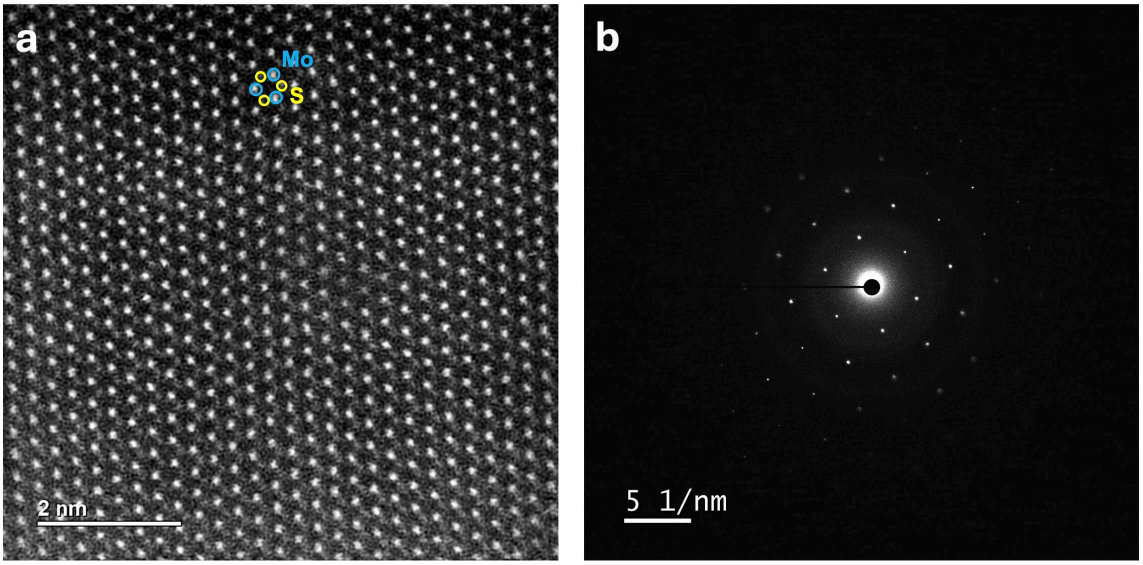

Figure 4.3 Atomically resolved STEM measurements. (a) Atomically resolved STEM image displaying an 8 nm × 8 nm area of ML-MoS_2. (b) Selected area electron diffraction (SAED) image further confirms the high-quality crystalline structure of the ML-MoS_2.

4.3 Near-ohmic MoS_2-FETs with ultralow contact barrier at cryogenic temperature

Most FET devices studied in this work exhibited an ohmic-like behavior in the I_{DS}-*vs.*-V_{DS} curves from 300 K to 1.8 K under different V_{GS} values, as exemplified in Figures 4.4(a) and 4.4(b). The insets of Figure 4.4(a) and Figure 4.4(b) revealed an on/off ratio $>10^5$, while a shift of threshold voltage from 0 V (300 K) to 15 V (1.8 K) was apparent due to fewer thermally excited carriers at low temperature. This ohmic-like performance at 4K is achieved

using Bi/Au contacts, where previous study shown that ultralow contact barrier was achieved.[201,202] Our study followed the same methodology and showed that our devices had an ohmic-like behavior at 300 K and a near-ohmic behavior at 1.8 K, as exemplified in Figures 4.4 and 4.5.

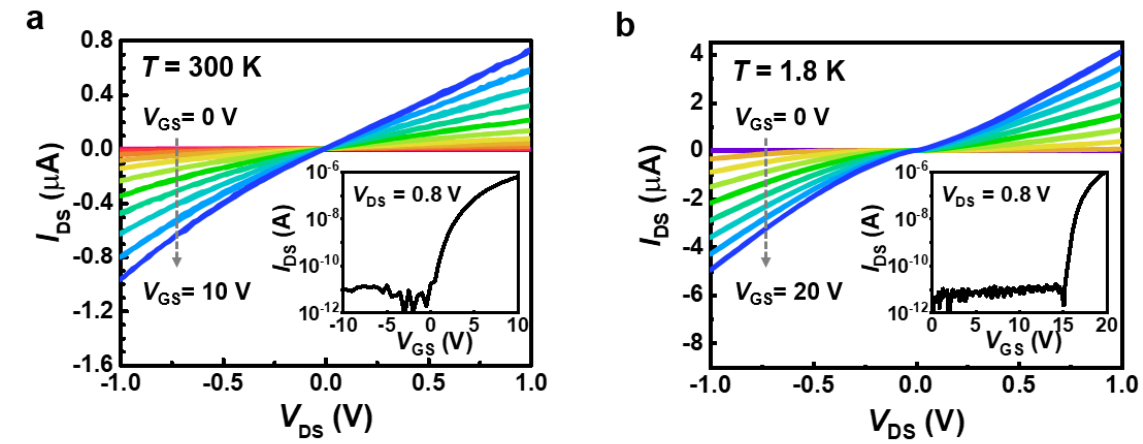

Figure 4.4 MoS_2 FET device characterization at 300 K and 1.8 K. I_{DS}-*vs.*-V_{DS} curves under various V_{GS} measured at (a) T = 300 K and (b) 1.8 K, respectively on device #1. Insets present logarithmic I_{DS}-*vs.*-V_{GS} curves.

Under the condition that $qV_{DS} \gg k_B T$, the thermally injected current from Bi/Au contact to our MoS_2 single crystal may be approximated by the following equation:

$$I_{DS} \approx A_{2D}^{*} T^{1.5} \exp\left(-\frac{E_A}{k_B T}\right),$$

where $A_{2D}^{*} = q(8\pi k_B^3 m^*/h^2)$ is the Richardson constant for a 2D system, $E_A = q\phi_B$ is the Schottky barrier height under the flat-band condition (Figure 4.5(a)). The inset of Figure 4.5a showed a typical device (Device #5) that exhibited a typical Schottky barrier-like behavior, with negative linear slopes in the Arrhenius plot. In contrast, ohmic-like contacts were found

in Devices #1 - #3 with extracted Schottky barrier of −20 meV, which exhibited positive slopes that asymptotically approached zero slope in the Arrhenius plot (Figure 4.5(b)) as a signature of negligible contact barrier, similar to the report by Shen *et. al.*.[202] As a result, the device showed ohmic-like $|I_{DS}|$-*vs.*-V_{DS} transfer curves at 300 K (Figure 4.4(a)) and nearly-ohmic transfer curves at 1.8 K (Figure 4.4(b)). Figures 4.5(c,d) showed corresponding I_{DS}-*vs.*-V_{GS} curve measured at 300 K and 1.8 K. The mobility for these devices was typically ~10 $cm^2V^{-1}S^{-1}$ or better[203] and was comparable to previously reported mobility range between 0.1-10 $cm^2V^{-1}S^{-1}$ over exfoliated ML-MoS_2 devices on typical SiO_2/Si substrates,[204–206] which appears to be substrate Coulomb impurity-limited instead of sample quality-limited or contact-limited. [207,208]

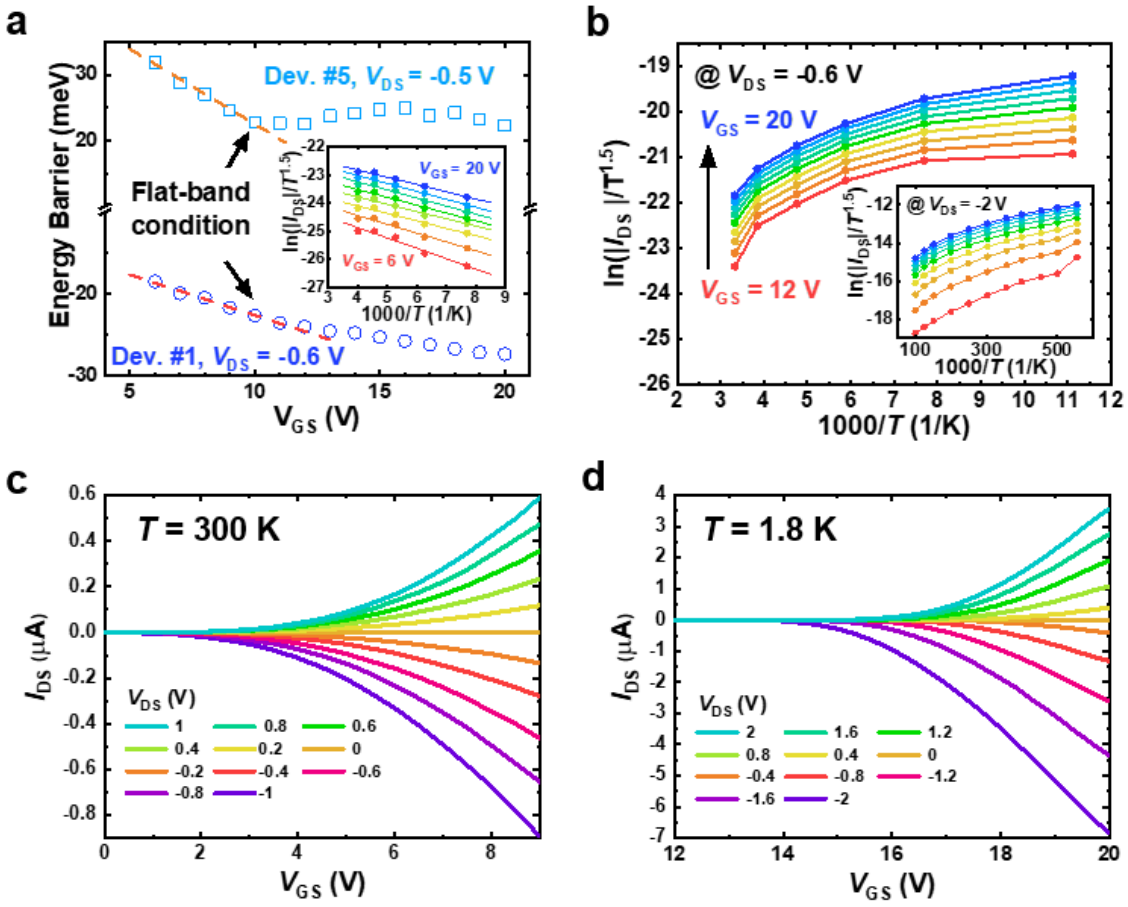

Figure 4.5 Low contact barrier ML-MoS_2 FETs down to 1.8 K. (a) Main panel: Contact barrier extracted from Device #1 and Device #5 at 1.8 K. The arrows point to the dashed linear fits consistent with the flat-band conditions for ohmic contacts.[201,202] While both devices exhibited a negligible contact barrier, the high temperature dependence of Device #5 exhibited a signature linear behavior in Arrhenius plot (inset), where electron injection originated from thermionic emission across a Schottky barrier. The arrows point to the dashed linear fits consistent with the flat-band conditions for ohmic contacts.[201,202] Here V_{GS} is colored from 6 V (red) to 20 V (blue) with an interval of 2V. (b) Arrhenius plots of Device #1 measured between 100 K - 300 K with V_{DS} = –0.6 V (main panel) and 1.8 K - 10 K (inset) with V_{DS} = –2 V. Here V_{GS} is colored from 12 V (red) to 20 V (blue) with an interval of 1 V.

The almost saturated slope indicates a vanishing contact barrier. Similar behavior is observed on Device #2 and Device #3. (c-d) I_{DS}-*vs.*-V_{GS} characteristics of Device #1 under different V_{DS} values at (c) 300 K and (d) 1.8 K, respectively. For all devices except Device #5, the contact resistance exhibited nearly ohmic behavior at all temperatures.

4.4 Emerging electric hysteresis in MoS_2-FETs under magnetic field

The schematic of a transistor and its electrical measurement circuit is shown in the inset of Figure 4.6(a), where the source-drain voltage (V_{DS}) was applied between a pair of bismuth (Bi)/gold (Au) contacts, and the gate voltage (V_{GS}) was applied between the source contact and a heavily *p*-doped Si substrate with a 30 nm-thick SiO_2 insulating layer. Nearly ohmic source-drain current (I_{DS}) versus gate voltage (V_{GS}) transfer curves were observed down to 1.8 K (Figure 4.6(a)) due to ultralow-Schottky barriers associated with the Bi/Au contacts[202] (Figure 4.4, Figure 4.5). The mobility of these FET devices was typically around ~10 $cm^2V^{-1}S^{-1}$ or better at 300 K, as detailed previously.[203] These values was comparable to the reported mobility values ranging 0.1-10 $cm^2V^{-1}S^{-1}$ for typical FET devices made of exfoliated ML-MoS_2 on SiO_2-supported substrates,[204–206] which appears to be limited by substrate charged impurities instead of sample quality-limited or contact-limited.[207,208]

Upon application of an out-of-plane magnetic field (B), counterclockwise $|I_{DS}|$-*vs.*-V_{GS} hysteretic loops emerged from measurements of the FET devices at 1.8 K, as exemplified in Figure 4.6(b) for $B = 9$ T, where the $|I_{DS}|$-*vs.*-V_{GS} transfer curves were measured with different V_{DS} values fixed at −1.0 V, −0.8 V, and −0.6 V. On the other hand, no loop was present for $B = 0$ (Figure 4.6(b) inset). This emergence of counterclockwise hysteretic behavior at low temperature and finite magnetic field is a response of ferroelectric-like polar order modulation caused by magnetic-field induced asymmetric rippling effect, which is

fundamentally different from previously known hysteresis-inducing mechanisms as elaborated in Appendix C.

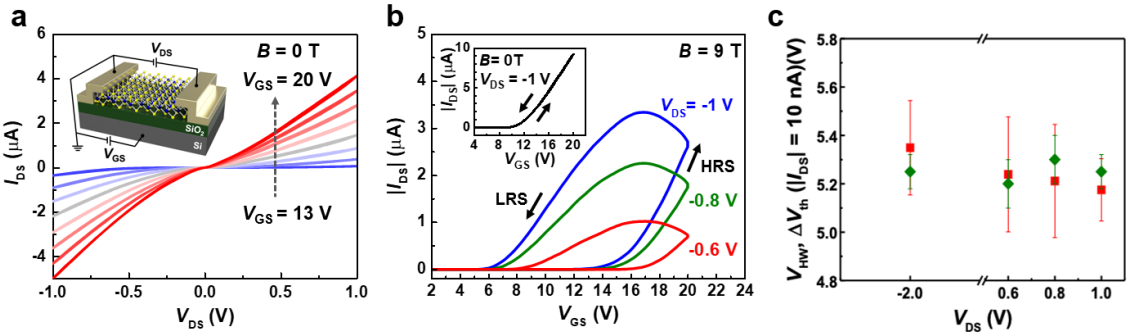

Figure 4.6 Magnetic-field induced giant hysteresis responses in ML-MoS_2 field-effect transistor (FET) at T = 1.8 K. (a) I_{DS}-*vs.*-V_{DS} transfer curve measured at a gate voltage (V_{GS}) from 13 V to 20 V with an increment of 1 V, showing largely ohmic characteristics. (b) Main panel: $|I_{DS}|$-*vs.*-V_{GS} hysteresis curves measured under a magnetic field of 9 T with V_{DS} fixed at –1 V, –0.8 V and –0.6 V, respectively. Inset: $|I_{DS}|$-*vs.*-V_{GS} curve taken at B = 0, showing absence of hysteresis. Black arrows in the main panel indicate the V_{GS} sweeping direction for the corresponding HRS/LRS states under different V_{DS} values, which reveal the counterclockwise hysteresis loops for all V_{DS} values at B = 9 T. (c) Extracted V_{HW} (green) and ΔV_{th} ($|I_{DS}|$ = 10 nA) (red) from V_{DS} fixed at 1 V, 0.8 V, 0.6 V, and –2V, respectively.

To quantify the size of the observed hysteresis loop, we first extract the threshold voltages $V_{th,\,H}$ and $V_{th,\,L}$ by first fitting the linear region of the high-resistance state (HRS, forward branch) and low-resistance state (LRS, backward branch) of the $|I_{DS}|$-*vs.*-V_{GS} transfer curves respectively, then finding their corresponding x-axis intercepts. The hysteresis window (V_{HW}) was then given by $V_{HW} \equiv V_{th,\,H} - V_{th,\,L}$ and was largely independent of V_{DS}, as shown in Figure 4.6(c) green diamonds. Another practical quantity to characterize the hysteresis loop size is the hysteresis width (ΔV_{th}),[195] which is defined as the gate voltage difference

between the intercepts of a small threshold current (*i.e.*, 10 nA) with the HRS and LRS $|I_{DS}|$-*vs.*-V_{GS} curves so that ΔV_{th} ($|I_{DS}|$ = 10 nA) ≡ $V'_{th,\,H}$ ($|I_{DS}|$ = 10 nA) – $V'_{th,\,L}$ ($|I_{DS}|$ = 10 nA). Another practical quantity to characterize the hysteresis loop size is the hysteresis width (ΔV_{th}),[195] which is defined as the gate voltage difference between the intercepts of a small threshold current (*i.e.*, 10 nA) with the HRS and LRS $|I_{DS}|$-*vs.*-V_{GS} curves so that ΔV_{th} ($|I_{DS}|$ = 10 nA) ≡ $V'_{th,\,H}$ ($|I_{DS}|$ = 10 nA) – $V'_{th,\,L}$ ($|I_{DS}|$ = 10 nA). In our study, we found that both V_{HW} and ΔV_{th} ($|I_{DS}|$ = 10 nA) gave similar results while the former was independent of the choice of the threshold quantity (threshold current), as exemplified in Figure 4.6(c). Therefore, we chose V_{HW} to represent to the size of the hysteresis loop unless otherwise specified. We further remark that the Zeeman splitting under external magnetic fields would reduce the bandgap at the K or K′ valley via lowering the conduction band minimum and lifting the valence band maximum. However, this effect was on the order of $10^{-3} \sim 10^{-4}$ eV for $|B| \sim 10$ T,[209,210] which corresponded to approximately $10^{-2} \sim 10^{-3}$ V changes in the back gate voltage.

As shown in Figure 4.6(b), when sweeping up V_{GS}, the system was initially in the HRS,[211] showing $|I_{DS}| > 0$ for $V_{GS} > V_{th,H}$. In contrast, when V_{GS} was reduced from a finite $|I_{DS}|$ state, the lattice returned from a highly polarized LRS[178,211] so that $|I_{DS}|$ remained finite until V_{GS} reached $V_{th,L}$ ($< V_{th,H}$), where $V_{th,L}$ represented the threshold voltage for $|I_{DS}| > 0$ in the returned branch. Within the applicable range of V_{GS} up to 36 V in all 5 devices (Dev. #1 - #5), none of the hysteresis loops became fully closed within our experimental parameters due to limited electrical doping capability and the necessity of keeping the leakage current small. We found that $|I_{DS}|$ continued to increase upon reversing V_{GS} from 20 V to 16 V (Figure 4.6(b)), which may be due to the transient response of charging as a result of polar order modulation. Additionally, while the $|I_{DS}|$-*vs.*-V_{GS} curves measured with different V_{DS} values yielded different loop shapes, the extracted hysteresis window V_{HW} (≡ $V_{th,H} - V_{th,L}$) remained the same (Figure 4.6(c)).

4.5 Modulation of the magnetic field-induced electric hysteresis

The magnetic field-induced hysteresis may be tuned by magnitude of the out-of-plane magnetic field, the out-of-plane electric field, and temperature. Firstly, the out-of-plane magnetic field consistently manifest the following the following key findings observed across five different devices (Figures 4.7-4.9): (1) under a constant out-of-plane B, the $|I_{DS}|$ value obtained at a given V_{GS} was smaller for a larger $|B|$ due to a positive magnetoresistance; (2) the size of the hysteresis loop V_{HW} increased with $|B|$, suggesting a stronger polar order under a higher magnetic field (Figure 4.7); (3) the hysteresis loop was independent of the sign of B from –9 T to 9 T (Figure 4.7); (4) no discernible magneto-hysteresis of $|I_{DS}|$-*vs.*-V_{GS} curves was observed during the two consecutive magnetic field sweeps from –9 T to 9 T then from 9 T back to –9 T (Figure 4.8), indicating absence of out-of-plane magnetism; and (5) the hysteresis window V_{HW} increased approximately linearly with $|B|$ for $|B| < 3$ T, and then saturated for large $|B|$ (Figure 4.7(b) and Figure 4.9).

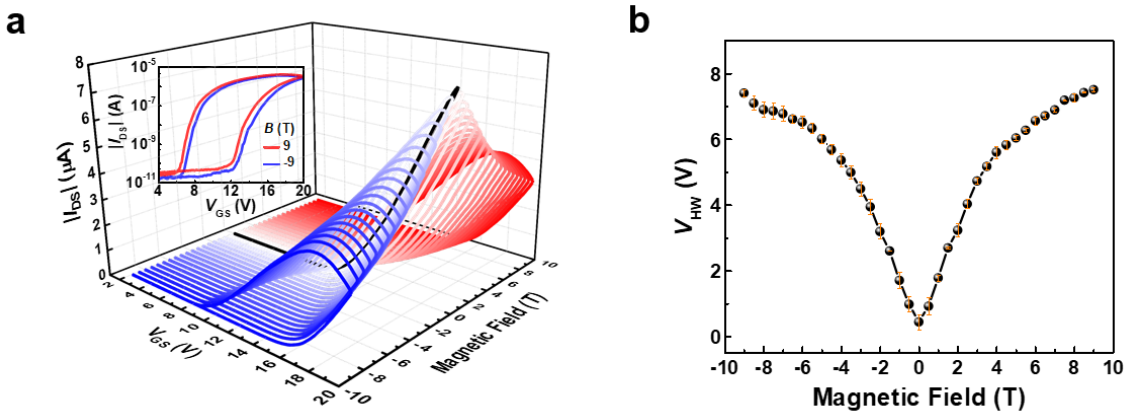

Figure 4.7 Modulated hysteresis responses in ML-MoS_2 field-effect transistor (FET) at T = 1.8 K by out-of-plane magnetic field. (a) $|I_{DS}|$-*vs.*-V_{GS} hysteresis under magnetic field from 9 T to –9 T with V_{DS} = –1 V, showing characteristics independent of the sign of magnetic field within experimental errors, as further demonstrated in the semi-log inset for comparison of

the hysteresis loops taken at B = 9 T (red) and – 9 T (blue). (b) Hysteresis window V_{HW} as a function of out-of-plane magnetic field.

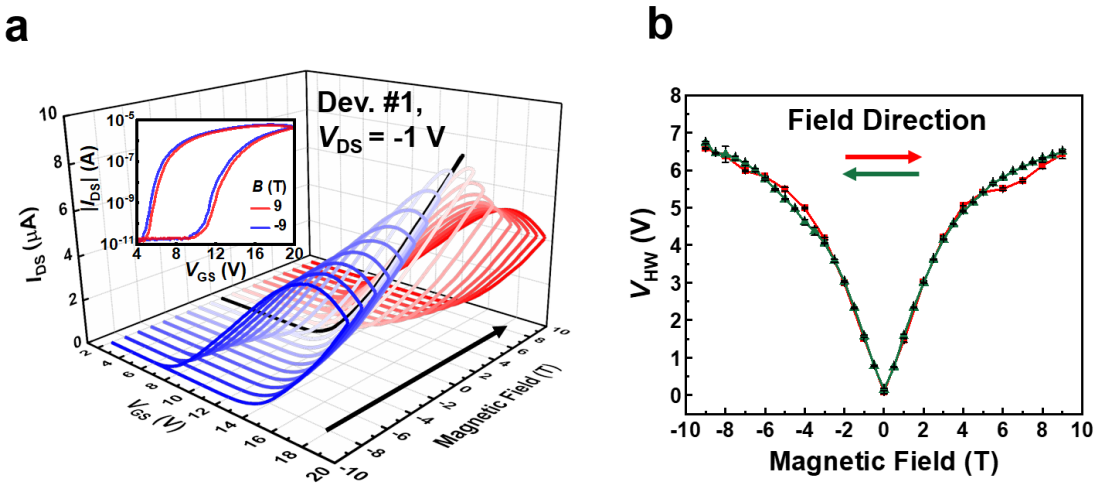

Figure 4.8 Magnetic field sign-symmetric hysteretic behavior of the monolayer MoS_2 FET devices. (a) $|I_{DS}|$-*vs.*-V_{GS} hysteresis under magnetic field from –9 T to 9 T (sweep direction indicated by the black arrow) with V_{DS} = –1 V measured after Figure 4.7(a). A magnetic field sign-symmetry under B = ±9 T is presented within experimental error as shown in the semi-log inset. (b) Magnetic-field controlled V_{HW} and extracted from (a) and Figure 4.7(a). Red and green arrows indicate the corresponding field ramping directions. These results strongly suggest the absence of any discernible out-of-plane magnetization.

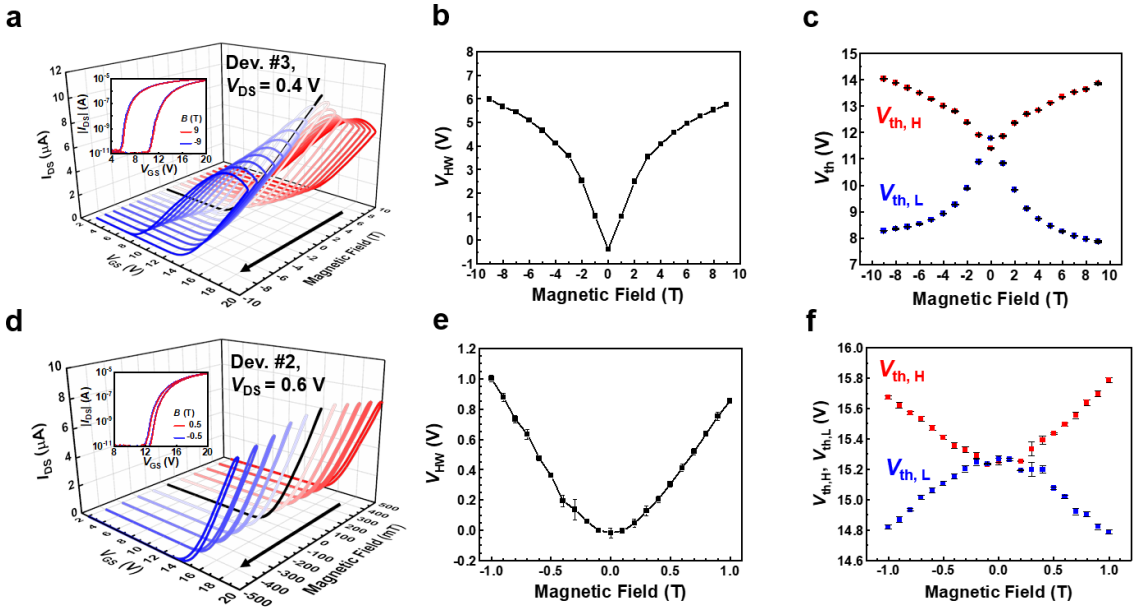

Figure 4.9 Consistent high and low-field hysteresis behavior measured on additional devices. (a) Main panel: $|I_{DS}|$-*vs.*-V_{GS} hysteresis under magnetic field from 9 T to -9 T (sweep direction indicated by the black arrow) with V_{DS} = 0.4 V measured on Device #3. A magnetic field sign-symmetry under $B = \pm 9$ T is presented within experimental errors as shown in the semi-log inset. (b) Magnetic field-controlled V_{HW} extracted from (a). (c) Threshold gate voltages $V_{th,\,H}$ and $V_{th,\,L}$ for Device #3 are shown as a function of the applied magnetic field from –9 T to 9 T. (d) Main panel: $|I_{DS}|$-*vs.*-V_{GS} hysteresis loops under low magnetic fields from B = –0.5 T to 0.5 T (sweep direction indicated by the black arrow) with $V_{DS} = 0.6\,V$ measured on Device #2 are shown for the sake of clarity. A magnetic field sign-symmetric low-field hysteresis behavior under $B = \pm 0.5$ T is presented in the semi-log inset. (e) Magnetic field controlled V_{HW} extracted from (d). (f) Threshold gate voltages $V_{th,\,H}$ and $V_{th,\,L}$ for Device #2 are shown as a function of the applied magnetic field from –1.0 T to 1.0 T.

Secondly, we found the applied electric field, particularly in the out-of-plane direction, may provide hysteresis modulation. Figure 4.10(a) shows the linear and semi-log scale (inset) $|I_{DS}|$-*vs.*-V_{GS} curves of a FET device measured at 10 K and $B = 9$ T and for V_{GS} swept from 2 V to different maximum gate voltages ($V_{GS,\,max}$) then back. Interestingly, under a fixed magnetic field, a higher $V_{GS,\,max}$ led to increasing although eventually saturating V_{HW} (Figure 4.10(b)). Combining with the observation that V_{HW} was independent of on the in-plane voltage V_{DS} (Figure 4.6(c)), we may conclude that the field-induced polarization was mostly tunable via the out-of-plane electric field rather than in-plane electric field.

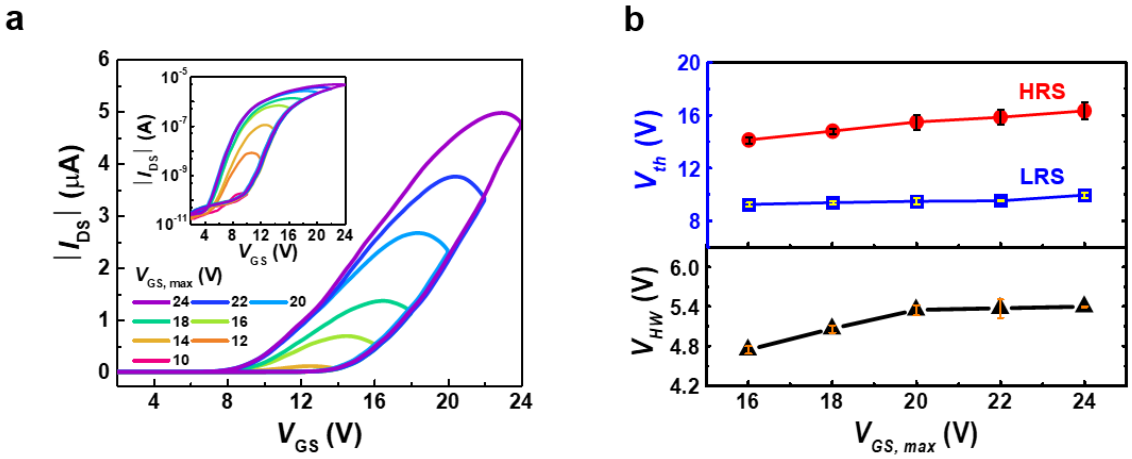

Figure 4.10 Gate voltage modulation of electric hysteresis. (a) Linear-scale (main panel) and semi-log-scale plot (inset) of $|I_{DS}|$-*vs.*-V_{GS} characteristics, showing different hysteresis loop sizes under different V_{GS} ranges. All measurements started at $V_{GS} = 2$ V and ended at different $V_{GS,\,max}$ values under the conditions of $T = 10$ K, $B = 9$ T and $V_{DS} = -0.6$ V. (b) Characteristics voltages ($V_{th,\,H}$, $V_{th,\,L}$, V_{HW}) of the hysteresis loops in **a** are shown as a function of $V_{GS,\,max}$.

Finally, temperature may also be used to modulate this hysteresis, as shown in the Figure 4.11. Upon increasing temperature from 1.8 K under a constant magnetic field of 12 T, the size of the hysteresis loop first shrank gradually with temperature, and then decreased precipitously above ~14 K, and finally vanished at the critical temperature (T_C) ~19.3 K

(Figure 4.11(a)) where V_{HW} vanished completely (Figure 4.11(a), inset). Above the T_C, a small magnetic field-independent clockwise hysteresis background emerged as exemplified in Figure 4.12, which was due to the gate voltage stress[198] and remnant oxide trapping close to the SiO_2-MoS_2 interface as previously reported.[193,194] We further investigated the temperature dependence of V_{HW} for the counterclockwise hysteresis loops under different constant magnetic fields (Figure 4.11(b)) and found that the critical temperature T_C where V_{HW} vanished increased with increasing $|B|$ (Figure 4.11(b), inset), whereas for a given temperature below T_C, V_{HW} always increased with $|B|$. Noting that the in-plane TA and LA phonon modes of ML-MoS_2 became frozen below 20 K[212] where the magnetic field induced lattice expansion emerged, the modulation of T_C by magnetic field was less disturbed by in-plane phonons so that larger degrees of lattice expansion induced by stronger magnetic field may survive a higher temperature, yielding the observation of a higher T_C. Overall, comparable T_C-*vs.*-B values within ±1 K variations among four different devices were found (Figure 4.11(c)), suggesting the robust presence of this hysteresis across devices

In summary, we found out-of-plane magnetic field, gate voltage and temperature may modulate the hysteresis, although the out-of-plane magnetic field and temperature were able to turn the hysteresis on/off while gate voltage only provides limited modulation capability.

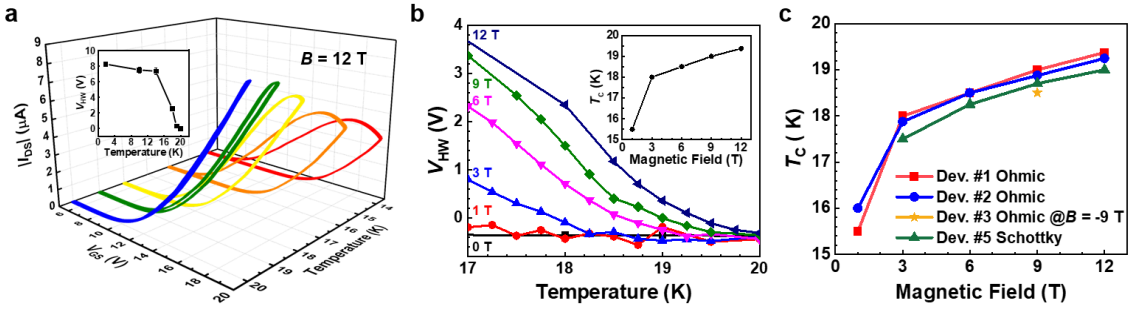

Figure 4.11 Temperature modulation of electric hysteresis. (a) Temperature dependence of $|I_{DS}|$-*vs.*-V_{GS} characteristics, showing a loop closing at T_C = 19.3 K under a constant magnetic field of 12 T. The inset shows the emergence of V_{HW} and P_0 below T_C. (b) Main panel:

Determination of the critical temperature (T_C) from the V_{HW}-T plots under different constant magnetic fields, where $T_C(B)$ is identified at the temperature where $V_{HW}(B, T) = 0$. The inset shows a higher magnetic field leads to a higher T_C. Measurements were taken with $V_{DS} = -1$ V. (c) Magnetic field-dependent T_C values for Devices #1, #2, #3, and #5. All T_C values were measured under positive magnetic fields except Device #3 where the T_C value was measured at $B = -9$ T.

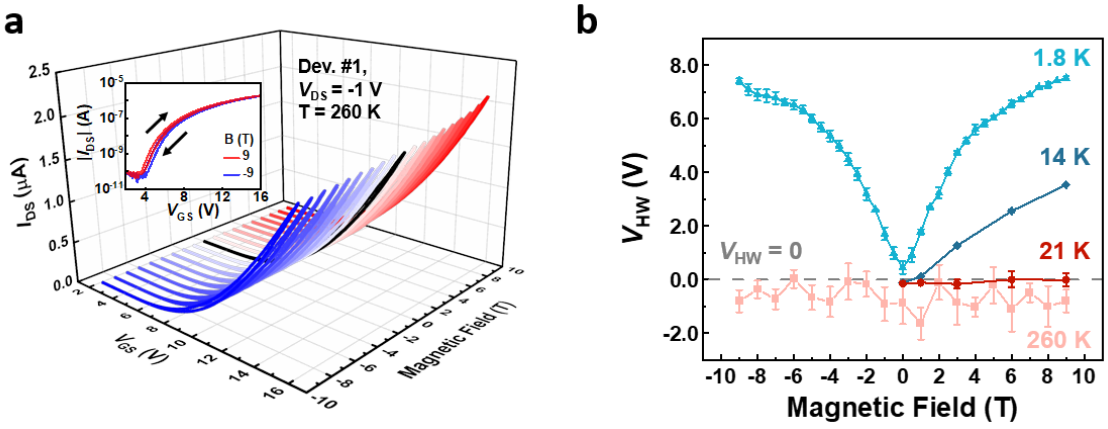

Figure 4.12 Magnetic field-independent clockwise hysteresis at 260 K. (a) $|I_{DS}|$-*vs.*-V_{GS} hysteresis under magnetic field from 9 T to –9 T with $V_{DS} = -1$ V measured at 260 K. As exemplified in the semi-log inset, clockwise hysteresis loop (indicated by black arrow) that was almost independent of magnetic field was observed under $B = 0$ and $B = -9$ T. (b) V_{HW}-*vs.*-B taken at 1.8 K, 14 K, 21 K, and 260 K. Grey dashed line shows the constant zero V_{HW}.

4.6 Raman-resolved magnetic field-induced MoS_2 lattice expansion

To elucidate the physical origin for magnetic field-induced hysteresis in these ML-MoS_2 FETs, we carried out cryo-temperature Raman spectroscopic studies of ML-MoS_2 on SiO_2/Si substrates, as shown in Figure 4.13(a) and Figure 4.13(b). Upon cooling the sample from 300 K at B = 0, both the A_{1g} and E_{2g} peaks were found blue-shifted due to a positive thermal expansion coefficient (TEC) down to ~20 K, below which the TEC became slightly negative as a result of frozen in-plane phonon modes[212–214] (Figure 4.13(c)).

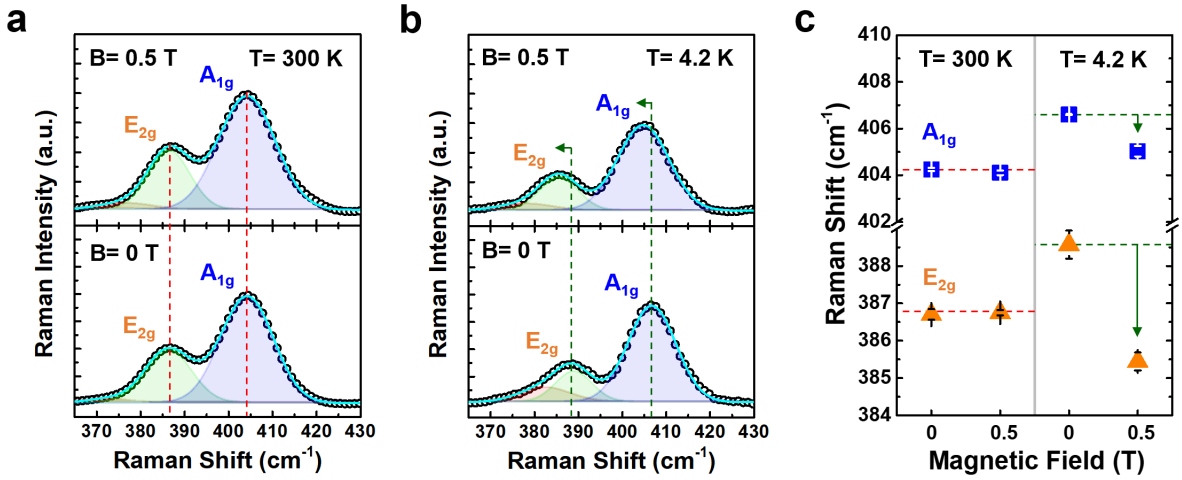

Figure 4.13 Raman characterizations of a ML-MoS_2 device under an out-of-plane magnetic field at 4.2 K. (a, b) Raman spectra taken under B = 0 (bottom) and an out-of-plane magnetic field B = 0.5 T (top) at (a) 300 K and (b) 4.2 K, respectively. (c) The Raman peak positions for A_{1g} (blue square) and E_{2g} (orange triangle) at 300 K and 4.2 K with and without magnetic field. The red (green) dashed lines indicate the peak positions of A_{1g} and E_{2g} at 300 K (4.2 K) under B = 0.

In particular, the peak positions of the A_{1g} and E_{2g} modes at 4.2 K were found to be at 406.6 cm^{-1} and 388.6 cm^{-1}, respectively, both higher than the A_{1g} (404.3 cm^{-1}) and E_{2g} (386.7 cm^{-1}) peak positions measured at 300 K. Upon the application of an out-of-plane magnetic

field of 0.5 T, however, significant field-induced redshifts were found for both the E_{2g} (-3.1 cm^{-1}) and A_{1g} (-1.5 cm^{-1}) modes at 4.2 K, whereas no discernible field-induced effect on the Raman modes was observed at 300 K, as shown in Figure 4.13(c). These findings suggest that under a magnetic field below $T_C(B)$, both the in-plane E_{2g} mode and the out-of-plane A_{1g} mode became softened, which implied a tensile strain on the lattice, similar to the Raman mode softening observed in the bubbled regions of ML-WS_2 encapsulated by h-BN.[215 215]

4.7 STM-resolved magnetic field-induced MoS_2 lattice expansion

Further evidence for magnetic field-induced lattice expansion was manifested by scanning tunneling microscopic (STM) studies of a ML-MoS_2 sample grown *in situ* on highly ordered pyrolytic graphite (HOPG).

The as-grown ML-MoS_2 sample was first outgassed *in situ* at a temperature of 800 K and a vacuum of 2×10^{-10} Torr for an hour. After being transferred to an STM chamber, the ML-MoS_2/HOPG sample was then measured at 4.5 K under various magnetic fields using an electrochemical-etched tungsten tip, whose quality was verified by test measurements on Au (111) surface states. Further STM calibration was done by scanning on pure HOPG areas of the sample at 4.5 K prior to the study of sample area covered by a ML-MoS_2. Due to the lattice constant mismatch as well as a small twist angle between HOPG and the as-grown ML-MoS_2, moiré superlattice patterns were observed in the STM topography.

These moiré patterns are very sensitive to the lattice mismatch between ML-MoS_2 and the underlying HOPG, hence served as an excellent tool to accurately determined the MoS_2 lattice expansion by studying the STM topography of the same sample area under various constant magnetic fields. Since the lattice constant of HOPG remains constant under

magnetic field,[216] the lattice match (δ) caused by magnetic field may be solely attributed to the changes in the ML-MoS_2 lattice constant so that $\delta = (a_G + a_M + \Delta a) / a_G$, where a_G = 0.246 nm and a_M = 0.318 nm are the lattice constant of HOPG and ML-MoS_2 under zero magnetic field, respectively, and Δa is the ML-MoS_2 lattice expansion under a finite magnetic field.[217] Given the twsist angle (φ) between HOPG and MoS_2, the expected moiré pattern periodicity (λ) becomes $\lambda = \frac{(1+\delta)a_G}{\sqrt{2(1+\delta)(1-\cos\varphi) + \delta^2}}$.

To extract lattice mismatch from the STM topography image, fast Fourier transformation (FFT) was performed over the obtained raw topographic image, and then the MoS_2 lattice constant, moiré periodicity and twist angle were derived from studying the FFT pattern. Inverse FFT was then performed on the filtered FFT image to obtain the filtered topography that highlighted the moiré pattern evolution under magnetic field. This data analysis was exemplified in Figures 4.14(a-d).

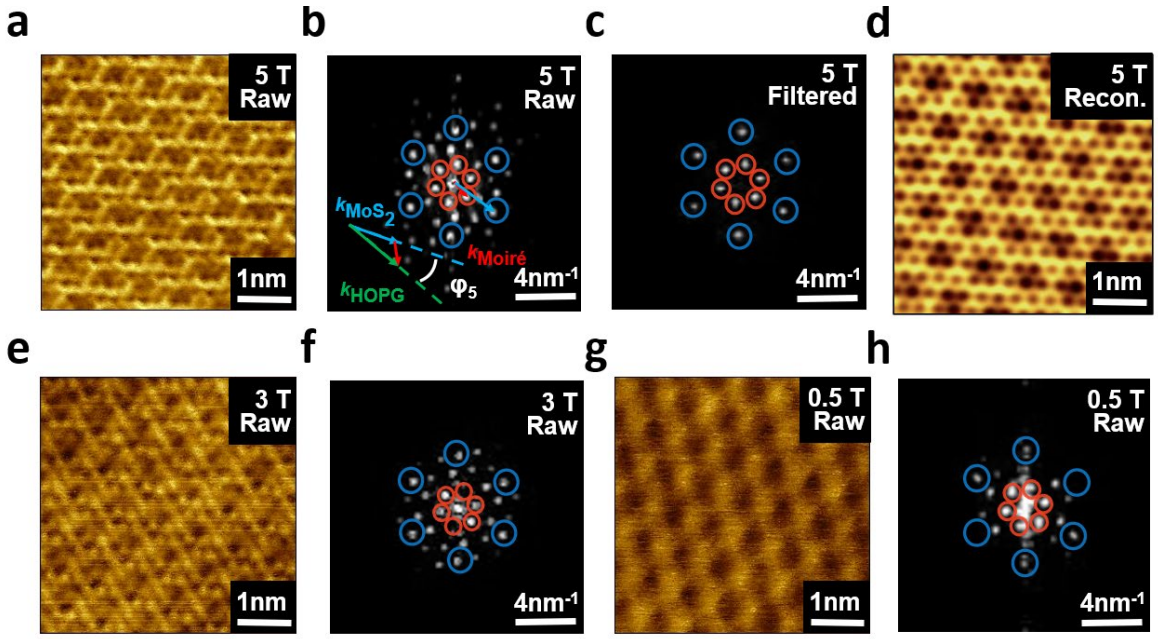

Figure 4.14 Image processing and raw data of STM topography. (a) Raw data of ML-MoS_2/HOPG moiré superlattice topography under a magnetic field of 5T. (b) FFT image of the topography shown in (a), where blue and red circles highlighted the MoS_2 reciprocal lattice vectors and the moiré reciprocal superlattice vectors, respectively. Red, blue, and green arrows on the side are exaggerated illustrations of the reciprocal lattice vectors of the moiré superlattice, MoS_2 lattice and HOPG lattice, respectively, where the twisted angle was measured between the MoS_2 and HOPG reciprocal lattice vectors. (c) Filtered FFT image. (d) Topography reconstructed from the inverse FFT on (c). (e, f) Raw data of moiré superlattice topography and FFT image measured under B = 3 T, respectively. (g, h), Raw data of moiré superlattice topography and FFT image measured under B = 0.5 T, respectively. Here we note that the other signal points that were present in the raw data of FFT images of (b), (f), and (h) but were filtered out in our analyses originated from the increased scanning signal resolution in STM after applying a strong magnetic field, which not only enhanced the brightness of each lattice point in reciprocal space, but also made new convolution signals extending outward from lattice points more apparent. Therefore, the extra points extending

outward from the MoS_2 periodic reciprocal space vector correspond to the MoS_2 convolution signals, and the extra points extending from the blue outer ring of the moiré periodic reciprocal space vector corresponding to the moiré convolution signals.

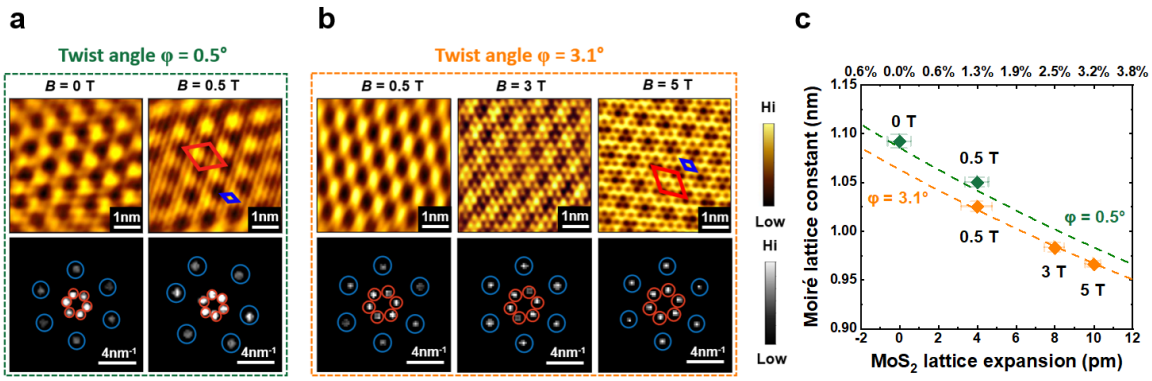

Figure 4.15 Magnetic field-induced ML-MoS_2 lattice expansion as characterized by scanning tunning microscopy (STM). (a,b) Reconstructed moiré superlattice topography (top panels) and the corresponding filtered fast Fourier transformation (FFT; bottom panels) of ML-MoS_2/HOPG at 4.5 K for two (5 nm × 5 nm) regions of the same sample: (a) one (5 nm × 5 nm) region with a twist angle of 0.5° between MoS_2 and HOPG under $B = 0$ and 0.5 T (green); and (b) the other (5 nm × 5 nm) region with a twist angle of 3.1° between MoS_2 and HOPG under B = 0.5 T, 3.0 T, and 5.0 T (orange). The red and blue rhombus in the topographic images outline the unit cell of the moiré superlattice and the MoS_2 lattice, respectively. Red and blue circles in the FFT images outline the corresponding reciprocal lattice sites. The STM bias voltage was fixed at 0.1 V and the tunneling current was fixed at (a) 3 nA and (b) 2 nA. (c) The moiré superlattice periodicity of ML-MoS_2/HOPG and the MoS_2 lattice expansion (green and orange diamonds) are derived from analyzing the FFT graphs and show an excellent match to the in-plane MoS_2 lattice expansion theoretical model (dashed curve). The top axis shows the lattice expansion in percentage.

The filtered ML-MoS_2/HOPG topographic images showed evolving moiré patterns with magnetic field for two distinct (5 nm × 5 nm) regions with a twist angle (φ) of 0.5° (Figure 4.15(a)) and 3.1° (Figure 4.15(b)) at B = 0, respectively. The corresponding reciprocal lattice points for the moiré pattern and ML-MoS_2 were respectively highlighted in red and blue circles in the Fast Fourier transformation (FFT) graphs of the topography, as shown in the bottom panels of Figure 4.15(a) and Figure 4.15(b). With increasing B, a systematically increasing ML-MoS_2 lattice constant as well as a decreasing moiré lattice constant were found from analyzing the reciprocal lattice vectors in the corresponding FFT graphs taken over the same (5 nm × 5 nm) area, whereas the HOPG lattice constant remained the same.[216] As shown in Figure 4.15(c), we found ~3% in-plane lattice expansion for B = 5 T and ~1.3% in-plane lattice expansion for B = 0.5 T, the latter agreed well with the estimate of ~1.4% lattice expansion from the redshift of the E_{2g} Raman mode.[218,219] These results thus provide solid evidence for substantial magnetic field-induced lattice expansion in ML-MoS_2 at low temperature. Moreover, the expected A_{1g} shift from the pure tensile strain of 1.4% would have been about $-0.8\ cm^{-1}$ as predicted by first principle calculations and previous experiments,[218,219] yet a larger shift of $-1.5 cm^{-1}$ was observed in our Raman measurement as shown in Figure 4.13(c). This difference may be understood by noting that the peak position of the out-of-plane A_{1g} phonon mode is much more sensitive to charge accumulation than the in-plane E_{2g} mode,[219] so that the larger redshift found in the A_{1g} mode may be attributed to the presence of net out-of-plane charge distributions[220] and thus supports the occurrence of spontaneous out-of-plane polarization.

4.8 Asymmetric lattice expansion-induced ferroelectric-like polar order

A plausible explanation for our observation of magnetic field-induced giant hysteretic behavior is due to a bistable ferroelectric-like spontaneous out-of-plane polarization, which emerges under anisotropic magnetic field-induced lattice expansion due to the TEC mismatch between ML-MoS_2 and the underlying rigid SiO_2/Si substrate,[212,221,222] leading to asymmetric flexoelectric effect[221] as schematically shown in Figure 4.16. The relevance of the substrate to the occurrence of out-of-plane polar order in ML-MoS_2 is schematically illustrated in Figure 4.16(a), where the side-views for the asymmetric and symmetric rippling effects between the top and bottom sulfur layers are shown for ML-MoS_2 on SiO_2/Si and h-BN/SiO_2/Si substrates, respectively. Our proposed model of asymmetric lattice expansion between the top and bottom sulfur layers of ML-MoS_2 on SiO_2/Si below T_C and under an out-of-plane external magnetic field is further illustrated in Figure 4.16(b), showing the occurrence of broken mirror symmetry.

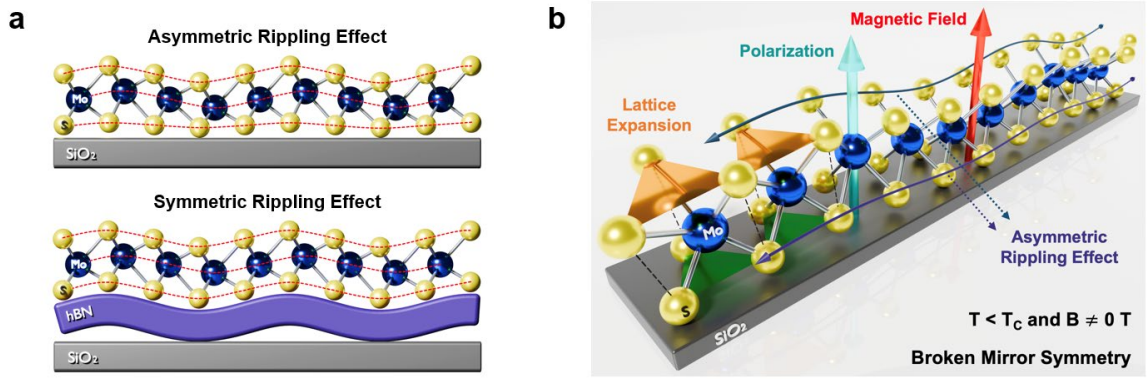

Figure 4.16 A proposed model for the effect of temperature and magnetic field on the structure of ML-MoS_2. (a) Schematic side-views of ML-MoS_2 on either a rigid SiO_2/Si substrate or a buffered h-BN/SiO_2/Si substrate and the resulting respectively asymmetric and symmetric rippling effects on the top and bottom sulfur layers. (b) A proposed model of

asymmetric lattice expansion in ML-MoS_2 on SiO_2/Si for $T < T_C$ and under an out-of-plane external magnetic field, leading to broken mirror symmetry that give rise to the out-of-plane polar order.

Further supporting evidence for this scenario was provided by piezo-response force microscopy (PFM) measurements, which is a commonly used tool to identify polar responses. The PFM hysteresis measurements were conducted utilizing a commercial cryogenic scanning probe microscope system (attoAFM I, Attocube) equipped with a closed-cycle cryostat (attoDRY 2100 with 9 T magnet, Attocube) operating at 1.6 K. A commercial platinum silicide (PtSi) coated tips with a spring constant of 2.8 N/m (NANOSENSORS PtSi-FM) was used to assess hysteresis, driven by a V_{RMS} = 1.5 V ac voltage at a contact-resonance frequency of about 300 kHz. Off-field hysteresis loops were obtained by switching spectroscopic techniques under pulse sequences generated by an arbitrary waveform generator (G5100A, Picotest).

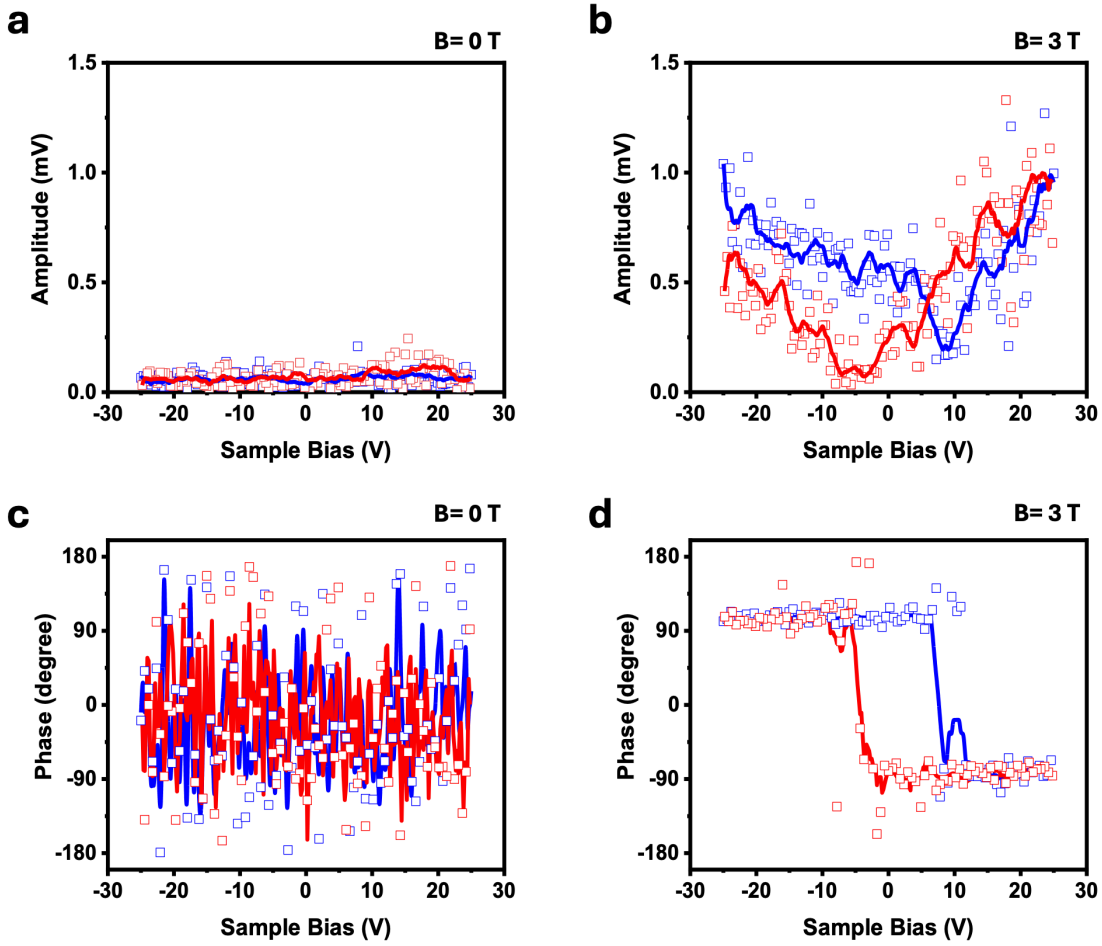

Figure 4.17 Low temperature piezo-response force microscopy (PFM) measurements of ML-MoS_2 at different magnetic fields. (a-b) The amplitude and (c-d) the phase of the PFM, measured at $B = 0$ and $B = 3$ T, respectively. Blue and red curves represent the response when voltage is applied from negative to positive and when reversed from positive to negative, respectively.

As exemplified in Figure 4.17, evident ferroelectric butterfly hysteresis loop emerged at 1.6 K and $B = 3$ T whereas no piezoelectric response was found at $B = 0$ T. his finding indicated that the out-of-plane polar order under a finite out-of-plane magnetic field was switchable by a nonlinear electric field applied by a PFM.[221] Other than net out-of-plane polarization due

to asymmetric magnetic field-induced lattice expansion and rippling in ML-MoS_2 on rigid substrate, local charge disorder due to sulfur vacancies could also contribute to the nonlinear effect found in the PFM measurements. However, the tendency of reduced tensile strain loading with increasing vacancy concentration as the result of decreasing Young's modulus[223] would have led to diminished flexoelectric effect with increasing sulfur vacancies. Moreover, the low sulfur vacancy concentrations (~ 0.2%) in all ML-MoS_2 samples that exhibited polar effects was consistent with insignificant roles of sulfur vacancies in the magnetic field-induced ferroelectric responses (Appendix C, Figure C.1 and Figure C.2

The important role of the substrate in the occurrence of out-of-plane asymmetric lattice expansion and the resulting polar effect was further verified by studying two distinct ML-MoS_2 FETs buffered by ~5 nm thick h-BN between the ML-MoS_2 and the rigid SiO_2/Si substrate. Both buffered FETs revealed no obvious magnetic field-induced counterclockwise hysteresis (Figure 4.18), which was expected because the h-BN buffer had a similar negative TEC[224] and also exhibited low lateral friction[225] relative to the MoS_2 layer so that the centrosymmetry-breaking required for ferroelectric-like out-of-plane polarization was largely prevented in the buffered ML-MoS_2 FETs on h-BN/SiO_2/Si substrates (Figure 4.18).

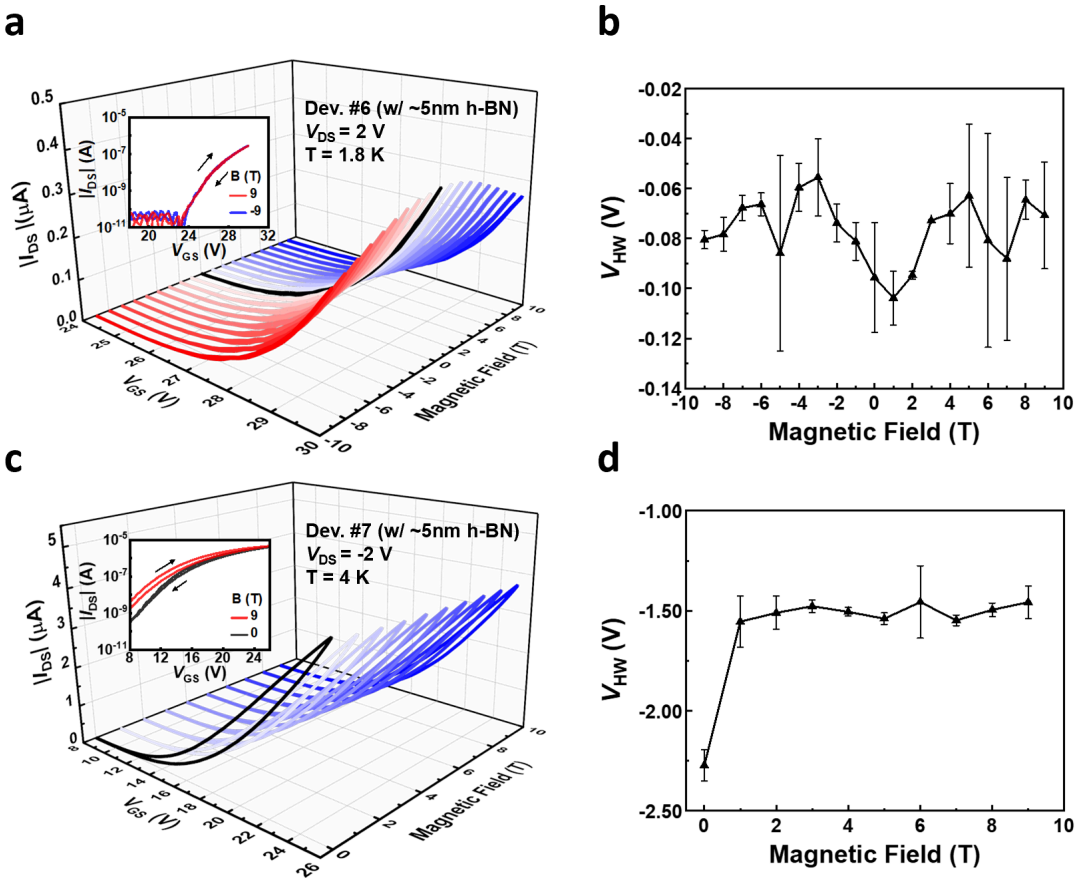

Figure 4.18 Magnetic field-independent clockwise hysteresis at 1.8 K for h-BN buffered devices. (a) $|I_{DS}|$-*vs.*-V_{GS} hysteresis under magnetic field from 9 T to –9 T with V_{DS} = –1 V measured at 1.8 K. As exemplified in the semi-log inset, a clockwise hysteresis loop (indicated by black arrow) that was almost independent of magnetic field was observed under B = 9 and B = –9 T. (b) V_{HW}-*vs.*-B taken from a), showing that the negative value of V_{HW} for clockwise hysteresis is independent of magnetic field. (c) $|I_{DS}|$-*vs.*-V_{GS} hysteresis under magnetic field from 0 T to –9 T with V_{DS} = –2 V measured at 4 K. As exemplified in the semi-log inset, a clockwise hysteresis loop (indicated by black arrow) that was almost independent of magnetic field was observed under B = 0 and B = –9 T. (d) V_{HW}-*vs.*-B taken from c), showing that the negative value of V_{HW} is independent of magnetic field except for the first few starting cycles at B = 0.

4.9 Conclusion

Overall, our fully reproducible experimental findings from five distinct FET devices of ML-MoS_2 on SiO_2/Si substrates suggested that the out-of-plane magnetic field-induced ferroelectric-like counterclockwise hysteresis was robust at low temperature and reversible upon removing the magnetic field, and the absence of such phenomena in two buffered FET devices of ML-MoS_2 on h-BN/SiO_2/Si further accentuated the important role of rigid substrates in inducing the asymmetric lattice expansion, which was essential for the out-of-plane electric polarization. The magnetic field-induced lattice expansion in ML-MoS_2 at low temperatures is likely associated with the occurrence of a magnetic field-induced structural phase transformation, although the microscopic mechanism and the nature of this phase transformation remain unclear. A possibility may be related to lifting the valley degeneracy in ML-MoS_2 by magnetic field via spin-valley coupling, thereby resulting in a real-space structural transformation. Additionally, the correlation between the size of hysteresis (V_{HW}) and the magnitude of out-of-plane magnetic field ($|B|$) is suggestive of multiferroic-like behavior. Overall, a careful *ab initio* calculation that takes the effects of magnetic field, temperature, sulfur vacancies, and substrate into consideration will be necessary to fully account for our observation and to unravel the underlying physical mechanism, which is beyond the current scope of our work. Regardless of the microscopic physical origin, the giant magnetic-field induced ferroelectric-like responses in the ML-MoS_2 FET devices exhibited strong stability and reproducibility, thus promising for such technological applications as cryo-temperature ultracompact non-volatile memories, memtransistors, and ultrasensitive magnetic field sensors. Furthermore, the observed ferroelectric behavior induced by asymmetric lattice expansion could potentially be generalized to other monolayer electronics, which opens exciting new possibilities of using nanoscale strain engineering of the substrate to achieve similar effects in various two-dimensional materials, paving a way towards innovative design and development of nanoelectronics for advanced nanotechnology.

Chapter 5

CRYOGENIC SCANNING PHOTOCURRENT SPECTROSCOPY FOR MATERIALS RESPONSES TO STRUCTURED OPTICAL FIELDS

5.1 Introduction

Novel optoelectronic properties of materials, such as the light emitting mechanisms and light-controlled matter responses, have attracted intense research interest in the past two decades.[226,227] Two notable ways of engineering light-matter interactions focus on the characteristics of the incident light and the optoelectronic properties of the material. Besides varying the energy and polarization of the photon, the former approach may further include the spin and orbital degrees of freedom. Circularly polarized light that carries a spin angular momentum (SAM) of $\pm\hbar$ has been exploited to achieve selective excitations in materials, especially those without lattice inversion symmetry. On the other hand, twisted light that carries an orbital angular momentum (OAM) of $\pm \ell\hbar$ (where ℓ is an integer that represents the topological charge of photons) is believed to have a wide range of applications due to its full utilization of the vector character of the electromagnetic nature of light,[228] which may be employed in such areas as optical tweezers,[229] conventional information transfer,[230] and emerging quantum information technology.[231]

Transition metal dichalcogenides (TMDs) of the 2H phase, 2H-MX_2 (M = transition metals, X= S, Se and Te), are a class of two-dimensional (2D) semiconducting quantum materials whose optoelectronic responses may be tuned via strain,[232] defect,[233,234] and meta-surface engineering.[235–237] The absence of lattice inversion symmetry and the presence of spin-orbital coupling (SOC) in 2H-MX_2 further enriches the fine-tunning handles,[238] allowing for unique chirality-controlled valley-specific excitation and transport.[239] Among 2H-TMDs, monolayer molybdenum disulfide (ML-2H-MoS_2, aka ML-1H-MoS_2) possesses a direct

bandgap of 1.8 eV and SOC-induced valence band splitting of ~150 meV,[240–242] leading to chiral-selected valley-polarized photocurrent[243] and circular polarization-maintained photoluminescence.[244,245] Moreover, under the excitation of *twisted light*, which refers to light with finite orbital angular momentum (OAM) $\pm \ell\hbar$ (where $\ell = 1, 2, 3\ldots$ is the topological charge), OAM light-induced enhancement in the photovoltaic effect[70] and intervalley transitions[71] with increasing ℓ has been demonstrated at the excitonic resonant energy.

Photocurrent spectroscopy (PCS), a powerful experimental tool for studying the optoelectronic responses of semiconducting materials, measures light-induced photocurrents as a function of the photon energy.[246] This approach is capable of probing the complex excitonic states of semiconductors[46,247] and further identifying dark excitons associated with forbidden optical transitions[248] when the PCS measurements are combined with electrical gating and an external magnetic field. Here we report the development of a scanning PCS system with spatially and SAM/OAM-resolved capabilities and further apply this system to characterizing the optoelectronic responses of ML-MoS_2 to SAM/OAM light at cryogenic temperatures and under finite magnetic fields. Our studies reveal a strongly enhanced Landé *g*-factor in monolayer MoS_2 due to the formation of intervalley excitons in the presence of magnetic fields, as well as monotonically increasing photocurrents with increasing $|\ell|$ due to the enhanced formation of Rydberg and dark excitons by the OAM light. These findings thus demonstrate the versatility of our scanning PCS system for investigating the excitonic physics, optical selection rules, and the optoelectronic responses of novel quantum materials and engineered quantum devices to structured light.

5.2 System setup

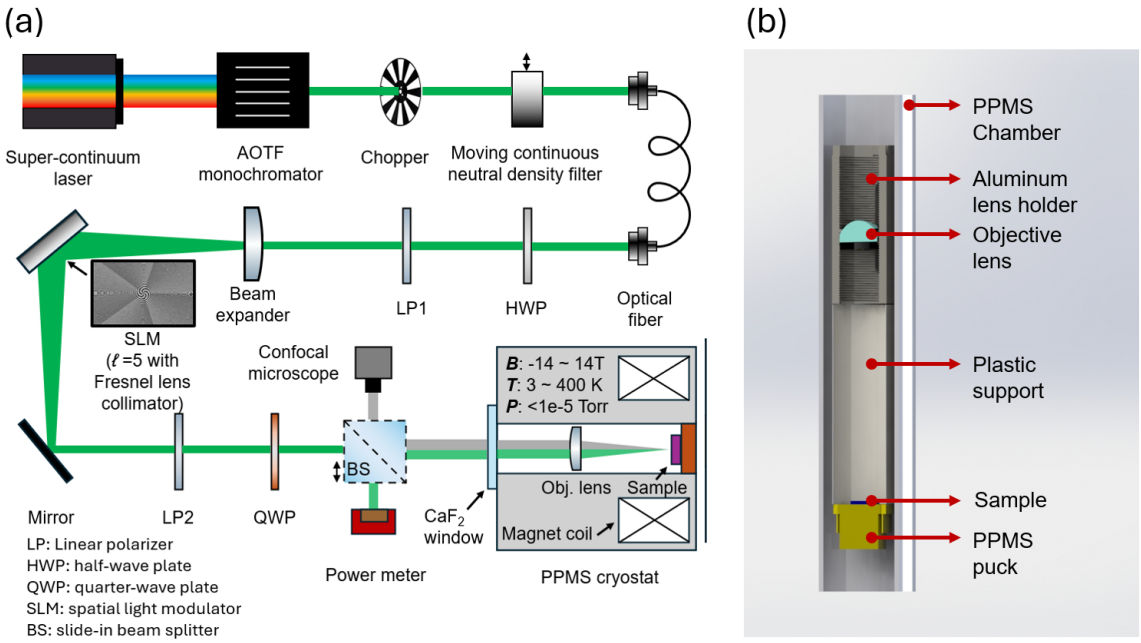

Figure 5.1 Experimental setup for variable temperature (3 – 400 K) photocurrent spectroscopy (PCS). (a) Schematic layout of the SAM/OAM PCS system. (b) Schematic cross-sectional view of the objective lens holder and support inside the cryostat chamber.

The PCS instrument comprises three major parts: 1) a super continuum laser-based photon generation system, 2) an OAM and SAM generation module with a confocal microscope, and 3) a cryostat with electronic detection and magnetic field control (Figure 5.1(a)). The super-continuum *superK Extreme* laser (NKT photonics) outputs a 4-Watt white light which is filtered using *superK Select* (NKT photonics, VIS 1x). The combined photon generation setup outputs linearly polarized light of wavelengths ranging from 430 nm to 700 nm and a factory-characterized linewidth of 0.5 nm – 1.85 nm, which corresponds to an energy resolution of ~ 3 meV. A mechanical chopper (Thorlabs, MC2000B and MC1F10HP, 20 – 1000 Hz) sets up the base frequency for photon illumination and photocurrent detection using a lock-in technique. The power output was then adjusted by a moving continuous neutral

density (cND) filter (Thorlabs, NDL-25C-2, optical density range of 0.04 to 2) carried by a step-motor-controlled translation stage with position repeatability < 3 μm (Zaber-motion, XLSQ600B). Further power adjustment may be conveniently achieved by including additional higher OD neutral density filters in the optical path.

A fiber delivery system (NKT photonics, FD7) with a customized XYZR mount is used to collect the power-adjusted light and provide a mechanically flexible delivery of light to the customized OAM module. The customized OAM module includes a set of half-wave plates, a linear polarizer, and a beam expander, delivering expanded light onto the spatial light modulator (SLM) with a linear polarization aligned with the extortionary axis of the liquid crystal-based panel of the SLM (Southport, JadeDot-LD). The SLM uses an algorithm-computed 8-bit (1920 pixel × 1200 pixel) pattern that not only generates the OAM pattern for each wavelength but is also capable of x-y beam steering while providing focus adjustment with the Fresnel lens collimator algorithm (Figure 5.1(a)). The OAM module also includes a confocal microscope setup that could be engaged via a slide-in beam splitter. This handy slide-in design helps locate the sample and check the beam quality, which can be removed during measurement to avoid complex wavelength-dependent polarization inconsistency. After the OAM generation, a linear polarizer (Thorlabs, WP25M-UB) and a rotary-mounted (Thorlabs, K10CR2/M) quarter-wave plate (Thorlabs, SAQWP05M-700) are used to generate circular polarization.

The instrument operates in either a room-temperature configuration or a cryostat configuration. The room-temperature setup consists of an achromatic objective lens, a sample holder assembly with the PPMS Userbridge for electronic measurements and a XYZR stage for sample-side positioning. The cryogenic setup is built on a commercial PPMS (Physical Property Measurement System, Quantum Design, Dynacool). A CaF_2 optical window and a customized objective lens holder [Figure 5.1(b)] is used to achieve

collimated SAM/OAM light spot on the sample while conducting concurrent electrical transport measurements.

The instrument achieves a stable temperature of 3 K with 12 mW redundant cooling power under a magnetic field of ±14 T, or 2 K with 4 mW redundant cooling power. To prevent exposure to the stray field up to 10 mT at $|B| = 14$T, the laser system and the OAM module were enclosed in their customized aluminum shields. The maximum spectroscopic-uniform power output between 500 nm and 700 nm was 20 μW ± 3% with a spot radius of 2.5 μm for zero OAM in the linearly polarized condition, while being chopped at 311 Hz with 50% duty cycle. The wavelength coverage may be extended to the full 430 nm – 700 nm spectral range at the expense of reduced uniformity in the spectral power output due to the sharply decreasing spectral power density of the laser below 500 nm. The power delivered by light to the sample was measured with the room-temperature configuration by placing a power meter (Thorlabs, PM400 and S120C) at the sample location. Further tests revealed that there was no discernible difference in the power reading whether the power meter was placed at the sample position of the room temperature configuration or at a distance comparable to the sample position in the cryostat configuration. Therefore, detailed wavelength-dependent power calibrations to be described below were carried out in the room temperature configuration. We further note that the uniformity of the spectroscopic power output was limited by the long-term stability of the laser (±3% in 2 hours) and the measurement uncertainty of the photodiode head of the power meter (±3%).

Overall, the instrument overcomes several critical challenges: 1) achieving 500 nm – 700 nm spectroscopic generation of OAM light using a SLM; 2) integrating PCS with a commercial cryostat setup within a limited space and a long working distance; 3) scanning a high-quality light spot on micron-scale ML-TMD field-effect transistors (FETs); 4) performing optical and back-gate tunable electronic transport measurements concurrently under magnetic field up to ±14 T and temperatures down to 3 K.

5.3 System evaluation

Spectroscopic orbital angular momentum generation

One of the key challenges for the PCS instrument is that the commercial SLM is usually calibrated at one specified wavelength. To achieve achromatic modulations from the SLM, we need to produce a wavelength-dependent linear mapping between 8-bit greyscale level (*GS*, integer from 0 to 255 as the input of SLM for each pixel) and optical phase modulation 0 to 2π. As shown in Figure 5.2(a), the calibration setup consists of two orthogonally polarized linear polarizers placed before and after the SLM, whose extraordinary axis is pointing out from the paper.[249] Assuming that the spatially-uniform phase modulation of the SLM is only on its extraordinary axis and using Jone's matrix $\begin{bmatrix} e^{-i\varphi(GS)} & 0 \\ 0 & 1 \end{bmatrix}$, the measured intensity at the power meter (I_{out}) is $I_{out} = I_{in}(1 - \cos\varphi(GS))/4$, where the $\varphi(GS)$ is the phase modulation applied by the SLM at a greyscale level *GS*.

The manufacture's single wavelength hardware calibration procedure was performed first at 700 nm, which resulted in a linear map between the *GS* input 0-255 and the phase depths of 0-2.2 π with a phase offset comparing to expected I_{out} described above [Figure 5.2(b)]. After the hardware calibration, we measured wavelength dependence between 500-700 nm [Figure 5.2(c)] and found two issues that need further calibration: firstly, roughly 700/λ periods were observed for shorter wavelengths, where the *GS* remapping was needed for each wavelength to cut off those excessive periods; secondly, the observed wavelength-dependent phase offset $\varphi_0(\lambda)$, shown as horizontal shifts in Figure 5.2(c), required additional corrections. The above two issues were corrected via a customized Python-based script for the instrument, which first normalized and fitted the measured intensity *I*-vs.-*GS* data to a set of $I_{\text{normalized}}(\lambda) = A(\lambda)\ \sin(GS/T(\lambda) + \varphi_0(\lambda))$ functions, with $A(\lambda)$ and

$T(\lambda)$ being the fitted amplitude and period at a wavelength λ, respectively. Based on the fitted result, a $GS_{\text{start}}(\lambda)$ was chosen where the phase modulation of the SLM was 0 and the $GS_{\text{end}}(\lambda)$ was calculated as $GS_{\text{end}}(\lambda) = GS_{\text{start}}(\lambda) + T(\lambda)$. Thus, the greyscale was remapped via the formula: $GS_{\text{remapped}}(\lambda) = \text{round}\left(\frac{GS}{255} * (GS_{\text{end}}(\lambda) - GS_{\text{start}}(\lambda)) + GS_{\text{start}}(\lambda)\right)$ such that for the whole range of *GS* from 0 to 255, the SLM produced a phase modulation linearly from 0 to 2π for all measured wavelengths. The calibration ensured the input *GS* stayed in the integer norm and will cause negligible (< 1%) accumulated phase error. In our experiment, the measured wavelength was 500-700 nm with 1 nm step size and the sub-nm correction was achieved by interpolating the experimentally extracted $GS_{\text{start}}(\lambda)$ and $GS_{\text{end}}(\lambda)$ values using the Pchip interpolator algorithm.[250] The corrected results showed nearly one exact period with negligible phase offset in Figure 5.2(d). After carrying out both hardware and software calibrations, signature donut-shape spots for the OAM light of different ℓ values with phase singularity at the center of each light spot was achieved (Figure 5.2(e) and Figure 5.3) on a standard silicon chip mounted at the sample end.

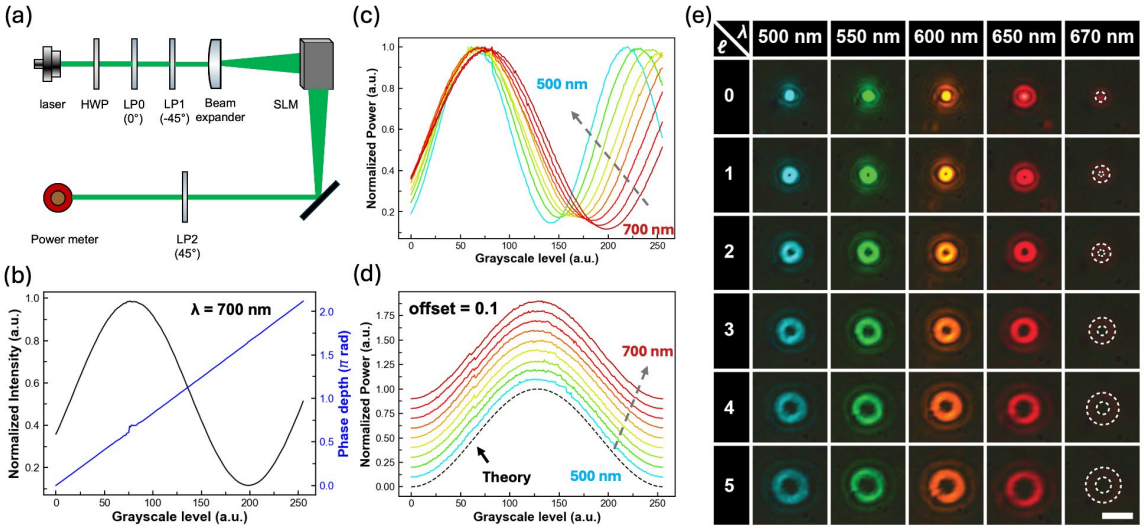

Figure 5.2 Generation of OAM-light spectroscopy: (a) Schematics of the optical experiment layout. (b) Measured power (left axis) and indicated phase depth (right axis) versus the grayscale level (*GS*) after hardware calibration. (c-d) Wavelength dependence of normalized light power *vs.* applied *GS* before (c) and after (d) software calibration. The black dashed line showed the theoretical expectation, *i.e.*, $I_{out} \propto [1 - \cos\varphi\,(GS)]$. (e) Table of the generated OAM light spots for different wavelengths and ℓ values after both hardware and software calibrations, captured by a confocal microscope of the setup at the sample end on a standard SiO_2/Si chip. The white scale bar represents 10 μm. Due to the internal CCD filter, the intensity of the spot image drops sharply for $\lambda > 650$ nm. Therefore, thin white dashed lines were added to outline the inside and outside rims of the donut-shape spots in the $\lambda = 670$ nm column for visual clarity.

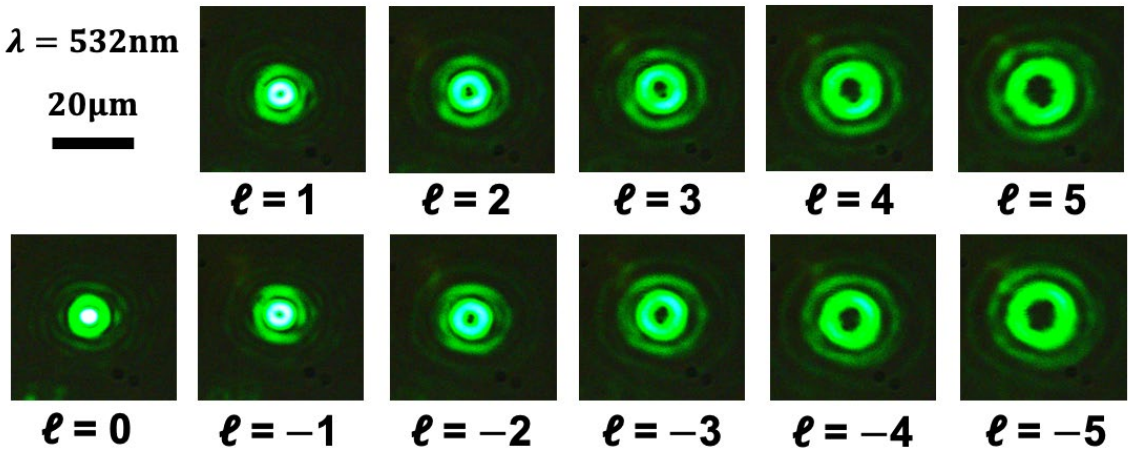

Figure 5.3 Spot table for positive and negative ℓ values. Spot image for ℓ = -5 to 5 at wavelength of 532nm. The black scale bar is 20 μm.

Spectral power uniformity

To ensure that the measured spectroscopic photocurrents are purely from the optoelectronic responses of the sample, spectroscopic dependences on the laser power due to optical components of the instrument, such as wave plates and polarizers, must be eliminated. Therefore, a spectral power calibration for the instrument is needed. The instrument employed a moving continuous neutral density (cND) filter to adjust the system power output, and a power meter placed at the sample position was used to measure the power output [Figure 5.4(a)]. The power $P = f(x, \lambda)$ measured at spot position x and wavelength λ was then interpolated and used as a calibration file such that when a desired power P_1 at wavelength λ_1 was needed, the corresponding position x_1 of the cND filter could be queried as $x_1 = f^{-1}(P_1, \lambda_1)$ via an integrated computer algorithm. With such corrections, the instrument with a constant spectroscopic power output (power fluctuation < ±3%) was

achieved [Figure 5.4(b) colored dots], in stark contrast to the highly wavelength dependent output power without calibration (Figure 5.4(b) black dots) due to the spectral power density characteristics of the super-continuum laser. The SAM and OAM spectral power uniformity was also tested for various wavelengths as shown in Figures 5.4(c) and 5.4(d), respectively. These results indicated that a consistent spectral power uniformity within ±3% was achieved under varying polarizations, OAM, and power setpoints, thus validating the suitability of our instrument for spectroscopic photocurrent measurements.

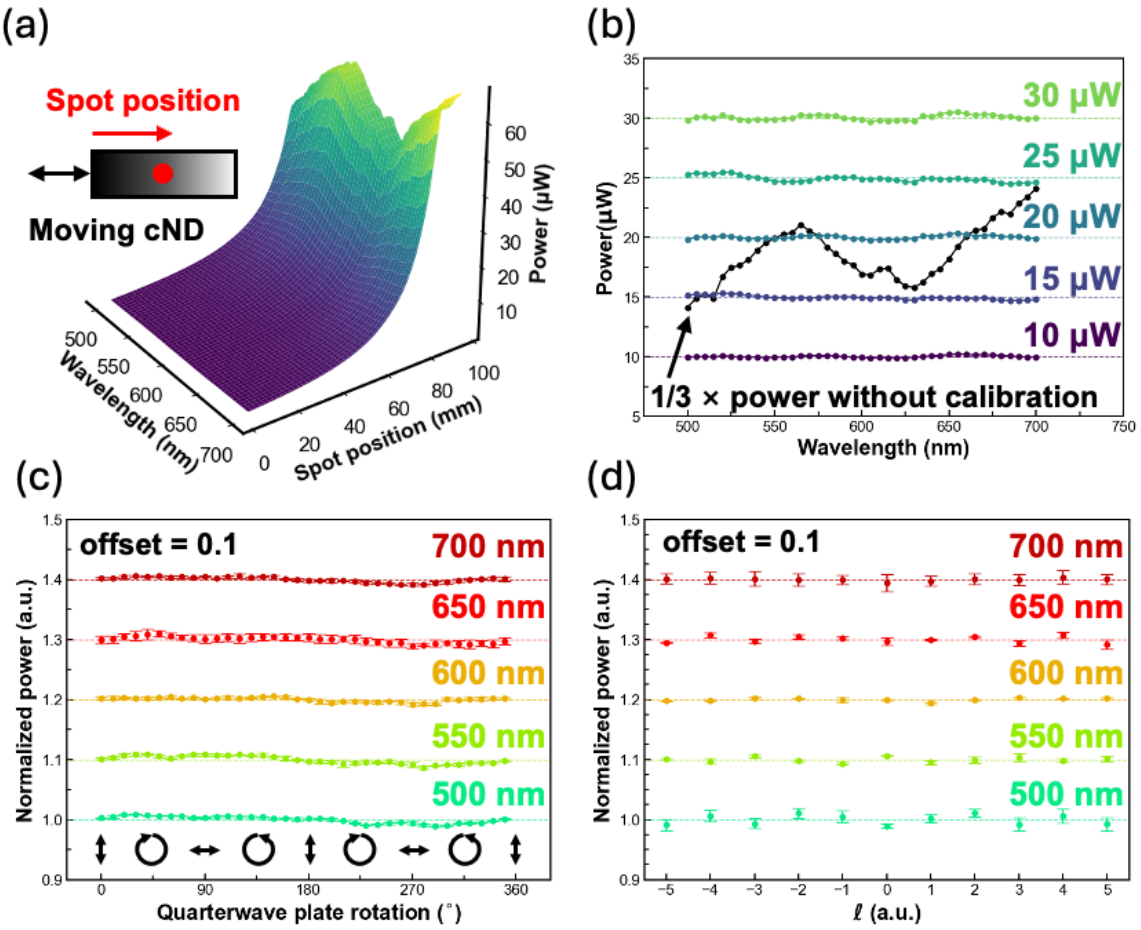

Figure 5.4 Spectral power uniformity measurement and performance testing. (a) Sample-side power as a function of wavelength and the spot position passing through a moving continuous neutral density (cND) filter. The inset illustrates the spot position relative to the moving cND filter. (b) Measured laser raw power output (black dots) on the sample-end before system spectral power output calibration and measured constant spectral output (colored dots) at 10, 15, 20, 25, and 30 μW setpoints after calibration. (c) Measured sample-side polarization-dependent power normalized by a setpoint of 20 μW for wavelengths between 500 nm to 700 nm. (d) Measured sample-side ℓ-dependent power normalized by a setpoint of 20 μW for wavelength between 500 nm to 700 nm.

Scanning capability

The scanning capability of the PCS system was realized by offsetting the SLM pattern center. As shown in Figure 5.5, manual X offset and Y offset was added to shift the spot location in real space. In scanning PCS measurement, it is vital to achieve a spatially uniform power projection regardless of the spot position such that the spatial-dependent PCS spectrum will faithfully reflect the spatial properties of the material, such as local defect or strain. While the real-space spatial movement of the spot may be achieved within a reasonably small offset om SLM pattern, the cyclic boundary conditions used in the pattern-generation algorithm (Figure 5.5 (d)) may lead to an increasingly large power losses and spot quality degradation for a larger offset. In addition, the expanded beam carries intrinsic gaussian intensity distribution over the SLM, adding another source of spatial power variation. Empirically, the compliance of power fluctuation less than 3% is a harsher limit than spot quality in terms of donut-shape's visual quality with a finite ℓ. Therefore, it is important to characterize the spatial power uniformity and determine the usable scanning range in terms of applicable X and Y offsets to the SLM pattern. This usable X,Y offset range, barred by visually examined quality of the spot and measured <3% power fluctuation within, thus characterizes the scanning area of the instrument.

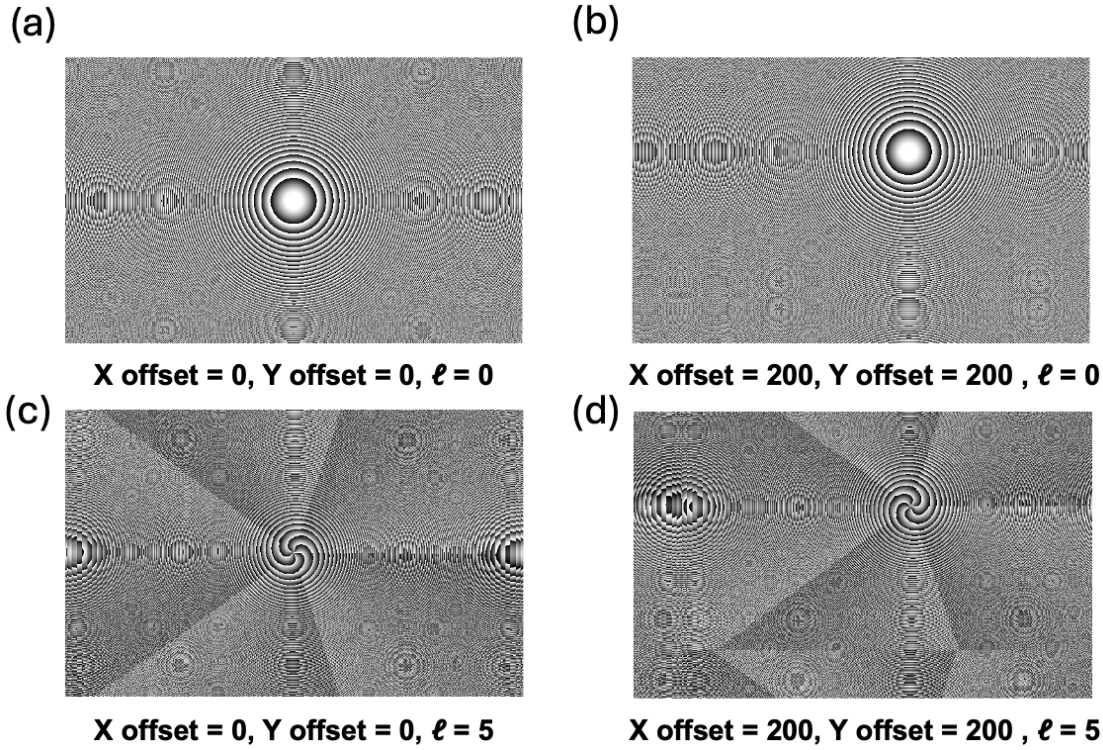

Figure 5.5 SLM pattern with X and Y offset for beam steering. (a-b) ℓ =0 SLM pattern with spatially offset of (a) X offset = Y offset = 0 and (b) X offset = Y offset = 200. (c-d) ℓ =5 SLM pattern with spatially offset of (a) X offset = Y offset = 0 and (b) X offset = Y offset = 200. Z offset = 0.31 were used for all patterns.

To measure the scanning power uniformity, a power meter was put at the sample side in room-temperature configuration, measuring spot power with a rectangular grid of X, Y offset combinations. We first measure the power within a 200×200 pixel grid with increments of 10 pixels each direction [Figure 5.6 (a)] then a zoom-in section of 50×50 pixel grid with increment of 2 pixel each direction [Figure 5.6(b)]. We found a 60×50 pixel rectangular grid (whose boundary is shown as the purple dashed rectangle in Fig 5.6(b)) may be positioned within 97% boundary, typically covering an area of roughly (35×25) μm^2 with resolution of 0.5 μm/pixel in cryogenic configuration with an achromatic objective lens of 75mm focal

length. The actual scanning area and resolution may vary upon a different choice of objective lens, however, a similar strategy may be used to determine the scanning area and resolution using a known sample. Furthermore, the 3% power fluctuation may be overcome by incorporating an offset-dependent power correction profile in the future, in addition to the spectral power correction achieved by the moving cND filter.

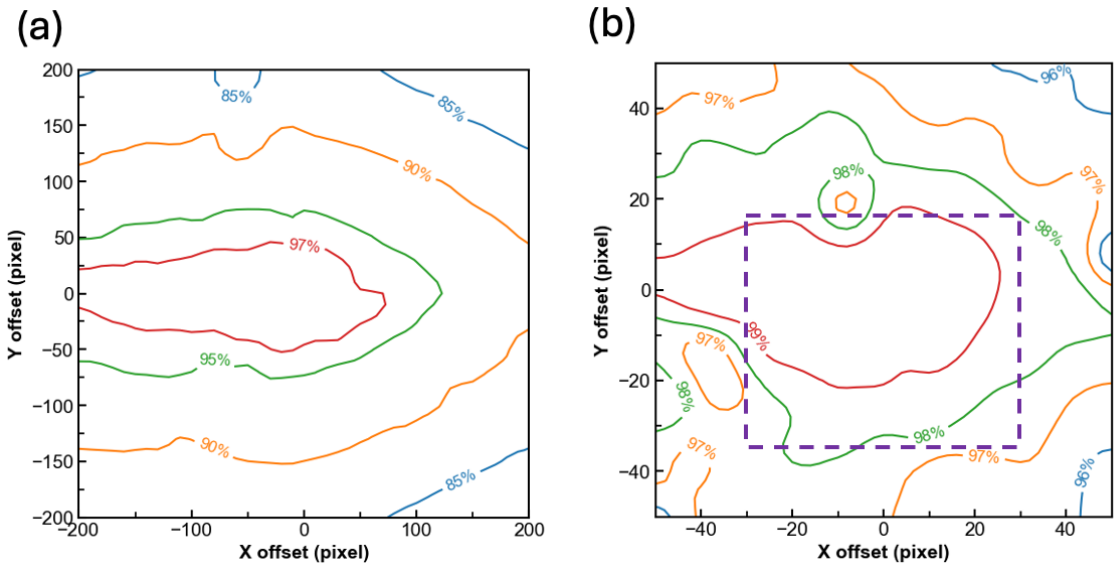

Figure 5.6 Spatial power uniformity measurement. (a-b) Spatial power uniformity measured in a (a) 200×200 pixel and (b) 50×50 pixel rectangular grid, respectively under 532 nm. The colored contour lines show the power percentage level compared to the power measured at X offset = Y offset = 0 value in each plot. The purple dashed box indicates the scanning area of the instrument.

5.4 Implementing the scanning SAM/OAM-PCS

The performance of the scanning SAM/OAM-PCS system was evaluated on ML-MoS_2 field-effect transistors (FETs). The ML-MoS_2 single crystal samples used for the FETs were synthesized on sapphire substrates by chemical vapor deposition (CVD), and the device

fabrication processes were similar to those reported before for electrical transport studies[251,252] except that an additional 5 nm thick h-BN layer between MoS_2 and SiO_2 substrate were included for the FETs devices used in the PCS studies to eliminate magnetic field-induced polar order[251] in ML-MoS_2 on SiO_2 substrate at cryogenic temperatures. A typical diagram for device and circuit is shown in Figure 5.7. The performance of the scanning SAM/OAM-PCS system was evaluated on ML-MoS_2 field-effect transistors (FETs). The ML-MoS_2 single crystal samples used for the FETs were synthesized on sapphire substrates by chemical vapor deposition (CVD), and the device fabrication processes were similar to those reported before for electrical transport studies[251,252] except that an additional 5 nm thick h-BN layer between MoS_2 and SiO_2 substrate were included for the FETs devices used in the PCS studies to eliminate magnetic field-induced polar order[251] in ML-MoS_2 on SiO_2 substrate at cryogenic temperatures.

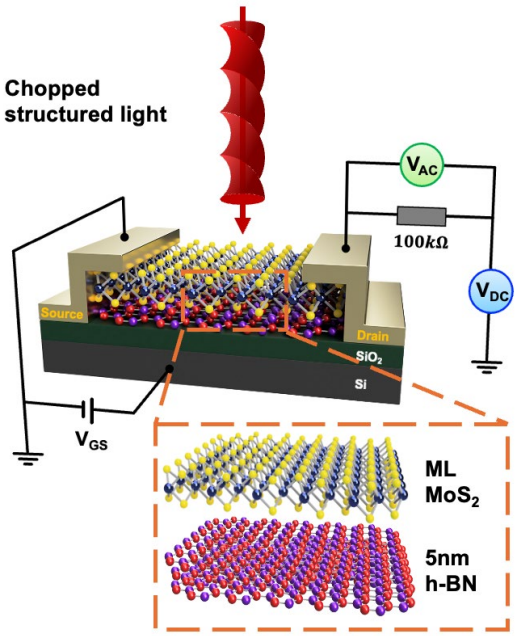

Figure. 5.7. Schematics of the ML-MoS_2 FET device and the electrical circuit for photocurrent measurements.

For measurements of the photocurrent, a 100 kΩ (±0.01%) precision resistor served as both a protection resistor and an AC voltage measurement target, as illustrated in Figure 5.6. A DC bias voltage V_{DS} across the sample and the precision resistor series was applied to achieve a channel current of 10 nA/μm. Unless specified, all photocurrent measurements were taken with the cryogenic configuration at 3 K. The photocurrent I_{pc} was measured with a lock-in amplifier across the precision 100 kΩ resistor in series with the sample at a chopper frequency of 311 Hz. The backgate voltage was swept to a negative voltage of −20 V before obtaining each spectrum in order to remove the residual carriers.[253]The backgate voltage was swept to a negative voltage of −20 V before obtaining each spectrum in order to remove the residual carriers.[253]

In the following part of this section, we illustrate four applications of the PCS system to deriving various optoelectronic properties of ML-MoS_2, which include: 1) gate-tunable cryogenic photocurrent spectroscopy measurements; 2) scanning PCS measurements for spatially resolved excitonic spectra; 3) SAM-resolved PCS measurements in magnetic fields for determining the effective Landé *g*-factor; and 4) OAM-resolved PCS studies of enhanced optoelectronic responses induced by OAM light.

Basic photocurrent spectroscopy studies

The ML-MoS_2 device was first measured in the dark environment to obtain its baseline electrical performance, as shown in Figure 5.8. The I_{DS}-*vs.*-V_{DS} curve measured at T = 3K, B = 0T and V_g from 8V to 32V with 2V steps (Figure 5.8(a)) shows a near-ohmic behavior, similar to device performance seen in the last chapter. The threshold voltage V_{th} for this particular device is measured to be 22.5 V in the dark condition.

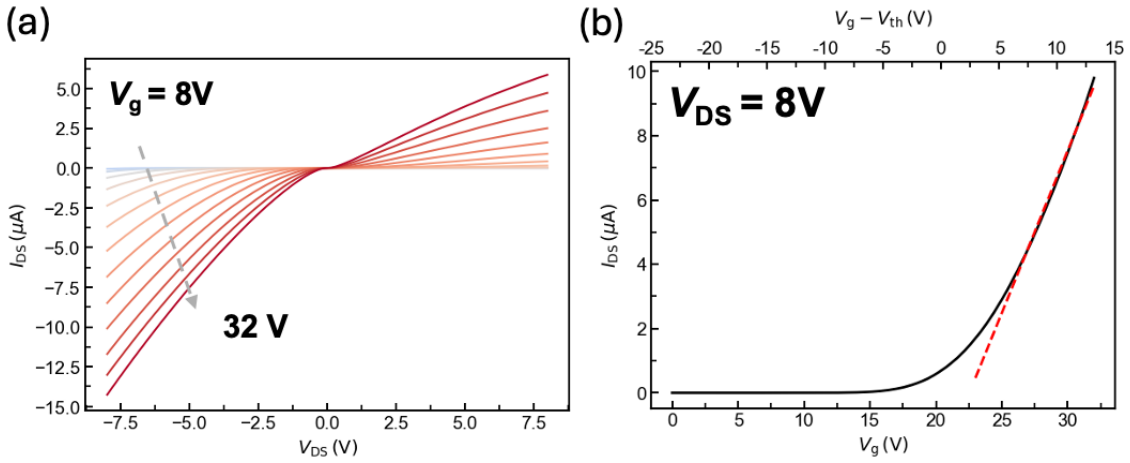

Figure 5.8 Electrical characterization of ML-MoS_2 FET device at T = 3K. (a) Gate-dependent I_{DS}-*vs.*-V_{DS} at T = 3K, B = 0 and V_g from 8V to 32V with 2V steps. (b) Typical I_{DS}-*vs.*-V_g curve taken at V_{DS} = 8V with linear fitting (red dashed line) whose x-axis intercept determines the threshold voltage V_{th} = 22.5V.

The photocurrent spectroscopic response of the ML-MoS_2 FET was measured under different V_g (Figure 5.9(a)), where the A-exciton (X^A) and B-exciton (X^B) are marked in red (1.956 eV) and blue (2.098 eV,) dashed line, respectively. The valence band splitting of 142 meV ± 4.3meV was measured as the energy difference between A-exciton and B-exciton, which is manifested by electron spin-orbit coupling. The A(B)-exciton peak intensity is extracted in Figure 5.9(b) where clearly a bulge was seen at around $V_g - V_{th}$ =1~5V. This is a result of decreasing exciton transition at higher V_g due to Pauli blockade and increasing photocurrent due to increasing channel conductance at higher V_g.[46] Colormap of measured photocurrent as a function of photon energy and gate voltage was shown in Figure 5.9(c), where each spectrum taken at different V_g was normalized to A-exciton peak intensity shown in Figure 5.9 (b). Under the applicable V_g up to 30 V, no obvious signature of trion was observed.

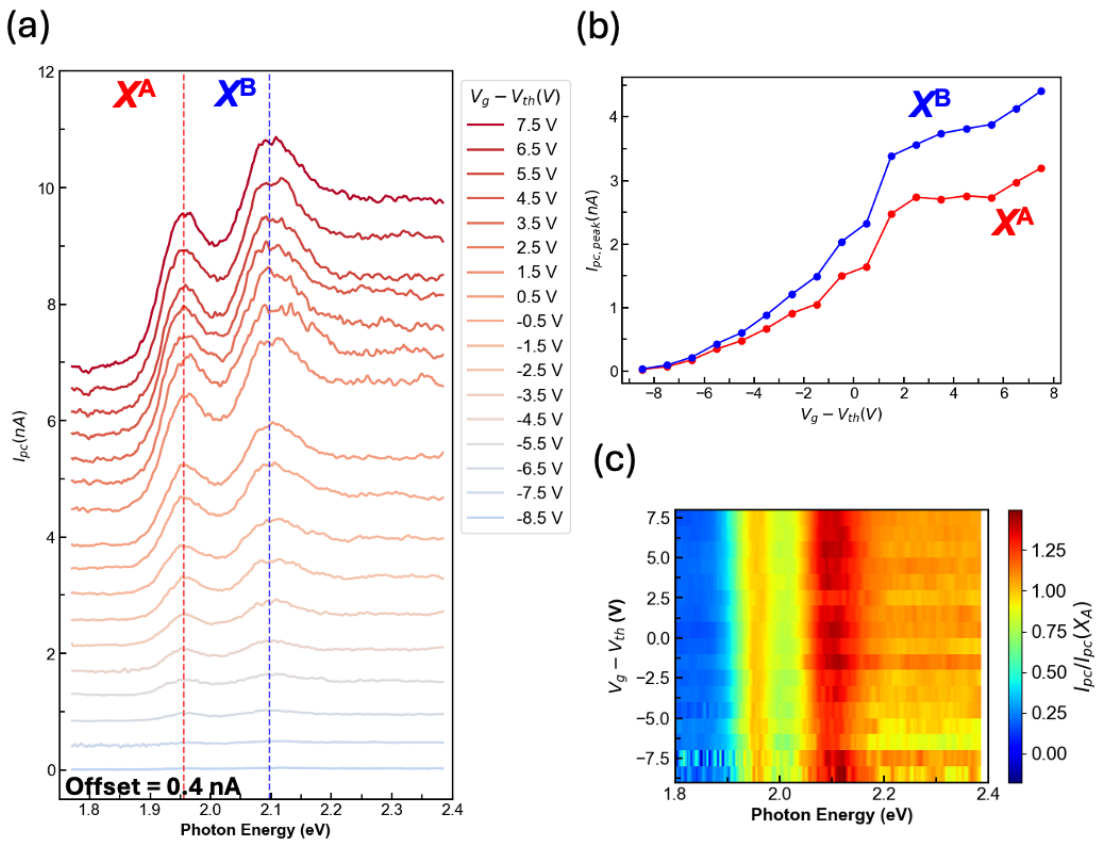

Figure 5.9 Gate-dependent PCS measurement. (a) Gate-dependent PCS measurement in line plot under $T = 3$ K, $B = 0$ and $V_{DS} = 8$ V. (b) Extracted peak intensity for A and B exciton under different V_g. (c) Color map of photocurrent measured as a function of gate voltage and photon energy. Each spectrum was normalized to their bright A-exciton peak intensity.

Scanning RCP-photocurrent spectroscopy

The scanning capability of our instrument was evaluated by measuring the spatially dependent RCP-PCS on a ML-MoS_2 FET, with approximately twenty photocurrent spectra taken over a spatial region between the source (S) and drain (D) contacts and the sample, as illustrated in the optical micrograph in Figure 5.10(a), where the red arrow indicates the scanning direction, and the red dots represent the locations where the spectra were taken. The measured spectra were fitted then normalized to the bright A-exciton peak amplitude as shown in Figure 5.10 (b). The A-exciton (X^A) and B-exciton (X^B) peak positions are marked in red (1.956 eV) and blue (2.098 eV,) dashed lines in Figure 5.10(b), respectively. The extracted amplitudes of X^A and X^B were shown in Figure 5.10(c), where amplitude homogeneity in the sample region was apparent. The sharp increase of both X^A and X^B amplitudes near the source contact was due to band-bending-induced carrier saturation, similar to the findings in previous reports.[254,255] Over the metal contact regions, in addition to the expected sharply diminished exciton amplitudes (Figure 5.10(c)), the emergence of the A-trion (T^A, black dashed line in Figure 5.10(b)) accompanied by a suppressed B-exciton amplitude was indicative of exciton-plasmon interactions[256,257] and charge transfer. [258,259]

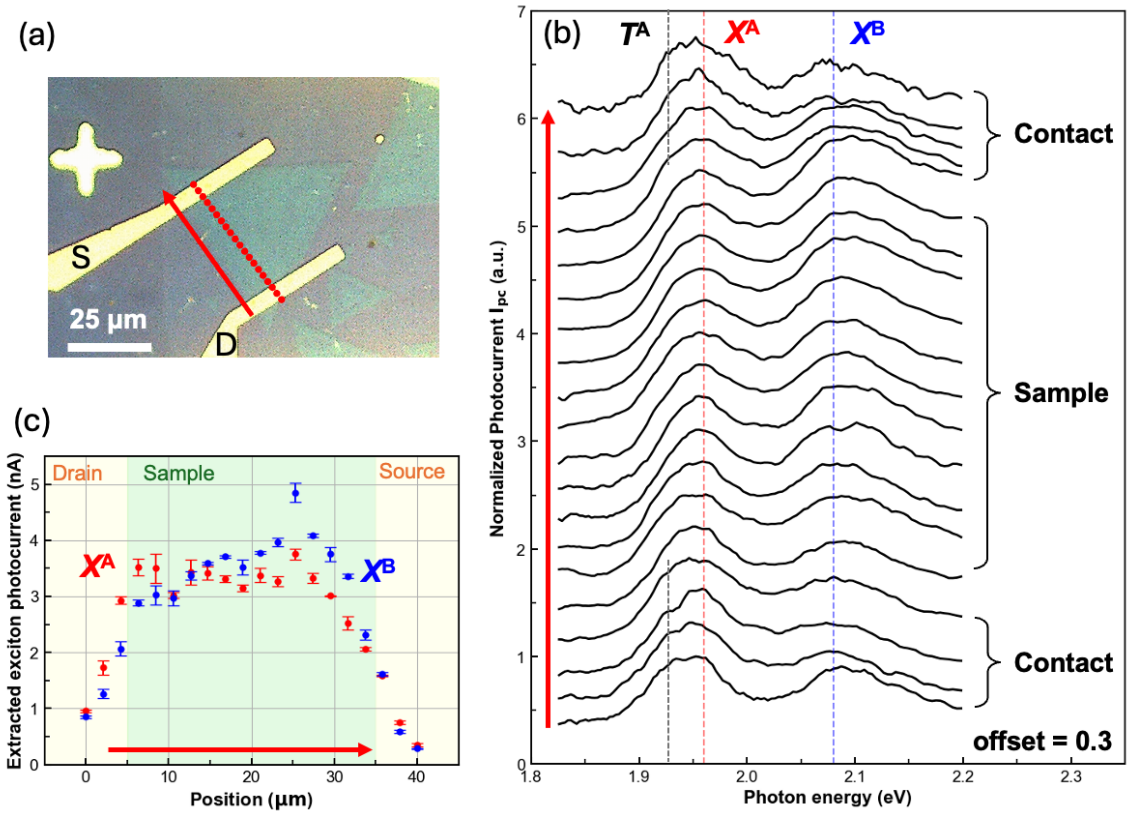

Figure 5.10 Scanning RCP-PCS on a ML-MoS_2 FET. (a) Optical micrograph of the FET device. The red arrow indicates the scanning direction, and the array of red spots marks the measurement locations. (b) Spatially dependent photocurrent spectra normalized to the bright A-exciton peak amplitude. Each spectrum was taken at one of the spots marked in the red dot array in (a). (c) Extracted A and B exciton peak amplitudes from (b). Yellow and green background colors correspond to the regions of metallic contacts and sample, respectively.

5.5 Material responses to the structured light

SAM-resolved photocurrent spectroscopy

Photocurrent spectra taken on a ML-MoS_2 FET under both the right circularly polarized (RCP) light and left circularly polarized light (LCP) for applied magnetic field between B = ±14 T perpendicular to ML-MoS_2 were shown in Figure 5.7. All spectra taken in different magnetic fields were fitted collectively to a Zeeman splitting model,[209,260,261] with the assumption that the PCS spectra for individual exciton modes near their resonance are Lorentzian.[46] The measured PCS current $I(B,\lambda)$ under magnetic field B and wavelength λ is thus described by the following equation:

$$I(B,\lambda) = \frac{\frac{|A_B|\pi \cdot w_B}{2}}{\left[\frac{hc}{\lambda} - \left(X_0^A + \frac{1}{2}\tau \cdot \mu_{Bohr} \cdot g \cdot B\right)\right]^2 + \left(\frac{w_B}{2}\right)^2}. \quad (1)$$

Here h is the Planck constant, c is the speed of light, μ_{Bohr} is the Bohr magneton, $\tau = \pm 1$ is the valley index corresponding to RCP and LCP, and A_B and w_B are the magnetic field-dependent Lorentzian amplitude and linewidth for each spectrum taken, respectively. Equation (1) also includes two magnetic field-independent parameters, where g is the Landé g-factor, and X_0^A is the central energy of the bright A-exciton peak under zero magnetic field. The normalized data (colored solid dots) and model fitting result for each magnetic field is shown as the colored dash line in Figure 5.11(a). The valley selection mechanism[244,262] allows a selective excitations of bright intra-valley A-excitons in the K (K′) valley using the RCP (LCP) light, showing a red (blue) shift in the corresponding A-excitonic energy with increasing magnetic fields. This is due to the magnetic field-induced Zeeman splitting in the K and K′-valleys, as illustrated in Figure 5.11(b). The fitted result showed that at zero magnetic field, the centers of the X_0^{A} was found to locate at 1.956 eV, shown as the vertical dark red dashed lines in Figure 5.11(a) for both RCP and LCP measurements, whereas the

g-factor was found to be -14.58 ± 0.61 and -11.14 ± 0.65 for RCP and LCP, respectively. Similar analysis was done for B exciton peak using RCP light and LP light, deriving g-factor of -14.61 ± 0.51 and -1.03 ± 0.60 respectively (Figure 5.12).

Here we remark that the magnitude of the g-factor derived from our PCS studies is significantly larger than that of the g-factor -4 derived from photoluminescence measurements,[263–265] which may be attributed to the existence of magnetic field-enhanced formation of intervalley excitons under the presence of an in-plane electric field. The notion of magnetic field-enhanced formation of intervalley excitons can be corroborated by our observation that the linewidth difference, defined as $(w_B^{RCP} - w_B^{LCP})$, was always positive for positive magnetic fields (*e.g.*, 21.5 meV at 12 T) and negative for negative magnetic fields (*e.g.*, -22.3 meV at -12 T), which implied that positive magnetic fields enhanced (suppressed) the formation of $\mathrm{K} \rightarrow \mathrm{K}'$ intervalley excitons under the excitation of RCP (LCP) light, as manifested by the energy diagrams in Figure 5.11(b), which resulted in the broadening (sharpening) of the linewidth w_B^{RCP} (w_B^{LCP}). Similarly, negative magnetic fields enhanced (suppressed) the formation of $\mathrm{K}' \rightarrow \mathrm{K}$ intervalley excitons under the excitation of LCP (RCP) light, thus resulting in the broadening (sharpening) of the linewidth $w_B^{LCP}(w_B^{RCP})$. It is worth pointing out that the g-factor values determined from our PCS studies were comparable to the intervalley exciton g-factor of -12 reported for monolayer tungsten diselenide.[266] Finally, we note that the slight difference between the g-factors extracted from the RCP and LCP measurements using our PCS may be due to in-plane bias voltage-induced valley symmetry breaking.

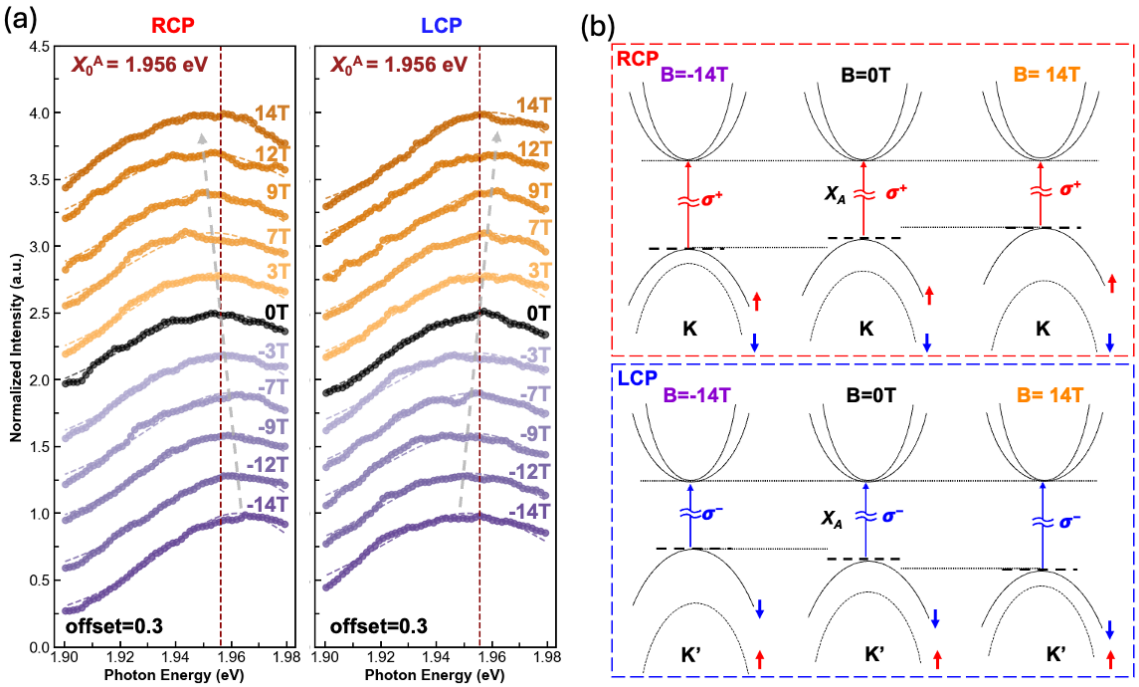

Figure 5.11 Application of the SAM/OAM-resolved PCS system to deriving the Landé g-factor of ML-MoS_2. (a) PCS of ML-MoS_2 FET between B = 0 and ±14 T under RCP light and LCP light, respectively. The colored dashed lines are fitting results under different magnetic field and the dark red vertical line indicates the fitted center of A exciton under zero magnetic field, X_0^A. The applied V_{DS} is 3 V and V_{GS} is 28V. The gray arrows serve as visual guides, indicating the shift of the peak center. (b) Energy band schematics of ML-MoS_2 under magnetic field with K (red) and K' (blue) valley respectively. The spin-orbit coupling at the conduction band minimum was small and thus omitted in the schematics.

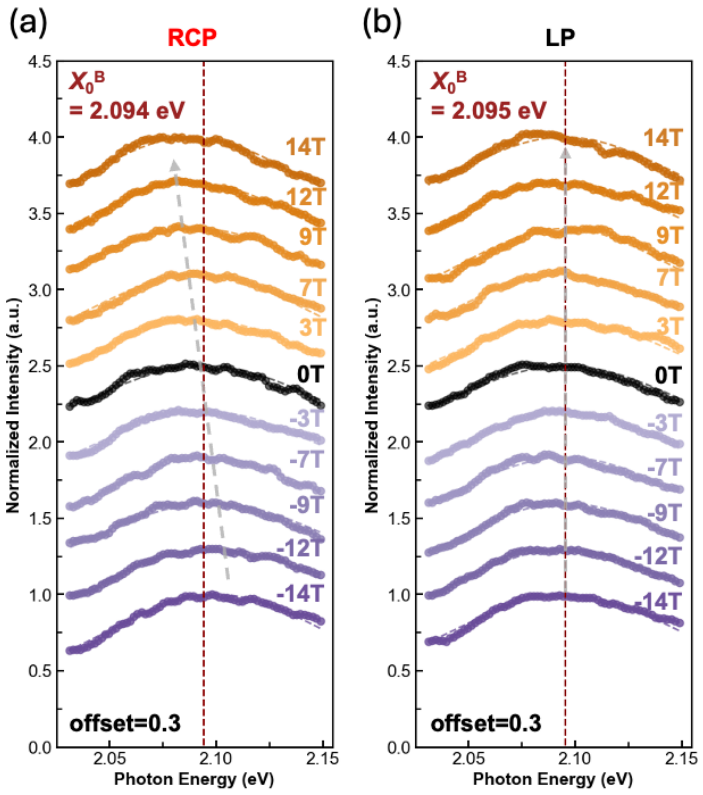

Figure 5.12 Additional data for deriving the Landé g-factor of ML-MoS_2. (a-b) PCS of ML-MoS_2 FET between B = 0 and ±14 T under RCP light and LP light, respectively. The colored dashed lines are fitting results under different magnetic field and the dark red vertical line indicates the fitted center of B exciton under zero magnetic field, X_0^B. The applied V_{DS} is 3 V and V_{GS} is 28V. The gray arrows serve as visual guides, indicating the shift of the peak center.

OAM-resolved photocurrent spectroscopy

In additional to studies of the SAM-resolved PCS, the effect of OAM light on the PCS of ML-MoS_2 was investigated and shown in Figure 5.13. We found that the measured photocurrent exhibited a significant increase with increasing $|\ell|$ for both positive [Figure 5.13(a)] and negative ℓ (Figure 5.13(b)), where the controlled $\ell = 0$ spectrum is shown in

black for reference in both plots. The extracted peak photocurrents on resonance with the bright A and B-excitons are shown in Figure 5.13(c), where up to ~ 80% enhancement in the photocurrent was observed for $\ell = \pm 5$ relative to that with $\ell = 0$. This unusual enhancement was not originated from larger effective spot size under higher ℓ because the channel length (~ 30 μm) well exceeded the spot size, and the moving the spot position over the sample region did not incur discernible changes in the measured photocurrent (Figure 5.13(c)). Moreover, the laser power variation under different ℓ values had been carefully calibrated to be less than ±3% (Figure 5.4(d)).

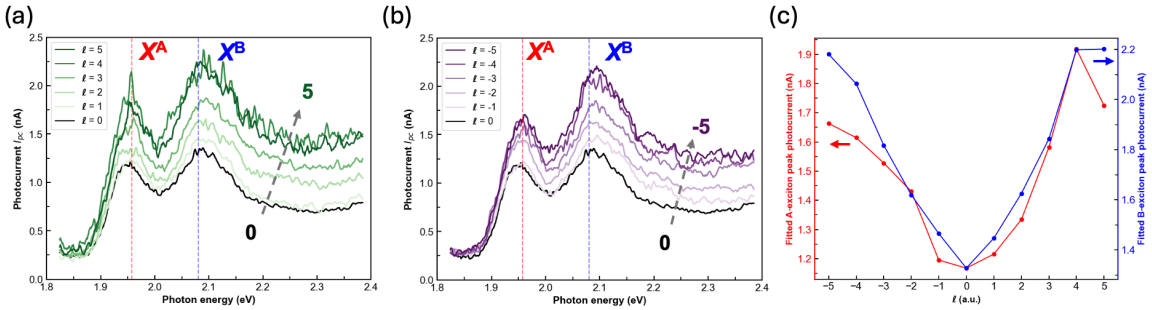

Figure 5.13 Orbital angular momentum enhanced photocurrent under linearly polarized light. (a, b) PCS obtained under OAM carrying ℓ from (a) 0 to 5 and (b) 0 to -5 with linearly polarized light. (c) Fitted A-exciton (red) and B-exciton (blue) peak photocurrents measured at their resonance energy under OAM light of different ℓ.

The substantial increase in photocurrents with increasing $|\ell|$ may be attributed to several important characteristics associated with the OAM light, that enables far more channels of excitations in materials relative to light without OAM, which include rapidly increasing accessible final states in the conduction bands due to the expanded "light cone"[267] with increasing $|\ell|$, unlocking phonon-assisted intervalley dark excitonic transitions,[266,268] enhancing the formation of Rydberg excitons,[269] and enabling quadrupole light-matter interactions in addition to the dipole interaction[269]. Moreover, the rapid increases of

measured photocurrent at ~2.14eV under light with increasing $|\ell|$ shows hints of strong excitation enhancement of Rydberg series of A excitons reported between 2.089 eV (A_{2s}) to 2.172 eV (A_{5s}) as shown in Figures 5.13(a) and 5.13(b) ,[46] although individual peaks of the Rydberg excitons could not be resolved from our current PCS measurements due to the limited signal-to-noise ratio and energy resolution, which may be improved in the future by encapsulating the ML-TMD FET devices with layers of h-BN to enhance the light-matter interaction.

Further observation of enhanced optoelectronic responses due to OAM light was manifested by an increased photoconductive effect measured with the lock-in technique (Figure 5.14(a)), where the light chopped at a finite frequency of 311Hz picked up the photoconductive response and rejected the DC photovoltaic effect[270]. Here we note that the DC photovoltaic effect was observed in the DC measurements (Figure 5.14(b) and 5.14(c)) and showed similar twisted light enhancement in previous study[271].

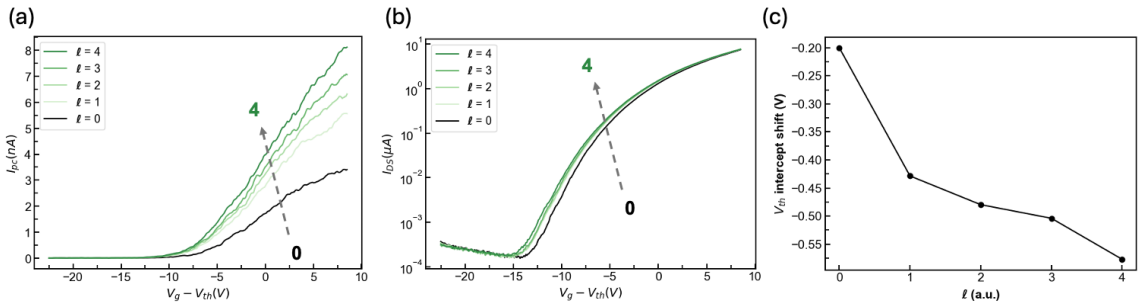

Figure 5.14 Orbital angular momentum enhanced photoconductive effect and photovoltaic effect. (a) AC photocurrent under OAM light of different ℓ. (b) Concurrently measured I_{DS}-*vs.*-V_g curve in semi-log scale measured under OAM light of different ℓ. (c) Extracted V_{th} shift as a function of different ℓ values from (b). All measurements were taken under λ =639.1 nm.

5.6 Conclusion

In this chapter, we reported a new instrumentation development of a cryogenic scanning photocurrent spectroscopy (PCS) system capable of resolving both spin and orbital angular momentum (SAM/OAM) of light for a spectral range from 500 nm (2.48 eV) to 700 nm (1.77 eV) and mapping a (35 × 25) μm^2 area with ~ 1 μm spatial resolution. We further demonstrated the capabilities of the instrument by applying it to investigate the optoelectronic responses of CVD-grown ML-MoS_2 FET devices at 3 K. We found that the SAM-resolved magneto-photocurrent measurement resulted in valley-dependent Zeeman splitting of the bright A-exciton peak, yielding a large Landé *g*-factor possibly due to magnetic field-enhanced intervalley excitons that were assisted by in-plane electric fields. Additionally, the OAM-resolved measurements revealed significant photocurrent enhancement with increasing $|\ell|$, which is consistent with substantially increased excitation channels associated with the OAM light. Further improvements of the signal-to-noise ratio for the PCS measurements may be achieved by encapsulating the ML-TMD FET device with finite thicknesses of hexagonal boron nitride (h-BN) to enhance the light-matter interaction and the magnitude of photocurrents so that the individual energies of dark and Rydberg excitons can be resolved. Additionally, the measurement uncertainty in laser power can be mitigated by using calibrated photodiodes with lock-in techniques to replace the standalone power meter. While there is clearly room for further improvements, the overall design concept of the instrument reported here provides a unique and versatile platform for investigating the optoelectronic responses of diverse quantum materials to structured SAM/OAM light.

Chapter 6

CONCLUSION AND OUTLOOK

This thesis presented experimental discoveries and investigations of various novel quantum phenomena that emerge at cryogenic temperature in nanoscale strain-engineered monolayer (ML)-graphene field-effect transistors (FETs) and valley Hall transistors, as well as in ML-MoS_2 FETs under external magnetic fields and/or structured light. Reliable ML-MoS_2 and ML-graphene synthesis techniques based on the chemical vapor deposition (CVD) and plasma enhanced chemical vapor deposition (PECVD) methods were employed to achieve scalable and reproducible high-quality samples, which were characterized by Raman spectroscopy, photoluminescence (PL) spectroscopy, x-ray photoelectron spectroscopy (XPS), atomic force microscopy (AFM), scanning electron microscopy (SEM), energy dispersive x-ray spectroscopy (EDS) and electrical transport measurements. State-of-the-art nanofabrication processes were developed to fabricate consistent ML-graphene valley Hall transistors and ML-MoS_2 FETs, with dedicated engineering efforts to incorporate processes that enabled the full scalability of the devices in the future. These fabricated devices revealed a variety of novel quantum phenomena, including strain-induced pseudo-magnetic fields (PMFs), quantum oscillations, quantum valley Hall effect and quantum anomalous Hall effects in ML-graphene; magnetic-field induced giant ferroelectric-like polar order in ML-MoS_2 FETs; and structured-light enhanced Landé *g*-factor and photocurrents in ML-MoS2 FETs. Additionally, cryogenic scanning photocurrent spectroscopy with structured light capabilities was designed and developed to study structured light-2D material interactions for temperatures from 2 K to 300 K and magnetic fields up to $\pm$14 T. This new and unique instrument provides new opportunities for studying and controlling the optoelectronic responses of 2D quantum materials under excitation of photons with finite spin angular momentum (SAM) and orbital angular momentum (OAM). These efforts in material

synthesis, device designs, fabrication and characterization and novel instrumentation development, provide exciting new pathways to the investigation and application of 2D quantum materials in the future.

In ML-graphene valley Hall transistors, the evidence of PMF-induced spin symmetry breaking observed in this thesis suggests strongly enhanced electronic correlations and calls for theoretical modeling to account for the enhanced spin-orbit coupling and spin-splitting in these highly strained devices. The pronounced anisotropy in these devices further necessitates anisotropic transport models to fully capture their nonlocal transport behavior. Moreover, other periodic nanostructures could be purposefully designed to investigate distinct quantum phenomena. For instance, periodic nano-steps could be employed to realize the Magnus Hall effect via a spatially periodic electrical potential modulated by the back gate and while the carrier density tuning may be achieved by using a top gate. Additionally, geometrically frustrated strain superlattices (*e.g.* triangular and Kagome lattice) in ML-graphene may further result in interesting topological characteristics induced by nanoscale strain engineering.

In the ML-MoS_2 FETs, we observed magnetic field-induced lattice asymmetric expansion, which was corroborated by the frozen in-plane phonons at cryogenic temperature, caused asymmetric rippling effect in ML-MoS_2 on rigid SiO_2/Si substrate. The asymmetric expansion led to mirror symmetry breaking, which gave rise to the giant out-of-plane ferroelectric-like polar order. This observation suggests two interesting research directions. 1) Similar effects may appear in other ML-TMD materials at cryogenic temperature over SiO_2/Si substrate, which may be detected using Raman spectroscopy or in a FET configuration similar to Chapter 4 with optimized electrical contacts that minimize the Schottky barrier can be achieved on other ML-TMD materials. 2) Other mechanisms that may introduce mirror-symmetry breaking in ML-MoS_2 and other ML-TMD systems may promote similar out-of-plane polar order. For instance, ML-TMDs placing over

nanostructures can induce asymmetric strain between the top and bottom sulfur layers, as shown in Figure 6.1 for ML-MoS_2 over a gold nanoparticle, where the top and the bottom sulfur layers exhibit opposite signs of strain tensor components. Therefore, the out-of-plane polar order may be achieved by using nanoscale architected substrates without needing an external magnetic field, which would be highly beneficial for realistic technological applications.

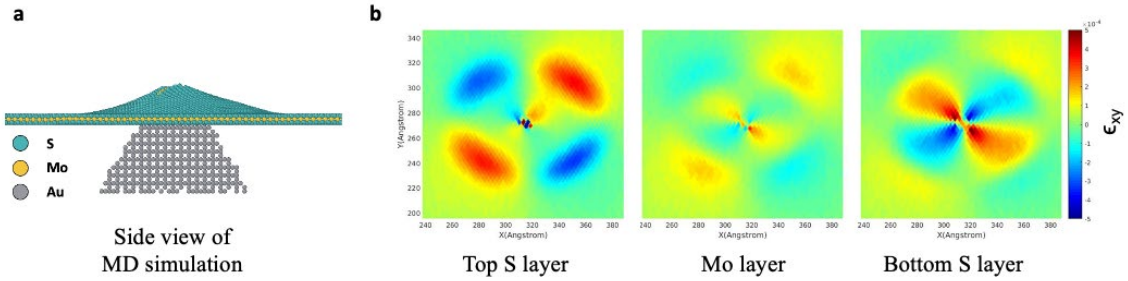

Figure 6.1 Molecular dynamics (MD) simulations of relaxing a $\sim 50\ nm \times 40\ nm$ ML-MoS_2 over a gold nano-tetrahedron particle with a side length of 1.46nm and a rounded tip curvature of 0.3 nm. (a) Sideview of the simulation final state. (b) Strain tensor component ϵ_{xy} in all three layers of a ML-MoS_2.

Furthermore, the strength of the polar order should be tunable by the carrier density, because the origin of the polar order is asymmetric charge distributions in the material, which may be reduced by electronic screening effects, as shown in Figure 6.2. Thus, the carrier density could be tuned electronically by tuning the back gate voltage as exemplified in Chapter 4, or optically by pumping with structured light. In fact, our preliminary studies have revealed that by optically pumping the FET with structured light of increasing OAM, the hysteresis window associated with the polar order steadily decreased generally reduced hysteresis window is observed, as exemplified in Figure 6.3. On the other hand, the photocurrent

steadily increased with increasing OAM, which was consistent with the results from the PCS studies outlined in Chapter 5 and may be attributed to the OAM light enhanced excitation channels in ML-MoS_2.

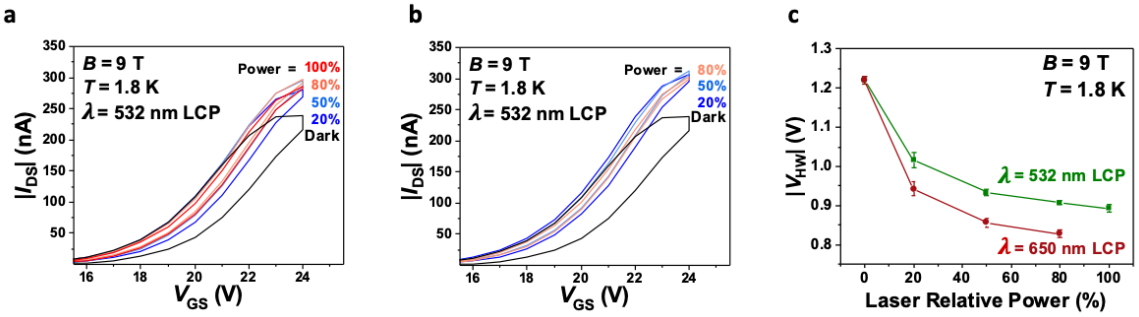

Figure 6.2 (a-b) $|I_{DS}|$-*vs.*-V_{GS} measurement under different laser power of (a) 532nm and (b) 650nm left circularly polarized light at B = 9 T and T =1.8 K. (c) Extracted $|V_{HW}|$ under different laser power and wavelength.

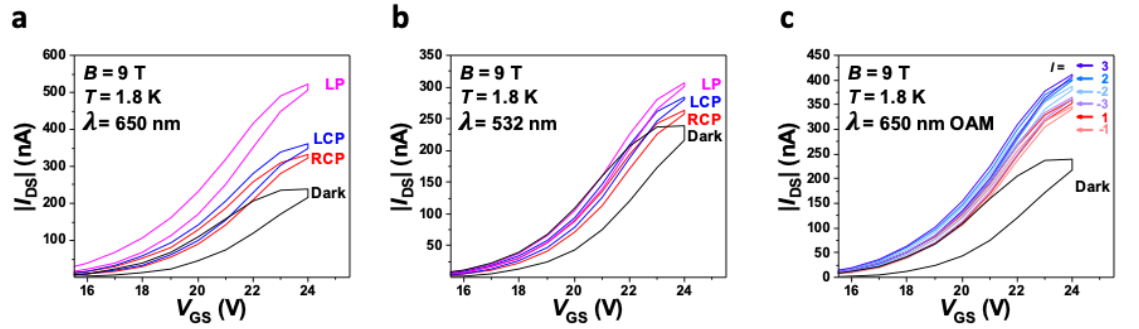

Figure 6.3 Preliminary data of structured light interaction with magnetic field-induced polar order at B = 9 T and T =1.8 K. (a-b) $|I_{DS}|$-*vs.*-V_{GS} measurement under different SAM using photon of (a) 650nm and (b) 532nm wavelength. (c) $|I_{DS}|$-*vs.*-V_{GS} measurement under different OAM with $\ell = \pm 1, \pm 2, \pm 3$.

Based on the aforementioned interesting findings, we expect that the interaction between structured light and strain-induced polar order in ML-TMD FETs (Figure 6.4) and valley Hall transistors may induce novel optoelectronic responses controlled by the sign and magnitude of the OAM of the optical excitations as well as the configurations of the strain superlattices with the help of the cryogenic scanning photocurrent spectroscopy developed in this thesis.

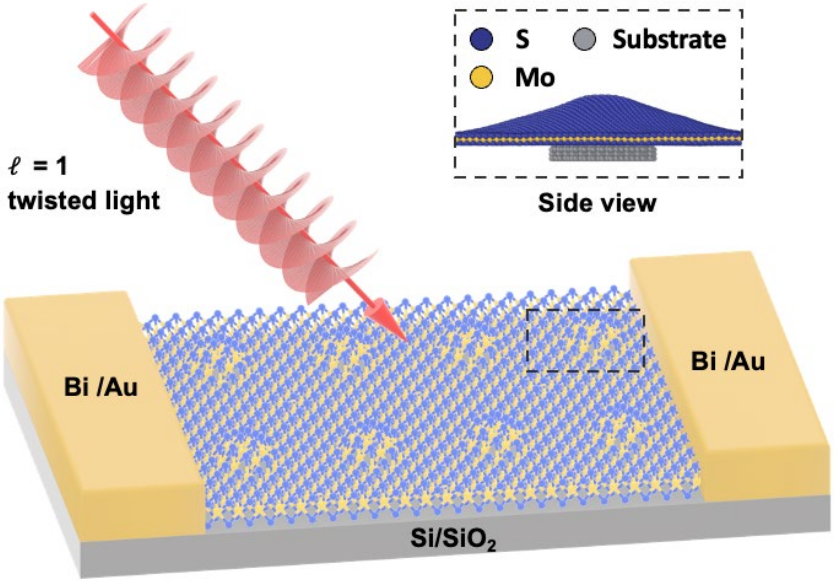

Figure 6.4 Concept illustration of studying structured light-strain-induced polar order interaction in a ML-MoS_2 FET with cryogenic photocurrent spectroscopy.

Appendix A

PPMS PUCK ASSEMBLY MAKING

1. Unscrew the set screw at the bottom of the PPMS universal sample puck (Quantum Design, 8084-100) and take apart the metal cap and the separable base (Figure A1(a)). Flip the separatable base upside-down such that the metal pads may be cleaned by using soldering braid.

2. Cut the wire into 1.5cm-long straight segments as shown in Figure A1 (b). Then use the razor blade to peel off the insulation coating 2.0mm on one end and 4mm on the other. Be as precise as possible to avoid short in later steps. Prepare 12 of them.

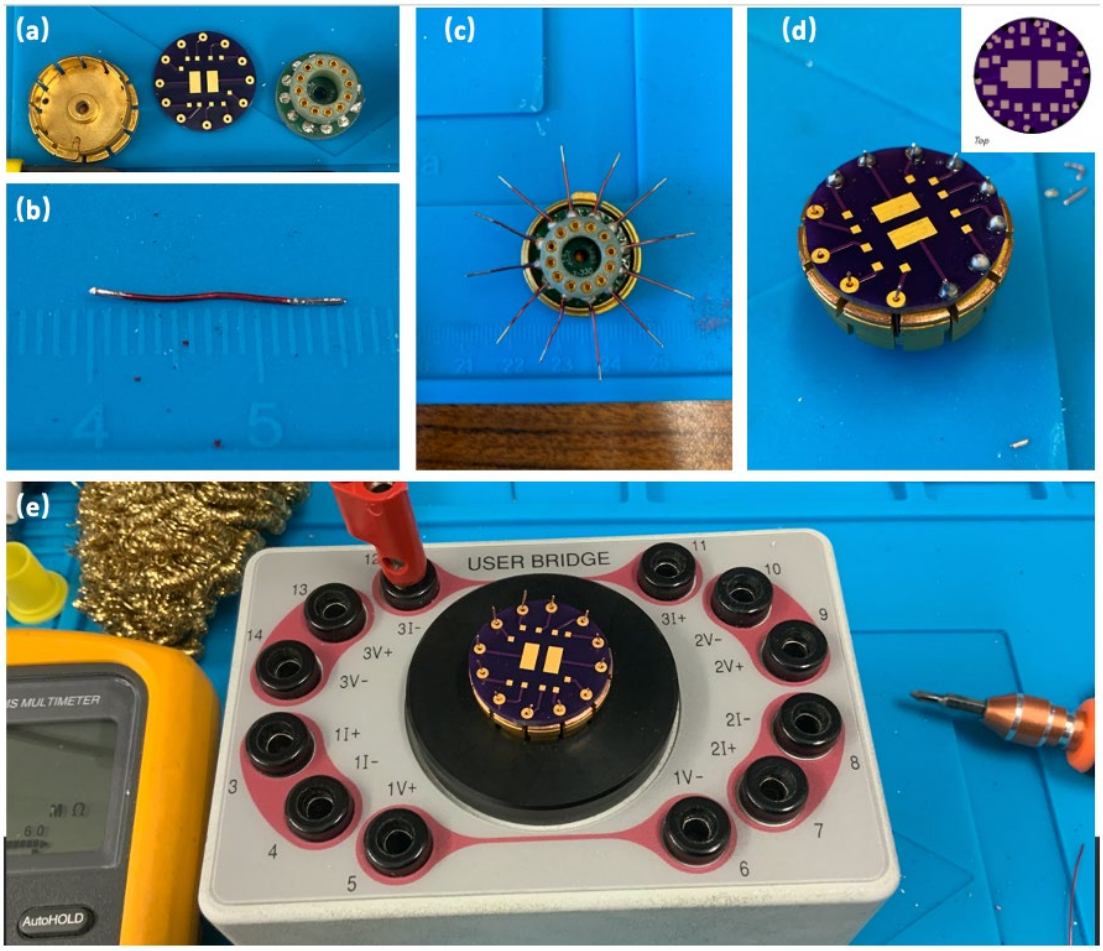

Figure A.1 PPMS puck assembly making. (a) (Left to right) PPMS puck metal cap, customized PCB board, PPMS puck separable base. (b) Typical razor-blade peeled wire. (c) Puck laid upside down after sliding the base into metal cap. (d) Puck in the final step of soldering. (e) Terminal connection testing using Quantum Design's user bridge and a Fluke 87 hand-held multimeter.

3. Apply solder to each pad and preheat it to form a smooth, hemispherical solder base. While the solder is heated, use tweezers to horizontally feed the 2.0 mm peeled end of the wire into the solder. Roughly aligned the wire such that it is in the direction of the metal pads. After this step, the 2.0mm-pealed end of the wire should be completely buried in the solder to avoid a possible short (Figure A1(c)).

4. Carefully slide the separable base into the metal cap. Re-solder some of the wire to correct wire's alignment if necessary. Use tweezer to tightly hold the other peeled end of the wire and bend it towards the puck cap. Put the wire through the pinhole on the PC board (Figure A1(d)). If a newer version of the PC board with additional test pads for wire-bonding is used (Figure A1(d) inset), only bring the wire close to the pad. Use a multimeter to test if any of the wire is short to the metal cap. If one did the 4.0mm peel-off precisely, there should be 0.3 mm ~ 1 mm insulating coat sitting above the metal cap's horizon.

5. With still 2mm-3mm wire extending and a few wires soldered, perform a loading check in the PPMS chamber. A smooth loading at this step is desired and if necessary, recenter the PC board accordingly.

6. Solder all other wires and trim off excessive wires. Use the user-bridge to measure and record the resistance between all terminals (Figure A.1(e)).

7. Use an ultrasonic cleaner to clean the puck in DI-water/Acetone/IPA for 15 mins each.

This appendix is temporarily embargoed.

Appendix C

SUPPLEMENTARY MATERIAL FOR CHAPTER 4

Discussion on various known hysteresis-inducing mechanisms

In this section, we aim to provide a phenomenological discussion of possible mechanisms that were previously identified in literature and were fundamentally different from the hysteresis behavior that we observed in the $|I_{DS}|$-*vs.*-V_{GS} transfer curves reported in Chapter 4 of this thesis.

Firstly, our findings differ drastically from previous reports of high-temperature and zero-B hysteretic behavior in monolayer MoS_2-FETs, which have been attributed to mechanisms such as thermally-activated extrinsic or intrinsic trapped states,[193–195] absorbates,[196,197] and gate voltage-induced stress effects,[198] where clockwise hysteresis loops were observed near room temperatures without magnetic field dependences. We have also observed a similar gate voltage stress type of clockwise hysteresis at higher temperature above T_C, as detailed in Figure 4.12. Firstly, our findings differ drastically from previous reports of high-temperature and zero-B hysteretic behavior in monolayer MoS_2-FETs, which have been attributed to mechanisms such as thermally-activated extrinsic or intrinsic trapped states,[193–195] absorbates,[196,197] and gate voltage-induced stress effects,[198] where clockwise hysteresis loops were observed near room temperatures without magnetic field dependences. We have also observed similar gate voltage stress type of clockwise hysteresis at higher temperature above T_C, as detailed in Figure 4.12.

At temperature below 4.2K, the presence of Schottky barrier between Cr/Au contact and MoS_2 can induce counterclockwise hysteresis in $|I_{DS}|$-*vs.*-V_{GS} transfer curves.[272] However, this type of hysteresis bears signature of a sharp rise in I_{DS} upon uncertain onset V_{GS} and the V_{HW} is larger with increasing V_{GS} sweep rates, contrary to our observations shown in

Figure 4.10. The Schottky barrier height in such devices is an result of a large Cr/Au contact barrier of ~ 200 meV,[272,273] whereas our devices shows negligible Schottky barrier height of ±20 meV as shown in the Figure 4.5(a). Furthermore, our devices exhibited no abruptly changing counterclockwise hysteresis behavior at B = 0. These contrasts all indicate that our magnetic field-induced counterclockwise hysteresis bears a different physical origin from the Schottky barrier mechanism. At temperature below 4.2K, the presence of Schottky barrier between Cr/Au contact and MoS_2 can induce counterclockwise hysteresis in $|I_{DS}|$-*vs.*-V_{GS} transfer curves.[272] However, this type of hysteresis bears signature of a sharp rise in I_{DS} upon uncertain onset V_{GS} and the V_{HW} is larger with increasing V_{GS} sweep rates, contrary to our observations shown in Figure 4.6. The Schottky barrier height in such devices is an result of a large Cr/Au contact barrier of ~ 200 meV,[272,273] whereas our devices show negligible Schottky barrier height of ±20 meV as shown in the Figure 4.5(a). Furthermore, our devices exhibited no abruptly changing counterclockwise hysteresis behavior at B = 0. These contrasts all indicate that our magnetic field-induced counterclockwise hysteresis bears different physical origin from the Schottky barrier mechanism.

Sulfur vacancies that exist in all MoS_2 FETs, as we discussed in the manuscript, could induce shallow donor-like trap states,[274] deep trap states above the valence band maximum,[274,275] or charge trapping at the oxide interfaces.[195,197] However, all of these would have led to magnetic field-independent clockwise hysteresis at relatively high temperatures, which contradicted our magnetic field-dependent counterclockwise hysteresis at cryo-temperatures. In-plane motion of sulfur vacancies or defects has been shown to introduce in-plane polar order with memristor-like behavior. For example, in-plane polar order had been observed as hysteresis in the I_{DS}-vs.-V_{DS} measurements under **in-plane** applied electric fields by introducing defects via focused ion beam,[276] chemical processing,[277] or utilizing Schottky barrier in contacts.[278] However, the scenario of ion or vacancy migration was incompatible with our observation for the following reasons: First,

the densities of sulfur vacancies in our devices were very low (~ 0.2% from KPFM and STM topography measurements, see Figures C.1-C.2) and no discernible magnetic impurities could be detected based on PL, Raman, and XPS mapping (Figures 4.1-4.2). Secondly, the magnetic field-induced polar order in our devices was modulated by **out-of-plane** electric fields (V_{GS}), which manifested hysteresis in the I_{DS}-*vs.*-V_{GS} measurements. In contrast, no discernable hysteresis could be found in the I_{DS}-vs.-V_{DS} measurements with **in-plane** electric fields (V_{DS}), which corroborated the notion of negligible ion or vacancy migration. Finally, interlayer motion of ions or vacancies would have been energetically too costly to occur in the monolayer system at low temperatures to yield out-of-plane polarization. Thus, we may rule out vacancy-induced trap states or ion/vacancy migration as the cause of our observed magnetic-field induced hysteresis at cryo-temperatures.

Flexoelectric effect could also manifest themselves as counterclockwise hysteresis as a result of strain gradient.[279] However, such polarization relies on the strain gradient that is non-switchable, thus is incompatible with our PFM results. Flexoelectric effect could also manifest themselves as counterclockwise hysteresis as a result of strain gradient.[279] However, such polarization relies on the strain gradient that is non-switchable, thus incompatible with our PFM results.

As for piezoelectric effect, it has been reported that the in-plane piezoelectric coefficient is much larger than the out-of-plane one,[279,280] and thus is less likely being the cause for our findings of V_{HW} that were mostly due to out-of-plane electric field and almost independent of the in-plane electric field. As for piezoelectric effect, it has been reported that the in-plane piezoelectric coefficient are much larger than the out-of-plane one,[279,280] thus less likely being the cause for our findings of V_{HW} that were mostly due to out-of-plane electric field and almost independent of the in-plane electric field.

In summary, we have ruled out all known mechanisms reported in the literature and thus demonstrate the novelty of our findings in magnetic field-induced hysteresis.

Characterization of sample sulfur vacancy concentrations

The sulfur vacancies in ML-MoS_2 may play an important role in our devices. Therefore, a typical FET device (Dev. #5), which we believed to possess representative sulfur vacancy concentrations, was studied using Kelvin probe force microscopy (KPFM), as shown in Figure B.1. We also presented in Figure B.2 direct surface topography imaging of one ML-MoS_2 sample by STM, which revealed a sulfur vacancy level similar to the low density of sulfur vacancies ~0.2% (Dev. #1-5) found in the ML-MoS_2 FET devices. The details are as follows.

The work function of the ML-MoS_2 was measured by the Peak Force Kelvin Probe Force Microscopy (PF-KPFM) calibrated with respect to the work function of gold at 4.82 eV. The contact potential difference (CPD) between the tip and the sample is given by $\Delta V_{CPD} = \phi_{sample} - \phi_{tip}$, where ϕ is the work function. Therefore, the work function of the ML-MoS_2 sample becomes

$$\phi_{MoS_2} = \phi_{tip} + \Delta V_{CPD}^{MoS_2} = \phi_{Au} + \Delta V_{CPD}^{MoS_2} - \Delta V_{CPD}^{Au}, \quad (C.1)$$

where $\Delta V_{CPD}^{MoS_2}$ was measured to be 0.52 ± 0.23 V, while ΔV_{CPD}^{Au} was measured to be 0.39 ± 0.22 V in a scan size of (1 μm × 1 μm, 512*512 grid) area on the fabricated Device #5. The Fermi level E_F is therefore determined from $\phi_{MoS_2} \sim 4.9$eV, which is located 0.4 eV above at the intrinsic Fermi level (E_i) of ML-MoS_2, as shown in the Figure A.1. Here we note that approximation of E_i can be expressed as $E_i = (E_c + E_v + k_B T \ln(m_p^*/m_n^*))/2 \approx (E_c + E_v)/2$, where m_p^* and m_n^* are the effective mass of holes and electrons of MoS_2, respectively, and the $k_B T \ln(m_p^*/m_n^*)$ term is negligible compared to $(E_c + E_v)$. The electron concentration of MoS_2 could be calculated with the following formula,

$$n = n_i \exp\left(\frac{E_F - E_I}{k_B T}\right), \quad (C.2)$$

where k_B is Boltzmann constant, T is the temperature, and n_i is the intrinsic electron concentration of MoS_2. With $n_i \sim 10^6$ cm^{-2} at room temperature[281] and measured $E_F - E_i$ = 0.4 eV, the corresponding electron concentration of the MoS_2 sample was estimated as $n \approx 4.8\times10^{12}$ cm^{-2}. Assuming those electrons were induced by sulfur vacancies, the order of magnitude of sulfur vacancy population density can be estimated as $na^2\sqrt{3}/4 \sim 0.2\%$, where a = 0.318 nm is the lattice constant of MoS_2. With $n_i \sim 10^6$ cm^{-2} at room temperature[281] and measured $E_F - E_i$ = 0.4 eV, the corresponding electron concentration of the MoS_2 sample was estimated as $n \approx 4.8\times10^{12}$ cm^{-2}. Assuming those electrons were induced by sulfur vacancies, the order of magnitude of sulfur vacancy population density can be estimated as $na^2\sqrt{3}/4 \sim 0.2\%$, where a = 0.318 nm is the lattice constant of MoS_2.

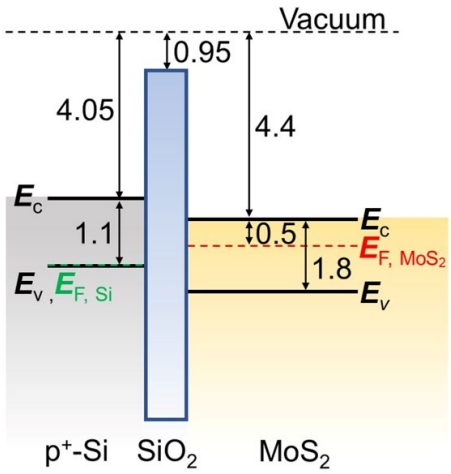

Figure C.1 Schematic of the band alignment of $MoS_2/SiO_2/Si$ based on KPFM measurement for device #5.

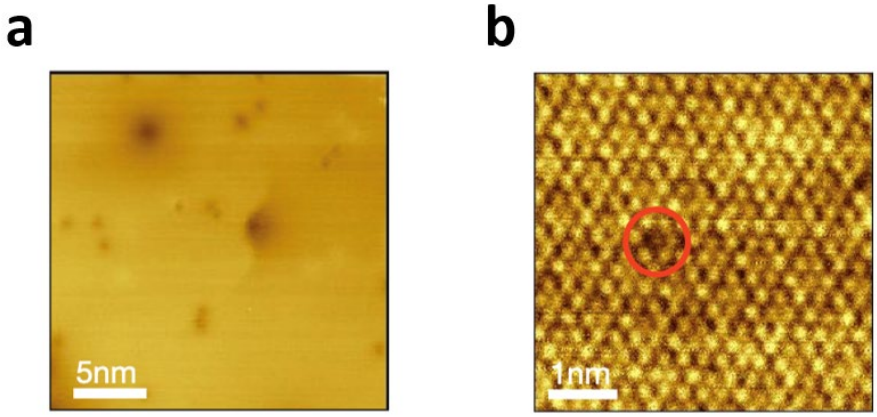

Figure C.2 STM topography of typical sulfur vacancies on MoS_2. (a) Surface topography (20 nm × 20 nm) with bias voltage −1 V, tunneling current 2.0 nA, and $B = 0$, where the defect density is 5.0 × 1012 cm-2. (b) One instance of a sulfur vacancy marked by red circle observed under $B = 5$ T at 4.5 K with bias voltage of –0.4V and tunneling current of 2.0 nA.

BILIOGRAPHY

1. Fiori, G. *et al.* Electronics based on two-dimensional materials. *Nature Nanotech* **9**, 768–779 (2014).
2. Xia, F., Wang, H., Xiao, D., Dubey, M. & Ramasubramaniam, A. Two-dimensional material nanophotonics. *Nature Photon* **8**, 899–907 (2014).
3. Das, S. *et al.* Transistors based on two-dimensional materials for future integrated circuits. *Nat Electron* **4**, 786–799 (2021).
4. Schwierz, F., Pezoldt, J. & Granzner, R. Two-dimensional materials and their prospects in transistor electronics. *Nanoscale* **7**, 8261–8283 (2015).
5. Guan, Z. *et al.* Recent Progress in Two-Dimensional Ferroelectric Materials. *Advanced Electronic Materials* **6**, 1900818 (2020).
6. Cao, Y. *et al.* Unconventional superconductivity in magic-angle graphene superlattices. *Nature* **556**, 43–50 (2018).
7. Taghizadeh, A. & Pedersen, T. G. Nonlinear optical selection rules of excitons in monolayer transition metal dichalcogenides. *Phys. Rev. B* **99**, 235433 (2019).
8. Novoselov, K. S. *et al.* Electric Field Effect in Atomically Thin Carbon Films. *Science* **306**, 666–669 (2004).
9. Gusynin, V. P. & Sharapov, S. G. Unconventional Integer Quantum Hall Effect in Graphene. *Phys. Rev. Lett.* **95**, 146801 (2005).
10. Jiang, Z., Zhang, Y., Tan, Y.-W., Stormer, H. L. & Kim, P. Quantum Hall effect in graphene. *Solid State Communications* **143**, 14–19 (2007).
11. Bolotin, K. I., Ghahari, F., Shulman, M. D., Stormer, H. L. & Kim, P. Observation of the fractional quantum Hall effect in graphene. *Nature* **462**, 196–199 (2009).
12. Yamamoto, M., Shimazaki, Y., Borzenets, I. V. & Tarucha, S. Valley Hall Effect in Two-Dimensional Hexagonal Lattices. *J. Phys. Soc. Jpn.* **84**, 121006 (2015).
13. Castro Neto, A. H. The electronic properties of graphene. *Rev. Mod. Phys.* **81**, 109–162 (2009).
14. Wallace, P. R. The Band Theory of Graphite. *Phys. Rev.* **71**, 622–634 (1947).
15. Reich, S., Maultzsch, J., Thomsen, C. & Ordejón, P. Tight-binding description of graphene. *Phys. Rev. B* **66**, 035412 (2002).
16. Saito, R., Dresselhaus, G. & Dresselhaus, M. S. *Physical Properties of Carbon Nanotubes*. (PUBLISHED BY IMPERIAL COLLEGE PRESS and DISTRIBUTED BY WORLD SCIENTIFIC PUBLISHING CO., 1998). doi:10.1142/p080.
17. Laturia, A., Van De Put, M. L. & Vandenberghe, W. G. Dielectric properties of hexagonal boron nitride and transition metal dichalcogenides: from monolayer to bulk. *npj 2D Mater Appl* **2**, 6 (2018).
18. Xia, J., Chen, F., Li, J. & Tao, N. Measurement of the quantum capacitance of graphene. *Nature Nanotech* **4**, 505–509 (2009).

19. Dröscher, S. *et al.* Quantum capacitance and density of states of graphene. *Applied Physics Letters* **96**, 152104 (2010).
20. Gosling, J. H. *et al.* Universal mobility characteristics of graphene originating from charge scattering by ionised impurities. *Commun Phys* **4**, 30 (2021).
21. Zheng, Y. & Ando, T. Hall conductivity of a two-dimensional graphite system. *Phys. Rev. B* **65**, 245420 (2002).
22. Manzeli, S., Ovchinnikov, D., Pasquier, D., Yazyev, O. V. & Kis, A. 2D transition metal dichalcogenides. *Nat Rev Mater* **2**, 17033 (2017).
23. Han, G. H., Duong, D. L., Keum, D. H., Yun, S. J. & Lee, Y. H. van der Waals Metallic Transition Metal Dichalcogenides. *Chem. Rev.* **118**, 6297–6336 (2018).
24. Zhao, W. *et al.* Metastable MoS_2 : Crystal Structure, Electronic Band Structure, Synthetic Approach and Intriguing Physical Properties. *Chemistry A European J* **24**, 15942–15954 (2018).
25. Shirodkar, S. N. & Waghmare, U. V. Emergence of Ferroelectricity at a Metal-Semiconductor Transition in a 1 T Monolayer of MoS 2. *Phys. Rev. Lett.* **112**, 157601 (2014).
26. Lu, H. *et al.* Unraveling Piezoelectricity of Two-Dimensional Ferroelectric Metal 1T″-MoS_2. *ACS Materials Lett.* **5**, 3136–3141 (2023).
27. Liu, L. *et al.* Phase-selective synthesis of 1T′ MoS2 monolayers and heterophase bilayers. *Nature Mater* **17**, 1108–1114 (2018).
28. Zhang, R. *et al.* Superconductivity in Potassium-Doped Metallic Polymorphs of MoS2. *Nano Lett.* **16**, 629–636 (2016).
29. Zhao, W. *et al.* Metastable MoS_2 : Crystal Structure, Electronic Band Structure, Synthetic Approach and Intriguing Physical Properties. *Chemistry A European J* **24**, 15942–15954 (2018).
30. Wei, L., Jun-fang, C., Qinyu, H. & Teng, W. Electronic and elastic properties of MoS2. *Physica B: Condensed Matter* **405**, 2498–2502 (2010).
31. Kumar, A. & Ahluwalia, P. K. A first principle Comparative study of electronic and optical properties of 1H – MoS2 and 2H – MoS2. *Materials Chemistry and Physics* **135**, 755–761 (2012).
32. Splendiani, A. *et al.* Emerging Photoluminescence in Monolayer MoS_2. *Nano Lett.* **10**, 1271–1275 (2010).
33. Liu, G.-B., Shan, W.-Y., Yao, Y., Yao, W. & Xiao, D. Three-band tight-binding model for monolayers of group-VIB transition metal dichalcogenides. *Phys. Rev. B* **88**, 085433 (2013).
34. Wu, F., Qu, F. & MacDonald, A. H. Exciton band structure of monolayer MoS 2. *Phys. Rev. B* **91**, 075310 (2015).
35. Shahriari, M., Ghalambor Dezfuli, A. & Sabaeian, M. Band structure and orbital character of monolayer MoS2 with eleven-band tight-binding model. *Superlattices and Microstructures* **114**, 169–182 (2018).

36. Wu, F., Qu, F. & MacDonald, A. H. Exciton band structure of monolayer MoS 2. *Phys. Rev. B* **91**, 075310 (2015).
37. Liu, G.-B., Shan, W.-Y., Yao, Y., Yao, W. & Xiao, D. Three-band tight-binding model for monolayers of group-VIB transition metal dichalcogenides. *Phys. Rev. B* **88**, 085433 (2013).
38. Giannozzi, P. *et al.* QUANTUM ESPRESSO: a modular and open-source software project for quantum simulations of materials. *J. Phys.: Condens. Matter* **21**, 395502 (2009).
39. Xiao, D., Liu, G.-B., Feng, W., Xu, X. & Yao, W. Coupled Spin and Valley Physics in Monolayers of MoS 2 and Other Group-VI Dichalcogenides. *Phys. Rev. Lett.* **108**, 196802 (2012).
40. Zhu, C. R. *et al.* Exciton valley dynamics probed by Kerr rotation in ${\mathrm{WSe}}_{2}$ monolayers. *Phys. Rev. B* **90**, 161302 (2014).
41. Chernikov, A. *et al.* Exciton Binding Energy and Nonhydrogenic Rydberg Series in Monolayer ${\mathrm{WS}}_{2}$. *Phys. Rev. Lett.* **113**, 076802 (2014).
42. Mak, K. F., He, K., Shan, J. & Heinz, T. F. Control of valley polarization in monolayer MoS2 by optical helicity. *Nature Nanotechnology* **7**, 494–498 (2012).
43. Zhang, C., Johnson, A., Hsu, C.-L., Li, L.-J. & Shih, C.-K. Direct Imaging of Band Profile in Single Layer MoS_2 on Graphite: Quasiparticle Energy Gap, Metallic Edge States, and Edge Band Bending. *Nano Lett.* **14**, 2443–2447 (2014).
44. Zhang, C., Wang, H., Chan, W., Manolatou, C. & Rana, F. Absorption of light by excitons and trions in monolayers of metal dichalcogenide Mo S 2 : Experiments and theory. *Phys. Rev. B* **89**, 205436 (2014).
45. Mak, K. F. *et al.* Tightly bound trions in monolayer MoS2. *Nature Mater* **12**, 207–211 (2013).
46. Vaquero, D. *et al.* Excitons, trions and Rydberg states in monolayer MoS2 revealed by low-temperature photocurrent spectroscopy. *Commun Phys* **3**, 194 (2020).
47. Vaquero, D. *et al.* Excitons, trions and Rydberg states in monolayer MoS2 revealed by low-temperature photocurrent spectroscopy. *Commun Phys* **3**, 1–8 (2020).
48. Cao, T. *et al.* Valley-selective circular dichroism of monolayer molybdenum disulphide. *Nature Communications* **3**, (2012).
49. Molas, M. R. *et al.* Brightening of dark excitons in monolayers of semiconducting transition metal dichalcogenides. *2D Mater.* **4**, 021003 (2017).
50. Robert, C. *et al.* Measurement of the spin-forbidden dark excitons in MoS2 and MoSe2 monolayers. *Nat Commun* **11**, 4037 (2020).
51. Yu, T. & Wu, M. W. Valley depolarization dynamics and valley Hall effect of excitons in monolayer and bilayer MoS 2. *Phys. Rev. B* **93**, 045414 (2016).
52. Saraswat, R., Verma, R. & Bhattacharya, S. Strain-Induced Activation of Symmetry-Forbidden Exciton-Phonon Couplings for Enhanced Phonon-Assisted Photoluminescence in MoS$_2$ Monolayers. Preprint at https://doi.org/10.48550/arXiv.2501.01410 (2025).

53. Rubinsztein-Dunlop, H. *et al.* Roadmap on structured light. *J. Opt.* **19**, 013001 (2017).
54. Willner, A. E. *et al.* Optical communications using orbital angular momentum beams. *Adv. Opt. Photon.* **7**, 66 (2015).
55. Polimeno, P. *et al.* Optical tweezers and their applications. *Journal of Quantitative Spectroscopy and Radiative Transfer* **218**, 131–150 (2018).
56. Moffitt, J. R., Chemla, Y. R., Smith, S. B. & Bustamante, C. Recent Advances in Optical Tweezers. *Annu. Rev. Biochem.* **77**, 205–228 (2008).
57. Porfirev, A., Khonina, S. & Kuchmizhak, A. Light–matter interaction empowered by orbital angular momentum: Control of matter at the micro- and nanoscale. *Progress in Quantum Electronics* **88**, 100459 (2023).
58. Rong, R. *et al.* The Interaction of 2D Materials With Circularly Polarized Light. *Advanced Science* **10**, 2206191 (2023).
59. Yariv, A. *Introduction to Optical Electronics*. (Holt, Rinehart and Winston, Inc.,New York, NY, United States, 1976).
60. *Quantum Imaging*. (Springer, New York, 2007).
61. Tamm, C. & Weiss, C. O. Bistability and optical switching of spatial patterns in a laser.
62. Tamm, Chr. Frequency locking of two transverse optical modes of a laser. *Phys. Rev. A* **38**, 5960–5963 (1988).
63. Sroor, H. *et al.* High-purity orbital angular momentum states from a visible metasurface laser. *Nat. Photonics* **14**, 498–503 (2020).
64. Wang, W. *et al.* Ultra-thin optical vortex phase plate based on the metasurface and the angular momentum transformation. *J. Opt.* **17**, 045102 (2015).
65. Zhao, Z. High precision optical Wavefront generation using liquid crystal spatial light modulator (LC-SLM). in *Liquid crystals* (IntechOpen, 2021).
66. Naidoo, D. *et al.* Controlled generation of higher-order Poincaré sphere beams from a laser. *Nature Photon* **10**, 327–332 (2016).
67. He, H., Friese, M. E. J., Heckenberg, N. R. & Rubinsztein-Dunlop, H. Direct Observation of Transfer of Angular Momentum to Absorptive Particles from a Laser Beam with a Phase Singularity. *Phys. Rev. Lett.* **75**, 826–829 (1995).
68. Wätzel, J. & Berakdar, J. Centrifugal photovoltaic and photogalvanic effects driven by structured light. *Sci Rep* **6**, 21475 (2016).
69. Wätzel, J. & Berakdar, J. Centrifugal photovoltaic and photogalvanic effects driven by structured light. *Sci Rep* **6**, 21475 (2016).
70. Simbulan, K. B. *et al.* Twisted Light-Enhanced Photovoltaic Effect. *ACS Nano* **15**, 14822–14829 (2021).
71. Simbulan, K. B. *et al.* Selective Photoexcitation of Finite-Momentum Excitons in Monolayer MoS_2 by Twisted Light. *ACS Nano* **15**, 3481–3489 (2021).
72. Quinteiro, G. F. & Tamborenea, P. I. Theory of the optical absorption of light carrying orbital angular momentum by semiconductors. *Europhys. Lett.* **85**, 47001 (2009).

73. Schmiegelow, C. T. & Schmidt-Kaler, F. Light with orbital angular momentum interacting with trapped ions. *Eur. Phys. J. D* **66**, 157 (2012).
74. Schmiegelow, C. T. *et al.* Transfer of optical orbital angular momentum to a bound electron. *Nat Commun* **7**, 12998 (2016).
75. Sordillo, L. A., Mamani, S., Sharonov, M. & Alfano, R. R. The interaction of twisted Laguerre-Gaussian light with a GaAs photocathode to investigate photogenerated polarized electrons. *Applied Physics Letters* **114**, 041104 (2019).
76. Lu, C.-H., Hao, D. & Yeh, N.-C. A perspective of recent advances in PECVD-grown graphene thin films for scientific research and technological applications. *Materials Chemistry and Physics* **319**, 129318 (2024).
77. Choi, S. H. *et al.* Large-scale synthesis of graphene and other 2D materials towards industrialization. *Nat Commun* **13**, 1484 (2022).
78. Briggs, N. *et al.* A roadmap for electronic grade 2D materials. *2D Mater.* **6**, 022001 (2019).
79. Yang, Z. & Hao, J. Progress in pulsed laser deposited two-dimensional layered materials for device applications. *J. Mater. Chem. C* **4**, 8859–8878 (2016).
80. Vishwanath, S. *et al.* MBE growth of few-layer 2H-MoTe2 on 3D substrates. *Journal of Crystal Growth* **482**, 61–69 (2018).
81. Vishwanath, S. *et al.* Comprehensive structural and optical characterization of MBE grown $MoSe_2$ on graphite, CaF_2 and graphene. *2D Mater.* **2**, 024007 (2015).
82. Cai, J., Han, X., Wang, X. & Meng, X. Atomic Layer Deposition of Two-Dimensional Layered Materials: Processes, Growth Mechanisms, and Characteristics. *Matter* **2**, 587–630 (2020).
83. Hao, W., Marichy, C. & Journet, C. Atomic layer deposition of stable 2D materials. *2D Mater.* **6**, 012001 (2018).
84. Kim, H. G. & Lee, H.-B.-R. Atomic Layer Deposition on 2D Materials. *Chem. Mater.* **29**, 3809–3826 (2017).
85. Shen, P.-C. *et al.* CVD Technology for 2-D Materials. *IEEE Trans. Electron Devices* **65**, 4040–4052 (2018).
86. Yi, K. *et al.* Plasma-Enhanced Chemical Vapor Deposition of Two-Dimensional Materials for Applications. *Acc. Chem. Res.* **54**, 1011–1022 (2021).
87. Vizireanu, S., Mitu, B., Luculescu, C. R., Nistor, L. C. & Dinescu, G. PECVD synthesis of 2D nanostructured carbon material. *Surface and Coatings Technology* **211**, 2–8 (2012).
88. Lei, M. *et al.* Low-temperature chemical vapor deposition growth of 2D materials. *Electron* **3**, e43 (2025).
89. Xu, X. *et al.* Growth of 2D Materials at the Wafer Scale. *Advanced Materials* **34**, 2108258 (2022).
90. Kim, T. *et al.* Wafer-Scale Epitaxial 1T′, 1T′–2H Mixed, and 2H Phases MoTe2 Thin Films Grown by Metal–Organic Chemical Vapor Deposition. *Advanced Materials Interfaces* **5**, 1800439 (2018).

91. Bolotin, K. I., Ghahari, F., Shulman, M. D., Stormer, H. L. & Kim, P. Observation of the fractional quantum Hall effect in graphene. *Nature* **462**, 196–199 (2009).
92. Cao, Y. *et al.* Unconventional superconductivity in magic-angle graphene superlattices. *Nature* **556**, 43–50 (2018).
93. Zheng, Z. *et al.* Unconventional ferroelectricity in moiré heterostructures. *Nature* **588**, 71–76 (2020).
94. Boyd, D. A. *et al.* Single-step deposition of high-mobility graphene at reduced temperatures. *Nat Commun* **6**, 6620 (2015).
95. Yeh, N.-C., Hsu, C.-C., Bagley, J. & Tseng, W.-S. Single-step growth of graphene and graphene-based nanostructures by plasma-enhanced chemical vapor deposition. *Nanotechnology* **30**, 162001 (2019).
96. Cuxart, M. G. *et al.* Inductively coupled remote plasma-enhanced chemical vapor deposition (rPE-CVD) as a versatile route for the deposition of graphene micro- and nanostructures. *Carbon* **117**, 331–342 (2017).
97. Boyd, D. A. *et al.* Single-step deposition of high-mobility graphene at reduced temperatures. *Nat Commun* **6**, 6620 (2015).
98. Cai, Z., Liu, B., Zou, X. & Cheng, H.-M. Chemical Vapor Deposition Growth and Applications of Two-Dimensional Materials and Their Heterostructures. *Chem. Rev.* **118**, 6091–6133 (2018).
99. Chen, Z., Qi, Y., Chen, X., Zhang, Y. & Liu, Z. Direct CVD Growth of Graphene on Traditional Glass: Methods and Mechanisms. *Advanced Materials* **31**, 1803639 (2019).
100. Lee, Y.-H. *et al.* Synthesis of Large-Area MoS2 Atomic Layers with Chemical Vapor Deposition. *Advanced Materials* **24**, 2320–2325 (2012).
101. Zhan, Y., Liu, Z., Najmaei, S., Ajayan, P. M. & Lou, J. Large-Area Vapor-Phase Growth and Characterization of MoS2 Atomic Layers on a SiO2 Substrate. *Small* **8**, 966–971 (2012).
102. Simbulan, K. B. C., Chen, P.-C., Lin, Y.-Y. & Lan, Y.-W. A Standard and Reliable Method to Fabricate Two-Dimensional Nanoelectronics. *JoVE* 57885 (2018) doi:10.3791/57885.
103. Teague, M. L. *et al.* Evidence for Strain-Induced Local Conductance Modulations in Single-Layer Graphene on SiO2. *Nano Lett.* **9**, 2542–2546 (2009).
104. Guinea, F., Katsnelson, M. I. & Vozmediano, M. A. H. Midgap states and charge inhomogeneities in corrugated graphene. *Phys. Rev. B* **77**, 075422 (2008).
105. Mañes, J. L. Symmetry-based approach to electron-phonon interactions in graphene. *Phys. Rev. B* **76**, 045430 (2007).
106. Guinea, F., Katsnelson, M. I. & Geim, A. K. Energy gaps and a zero-field quantum Hall effect in graphene by strain engineering. *Nature Phys* **6**, 30–33 (2010).
107. Levy, N. *et al.* Strain-Induced Pseudo–Magnetic Fields Greater Than 300 Tesla in Graphene Nanobubbles. *Science* **329**, 544–547 (2010).
108. Yeh, N.-C. *et al.* Nano-scale strain engineering of graphene and graphene-based devices. *Acta Mech. Sin.* **32**, 497–509 (2016).

109. Hsu, C.-C., Teague, M. L., Wang, J.-Q. & Yeh, N.-C. Nanoscale strain engineering of giant pseudo-magnetic fields, valley polarization, and topological channels in graphene. *Sci. Adv.* **6**, eaat9488 (2020).
110. Guinea, F., Geim, A. K., Katsnelson, M. I. & Novoselov, K. S. Generating quantizing pseudomagnetic fields by bending graphene ribbons. *Phys. Rev. B* **81**, 035408 (2010).
111. Yeh, N.-C. *et al.* Strain-induced pseudo-magnetic fields and charging effects on CVD-grown graphene. *Surface Science* **605**, 1649–1656 (2011).
112. Lee, D. S. *et al.* Raman Spectra of Epitaxial Graphene on SiC and of Epitaxial Graphene Transferred to SiO_2. *Nano Lett.* **8**, 4320–4325 (2008).
113. Sutter, P., Sadowski, J. T. & Sutter, E. Graphene on Pt(111): Growth and substrate interaction. *Phys. Rev. B* **80**, 245411 (2009).
114. Zhang, K. & Arroyo, M. Understanding and strain-engineering wrinkle networks in supported graphene through simulations. *Journal of the Mechanics and Physics of Solids* **72**, 61–74 (2014).
115. Shioya, H., Craciun, M. F., Russo, S., Yamamoto, M. & Tarucha, S. Straining Graphene Using Thin Film Shrinkage Methods. *Nano Lett.* **14**, 1158–1163 (2014).
116. Shioya, H., Russo, S., Yamamoto, M., Craciun, M. F. & Tarucha, S. Electron States of Uniaxially Strained Graphene. *Nano Lett.* **15**, 7943–7948 (2015).
117. Katin, K. P., Prudkovskiy, V. S. & Maslov, M. M. Molecular dynamics simulation of nickel-coated graphene bending. *Micro & Nano Letters* **13**, 160–164 (2018).
118. Yu, T. *et al.* Raman Mapping Investigation of Graphene on Transparent Flexible Substrate: The Strain Effect. *J. Phys. Chem. C* **112**, 12602–12605 (2008).
119. Ni, Z. H. *et al.* Uniaxial Strain on Graphene: Raman Spectroscopy Study and Band-Gap Opening. *ACS Nano* **2**, 2301–2305 (2008).
120. Mohiuddin, T. M. G. *et al.* Uniaxial strain in graphene by Raman spectroscopy: G peak splitting, Grüneisen parameters, and sample orientation. *Phys. Rev. B* **79**, 205433 (2009).
121. Petrone, N., Meric, I., Hone, J. & Shepard, K. L. Graphene Field-Effect Transistors with Gigahertz-Frequency Power Gain on Flexible Substrates. *Nano Lett.* **13**, 121–125 (2013).
122. Xu, C. *et al.* An experimental investigation on the mechanical properties of the interface between large-sized graphene and a flexible substrate. *Journal of Applied Physics* **117**, 164301 (2015).
123. Jin, Y. *et al.* Stretching Graphene to 3.3% Strain Using Formvar-Reinforced Flexible Substrate. *Exp Mech* **62**, 761–767 (2022).
124. Huang, M., Pascal, T. A., Kim, H., Goddard, W. A. & Greer, J. R. Electronic−Mechanical Coupling in Graphene from in situ Nanoindentation Experiments and Multiscale Atomistic Simulations. *Nano Lett.* **11**, 1241–1246 (2011).
125. Metzger, C. *et al.* Biaxial Strain in Graphene Adhered to Shallow Depressions. *Nano Lett.* **10**, 6–10 (2010).

126. Smith, A. D. *et al.* Piezoresistive Properties of Suspended Graphene Membranes under Uniaxial and Biaxial Strain in Nanoelectromechanical Pressure Sensors. *ACS Nano* **10**, 9879–9886 (2016).
127. Bousige, C. *et al.* Biaxial Strain Transfer in Supported Graphene. *Nano Lett.* **17**, 21–27 (2017).
128. Shu, Y. *et al.* Strain engineering on the electronic properties and interface contact of graphene/GeN3 van der Waals heterostructure. *Applied Surface Science* **604**, 154540 (2022).
129. Chen, L. *et al.* Electronic properties and interfacial contact of graphene/$CrSiTe_3$ van der Waals heterostructures. *Phys. Chem. Chem. Phys.* **24**, 4280–4286 (2022).
130. Lee, J.-K. *et al.* Modification of Electrical Properties of Graphene by Substrate-Induced Nanomodulation. *Nano Lett.* **13**, 3494–3500 (2013).
131. Zhang, Y., Kim, Y., Gilbert, M. J. & Mason, N. Electronic transport in a two-dimensional superlattice engineered via self-assembled nanostructures. *npj 2D Mater Appl* **2**, 31 (2018).
132. Kang, D.-H. *et al.* Pseudo-magnetic field-induced slow carrier dynamics in periodically strained graphene. *Nat Commun* **12**, 5087 (2021).
133. Pereira, V. M., Ribeiro, R. M., Peres, N. M. R. & Castro Neto, A. H. Optical properties of strained graphene. *EPL* **92**, 67001 (2010).
134. Yoon, D., Son, Y.-W. & Cheong, H. Strain-Dependent Splitting of the Double-Resonance Raman Scattering Band in Graphene. *Phys. Rev. Lett.* **106**, 155502 (2011).
135. Lee, J. E., Ahn, G., Shim, J., Lee, Y. S. & Ryu, S. Optical separation of mechanical strain from charge doping in graphene. *Nat Commun* **3**, 1024 (2012).
136. Xu, P. *et al.* Atomic control of strain in freestanding graphene. *Phys. Rev. B* **85**, 121406 (2012).
137. Lit, J. van der, Jacobse, P. H., Vanmaekelbergh, D. & Swart, I. Bending and buckling of narrow armchair graphene nanoribbons via STM manipulation. *New J. Phys.* **17**, 053013 (2015).
138. Juo, J.-Y. *et al.* In-situ atomic level observation of the strain response of graphene lattice. *Sci Rep* **13**, 2451 (2023).
139. Gorbachev, R. V. *et al.* Detecting topological currents in graphene superlattices. *Science* **346**, 448–451 (2014).
140. Komatsu, K. *et al.* Observation of the quantum valley Hall state in ballistic graphene superlattices. *Sci. Adv.* **4**, eaaq0194 (2018).
141. Plimpton, S. Fast parallel algorithms for short-range molecular dynamics. *Journal of Computational Physics* **117**, 1–19 (1995).
142. Stuart, S. J., Tutein, A. B. & Harrison, J. A. A reactive potential for hydrocarbons with intermolecular interactions. *The Journal of Chemical Physics* **112**, 6472–6486 (2000).
143. Hsu, C.-C., Teague, M. L., Wang, J.-Q. & Yeh, N.-C. Nanoscale strain engineering of giant pseudo-magnetic fields, valley polarization, and topological channels in graphene. *Sci. Adv.* **6**, eaat9488 (2020).

144. Shearer, C. J., Slattery, A. D., Stapleton, A. J., Shapter, J. G. & Gibson, C. T. Accurate thickness measurement of graphene. *Nanotechnology* **27**, 125704 (2016).
145. Liu, F., Ming, P. & Li, J. Ab initio calculation of ideal strength and phonon instability of graphene under tension. *Phys. Rev. B* **76**, 064120 (2007).
146. Wei, Y. & Yang, R. Nanomechanics of graphene. *National Science Review* **6**, 324–348 (2019).
147. Cadelano, E., Palla, P. L., Giordano, S. & Colombo, L. Nonlinear Elasticity of Monolayer Graphene. *Phys. Rev. Lett.* **102**, 235502 (2009).
148. Wei, X., Fragneaud, B., Marianetti, C. A. & Kysar, J. W. Nonlinear elastic behavior of graphene: Ab initio calculations to continuum description. *Phys. Rev. B* **80**, 205407 (2009).
149. Zhao, H., Min, K. & Aluru, N. R. Size and Chirality Dependent Elastic Properties of Graphene Nanoribbons under Uniaxial Tension. *Nano Lett.* **9**, 3012–3015 (2009).
150. Cao, K. *et al.* Elastic straining of free-standing monolayer graphene. *Nat Commun* **11**, 284 (2020).
151. Ramezani Masir, M., Moldovan, D. & Peeters, F. M. Pseudo magnetic field in strained graphene: Revisited. *Solid State Communications* **175–176**, 76–82 (2013).
152. Shearer, C. J., Slattery, A. D., Stapleton, A. J., Shapter, J. G. & Gibson, C. T. Accurate thickness measurement of graphene. *Nanotechnology* **27**, 125704 (2016).
153. Park, A. *et al.* Strongly Enhanced Electronic Bandstructure Renormalization by Light in Nanoscale Strained Regions of Monolayer MoS_2 /Au(111) Heterostructures. *ACS Nano* **18**, 29618–29635 (2024).
154. Levy, N. *et al.* Strain-Induced Pseudo–Magnetic Fields Greater Than 300 Tesla in Graphene Nanobubbles. *Science* **329**, 544–547 (2010).
155. Giambastiani, D., Colangelo, F., Tredicucci, A., Roddaro, S. & Pitanti, A. Electron localization in periodically strained graphene. *Journal of Applied Physics* **131**, 085103 (2022).
156. Aktor, T., Garcia, J. H., Roche, S., Jauho, A.-P. & Power, S. R. Valley Hall effect and nonlocal resistance in locally gapped graphene. *Phys. Rev. B* **103**, 115406 (2021).
157. Wang, H., Wu, Y., Cong, C., Shang, J. & Yu, T. Hysteresis of Electronic Transport in Graphene Transistors. *ACS Nano* **4**, 7221–7228 (2010).
158. Milovanović, S. P. & Peeters, F. M. Strained graphene Hall bar. *J. Phys.: Condens. Matter* **29**, 075601 (2017).
159. Mak, K. F., McGill, K. L., Park, J. & McEuen, P. L. The valley Hall effect in MoS2 transistors. *Science* **344**, 1489–1492 (2014).
160. Yamamoto, M., Shimazaki, Y., Borzenets, I. V. & Tarucha, S. Valley Hall Effect in Two-Dimensional Hexagonal Lattices. *J. Phys. Soc. Jpn.* **84**, 121006 (2015).
161. Shimazaki, Y. *et al.* Generation and detection of pure valley current by electrically induced Berry curvature in bilayer graphene. *Nature Phys* **11**, 1032–1036 (2015).
162. Hsu, C.-C. Physics and Applications of Graphene-based Nanostructures and Nano-meta Materials. (California Institute of Technology, 2020).

163. Guinea, F., Katsnelson, M. I. & Geim, A. K. Energy gaps and a zero-field quantum Hall effect in graphene by strain engineering. *Nature Phys* **6**, 30–33 (2010).
164. Milovanović, S. P., Anđelković, M., Covaci, L. & Peeters, F. M. Band flattening in buckled monolayer graphene. *Phys. Rev. B* **102**, 245427 (2020).
165. Xiao, D., Yao, W. & Niu, Q. Valley-Contrasting Physics in Graphene: Magnetic Moment and Topological Transport. *Phys. Rev. Lett.* **99**, 236809 (2007).
166. Fogler, M. M., Guinea, F. & Katsnelson, M. I. Pseudomagnetic Fields and Ballistic Transport in a Suspended Graphene Sheet. *Phys. Rev. Lett.* **101**, 226804 (2008).
167. Vozmediano, M. A. H., Katsnelson, M. I. & Guinea, F. Gauge fields in graphene. *Physics Reports* **496**, 109–148 (2010).
168. Ando, T. Theory of Valley Hall Conductivity in Graphene with Gap. *J. Phys. Soc. Jpn.* **84**, 114705 (2015).
169. Milovanović, S. P. & Peeters, F. M. Strain controlled valley filtering in multi-terminal graphene structures. *Appl. Phys. Lett.* **109**, 203108 (2016).
170. Guinea, F., Katsnelson, M. I. & Geim, A. K. Energy gaps and a zero-field quantum Hall effect in graphene by strain engineering. *Nature Phys* **6**, 30–33 (2010).
171. Kang, D.-H. *et al.* Pseudo-magnetic field-induced slow carrier dynamics in periodically strained graphene. *Nat Commun* **12**, 5087 (2021).
172. Komatsu, K. *et al.* Observation of the quantum valley Hall state in ballistic graphene superlattices. *Sci. Adv.* **4**, eaaq0194 (2018).
173. Jiang, Z., Zhang, Y., Tan, Y.-W., Stormer, H. L. & Kim, P. Quantum Hall effect in graphene. *Solid State Communications* **143**, 14–19 (2007).
174. Büttiker, M. Four-Terminal Phase-Coherent Conductance. *Phys. Rev. Lett.* **57**, 1761–1764 (1986).
175. Tan, Y.-W., Zhang, Y., Stormer, H. L. & Kim, P. Temperature dependent electron transport in graphene. *Eur. Phys. J. Spec. Top.* **148**, 15–18 (2007).
176. Tan, Y.-W. *et al.* Measurement of Scattering Rate and Minimum Conductivity in Graphene. *Phys. Rev. Lett.* **99**, 246803 (2007).
177. Papaj, M. & Fu, L. Magnus Hall Effect. *Phys. Rev. Lett.* **123**, 216802 (2019).
178. Wang, Y. *et al.* Van der Waals contacts between three-dimensional metals and two-dimensional semiconductors. *Nature* **568**, 70–74 (2019).
179. Uchino, K. *Ferroelectric Devices*. (CRC Press, 2018).
180. Morozovska, A. N., Eliseev, E. A., Svechnikov, G. S. & Kalinin, S. V. Pyroelectric response of ferroelectric nanowires: Size effect and electric energy harvesting. *Journal of Applied Physics* **108**, 042009 (2010).
181. Chai, X. *et al.* Nonvolatile ferroelectric field-effect transistors. *Nat Commun* **11**, 2811 (2020).
182. Si, M. *et al.* A ferroelectric semiconductor field-effect transistor. *Nat Electron* **2**, 580–586 (2019).

183. Peng, Y. *et al.* Exploiting the Bulk Photovoltaic Effect in a 2D Trilayered Hybrid Ferroelectric for Highly Sensitive Polarized Light Detection. *Angewandte Chemie International Edition* **59**, 3933–3937 (2020).
184. Chang, K. *et al.* Discovery of robust in-plane ferroelectricity in atomic-thick SnTe. *Science* **353**, 274–278 (2016).
185. Shi, P.-P. *et al.* Symmetry breaking in molecular ferroelectrics. *Chem. Soc. Rev.* **45**, 3811–3827 (2016).
186. Shirodkar, S. N. & Waghmare, U. V. Emergence of Ferroelectricity at a Metal-Semiconductor Transition in a 1 T Monolayer of MoS 2. *Phys. Rev. Lett.* **112**, 157601 (2014).
187. Lipatov, A. *et al.* Direct observation of ferroelectricity in two-dimensional MoS2. *npj 2D Mater Appl* **6**, 18 (2022).
188. Yuan, S. *et al.* Room-temperature ferroelectricity in MoTe2 down to the atomic monolayer limit. *Nat Commun* **10**, 1775 (2019).
189. Yang, T. H. *et al.* Ferroelectric transistors based on shear-transformation-mediated rhombohedral-stacked molybdenum disulfide. *Nat Electron* **7**, 29–38 (2023).
190. Fei, Z. *et al.* Ferroelectric switching of a two-dimensional metal. *Nature* **560**, 336–339 (2018).
191. Weston, A. *et al.* Interfacial ferroelectricity in marginally twisted 2D semiconductors. *Nat. Nanotechnol.* **17**, 390–395 (2022).
192. Wang, X. *et al.* Interfacial ferroelectricity in rhombohedral-stacked bilayer transition metal dichalcogenides. *Nat. Nanotechnol.* **17**, 367–371 (2022).
193. He, G. *et al.* Thermally Assisted Nonvolatile Memory in Monolayer MoS_2 Transistors. *Nano Lett.* **16**, 6445–6451 (2016).
194. Kaushik, N. *et al.* Reversible hysteresis inversion in MoS2 field effect transistors. *npj 2D Mater Appl* **1**, 1–9 (2017).
195. Di Bartolomeo, A. *et al.* Hysteresis in the transfer characteristics of MoS_2 transistors. *2D Mater.* **5**, 015014 (2017).
196. Late, D. J., Liu, B., Matte, H. S. S. R., Dravid, V. P. & Rao, C. N. R. Hysteresis in Single-Layer MoS_2 Field Effect Transistors. *ACS Nano* **6**, 5635–5641 (2012).
197. Li, T., Du, G., Zhang, B. & Zeng, Z. Scaling behavior of hysteresis in multilayer MoS2 field effect transistors. *Applied Physics Letters* **105**, 093107 (2014).
198. Shu, J. *et al.* The intrinsic origin of hysteresis in MoS_2 field effect transistors. *Nanoscale* **8**, 3049–3056 (2016).
199. Li, H. *et al.* From Bulk to Monolayer MoS2: Evolution of Raman Scattering. *Advanced Functional Materials* **22**, 1385–1390 (2012).
200. Splendiani, A. *et al.* Emerging Photoluminescence in Monolayer MoS2. *Nano Lett.* **10**, 1271–1275 (2010).
201. Allain, A., Kang, J., Banerjee, K. & Kis, A. Electrical contacts to two-dimensional semiconductors. *Nature Mater* **14**, 1195–1205 (2015).

202. Shen, P.-C. *et al.* Ultralow contact resistance between semimetal and monolayer semiconductors. *Nature* **593**, 211–217 (2021).
203. Lan, Y.-W. *et al.* Scalable fabrication of a complementary logic inverter based on MoS_2 fin-shaped field effect transistors. *Nanoscale Horiz.* **4**, 683–688 (2019).
204. Radisavljevic, B., Radenovic, A., Brivio, J., Giacometti, V. & Kis, A. Single-layer MoS2 transistors. *Nature Nanotech* **6**, 147–150 (2011).
205. Novoselov, K. S. *et al.* Two-dimensional atomic crystals. *Proceedings of the National Academy of Sciences* **102**, 10451–10453 (2005).
206. Radisavljevic, B. & Kis, A. Mobility engineering and a metal–insulator transition in monolayer MoS2. *Nature Mater* **12**, 815–820 (2013).
207. Li, W. *et al.* Approaching the quantum limit in two-dimensional semiconductor contacts. *Nature* **613**, 274–279 (2023).
208. Yu, Z. *et al.* Toward High-mobility and Low-power 2D MoS2 Field-effect Transistors. in *2018 IEEE International Electron Devices Meeting (IEDM)* 22.4.1-22.4.4 (IEEE, San Francisco, CA, 2018). doi:10.1109/IEDM.2018.8614644.
209. Li, Q. *et al.* Enhanced Valley Zeeman Splitting in Fe-Doped Monolayer MoS_2. *ACS Nano* **14**, 4636–4645 (2020).
210. Marinov, K., Avsar, A., Watanabe, K., Taniguchi, T. & Kis, A. Resolving the spin splitting in the conduction band of monolayer MoS2. *Nat Commun* **8**, 1938 (2017).
211. Liu, X. *et al.* Charge–Ferroelectric Transition in Ultrathin $Na_{0.5}Bi_{4.5}Ti_4O_{15}$ Flakes Probed via a Dual-Gated Full van der Waals Transistor. *Adv. Mater.* **32**, 2004813 (2020).
212. Huang, L. F., Gong, P. L. & Zeng, Z. Correlation between structure, phonon spectra, thermal expansion, and thermomechanics of single-layer MoS 2. *Phys. Rev. B* **90**, 045409 (2014).
213. Taube, A. *et al.* Temperature-Dependent Nonlinear Phonon Shifts in a Supported MoS_2 Monolayer. *ACS Appl. Mater. Interfaces* **6**, 8959–8963 (2014).
214. Thripuranthaka, M., Kashid, R. V., Sekhar Rout, C. & Late, D. J. Temperature dependent Raman spectroscopy of chemically derived few layer MoS_2 and WS_2 nanosheets. *Appl. Phys. Lett.* **104**, 081911 (2014).
215. Lee, K.-Y. *et al.* Raman imaging of strained bubbles and their effects on charge doping in monolayer WS2 encapsulated with hexagonal boron nitride. *Applied Surface Science* **604**, 154489 (2022).
216. Geng, T. *et al.* A Novel Atomically Resolved Scanning Tunneling Microscope Capable of Working in Cryogen-Free Superconducting Magnet. *Micromachines* **14**, 637 (2023).
217. Abbas, G. *et al.* Recent Advances in Twisted Structures of Flatland Materials and Crafting Moiré Superlattices. *Advanced Functional Materials* **30**, 2000878 (2020).
218. Rice, C. *et al.* Raman-scattering measurements and first-principles calculations of strain-induced phonon shifts in monolayer MoS 2. *Phys. Rev. B* **87**, 081307 (2013).
219. Sohier, T. *et al.* Enhanced Electron-Phonon Interaction in Multivalley Materials. *Phys. Rev. X* **9**, 031019 (2019).

220. Khamrui, S., Bharti, K., Goldfarb, D., Das, T. & Banerjee, D. Strain-driven Charge Localisation and Spin Dynamics of Paramagnetic Defects in S-deficit 2H-MoS2 Nanocrystals. *arXiv* **2312.12805**, (2023).
221. Morozovska, A. N. *et al.* Flexoinduced ferroelectricity in low-dimensional transition metal dichalcogenides. *Phys. Rev. B* **102**, 075417 (2020).
222. Luo, S. *et al.* Formation of ripples in atomically thin MoS2 and local strain engineering of electrostatic properties. *Nanotechnology* **26**, 105705 (2015).
223. Wang, W., Yang, C., Bai, L., Li, M. & Li, W. First-Principles Study on the Structural and Electronic Properties of Monolayer MoS2 with S-Vacancy under Uniaxial Tensile Strain. *Nanomaterials* **8**, 74 (2018).
224. Sevik, C. Assessment on lattice thermal properties of two-dimensional honeycomb structures: Graphene, h-BN, h-MoS2, and h-MoSe2. *Phys. Rev. B* **89**, 035422 (2014).
225. Quereda, J., Castellanos-Gomez, A., Agraït, N. & Rubio-Bollinger, G. Single-layer MoS2 roughness and sliding friction quenching by interaction with atomically flat substrates. *Applied Physics Letters* **105**, 053111 (2014).
226. Piprek, J. *Optoelectronic Devices: Advanced Simulation and Analysis*. (Springer, New York, 2005).
227. Ostroverkhova, O. Organic Optoelectronic Materials: Mechanisms and Applications. *Chem. Rev.* **116**, 13279–13412 (2016).
228. Quinteiro, G. F., Schmidt-Kaler, F. & Schmiegelow, C. T. Twisted-Light–Ion Interaction: The Role of Longitudinal Fields. *Phys. Rev. Lett.* **119**, 253203 (2017).
229. Zhan, Q. Trapping metallic Rayleigh particles with radial polarization. *Opt. Express* **12**, 3377 (2004).
230. Gibson, G. *et al.* Free-space information transfer using light beams carrying orbital angular momentum. *Opt. Express* **12**, 5448 (2004).
231. Erhard, M., Fickler, R., Krenn, M. & Zeilinger, A. Twisted photons: new quantum perspectives in high dimensions. *Light Sci Appl* **7**, 17146–17146 (2017).
232. Peng, Z., Chen, X., Fan, Y., Srolovitz, D. J. & Lei, D. Strain engineering of 2D semiconductors and graphene: from strain fields to band-structure tuning and photonic applications. *Light Sci Appl* **9**, 190 (2020).
233. Hu, Z. *et al.* Two-dimensional transition metal dichalcogenides: interface and defect engineering. *Chem. Soc. Rev.* **47**, 3100–3128 (2018).
234. Hossen, M. F., Shendokar, S. & Aravamudhan, S. Defects and Defect Engineering of Two-Dimensional Transition Metal Dichalcogenide (2D TMDC) Materials. *Nanomaterials* **14**, 410 (2024).
235. Ho, Y.-L. *et al.* Finite-Area Membrane Metasurfaces for Enhancing Light-Matter Coupling in Monolayer Transition Metal Dichalcogenides. *ACS Nano* **18**, 24173–24181 (2024).
236. Li, Z. *et al.* Tailoring MoS $_2$ Exciton–Plasmon Interaction by Optical Spin–Orbit Coupling. *ACS Nano* **11**, 1165–1171 (2017).

237. Lin, W. *et al.* Electrically Tunable and Dramatically Enhanced Valley-Polarized Emission of Monolayer WS_2 at Room Temperature with Plasmonic Archimedes Spiral Nanostructures. *Advanced Materials* **34**, 2104863 (2022).
238. Premasiri, K. & Gao, X. P. A. Tuning spin–orbit coupling in 2D materials for spintronics: a topical review. *J. Phys.: Condens. Matter* **31**, 193001 (2019).
239. Ominato, Y., Fujimoto, J. & Matsuo, M. Valley-Dependent Spin Transport in Monolayer Transition-Metal Dichalcogenides. *Phys. Rev. Lett.* **124**, 166803 (2020).
240. Garadkar, K. M. *et al.* MoS2: Preparation and their characterization. *Journal of Alloys and Compounds* **487**, 786–789 (2009).
241. Back, P. *et al.* Giant Paramagnetism-Induced Valley Polarization of Electrons in Charge-Tunable Monolayer MoSe 2. *Phys. Rev. Lett.* **118**, 237404 (2017).
242. Sun, L. *et al.* Spin-Orbit Splitting in Single-Layer MoS 2 Revealed by Triply Resonant Raman Scattering. *Phys. Rev. Lett.* **111**, 126801 (2013).
243. Eginligil, M. *et al.* Dichroic spin–valley photocurrent in monolayer molybdenum disulphide. *Nat Commun* **6**, 7636 (2015).
244. Kioseoglou, G. *et al.* Valley polarization and intervalley scattering in monolayer MoS_2. *Appl. Phys. Lett.* **101**, 221907 (2012).
245. Li, Z. *et al.* Tailoring MoS_2 Valley-Polarized Photoluminescence with Super Chiral Near-Field. *Advanced Materials* **30**, 1801908 (2018).
246. Peter, L. M. Chapter 8 Photocurrent Spectroscopy. in *Comprehensive Chemical Kinetics* vol. 29 353–383 (Elsevier, 1989).
247. Wu, C.-C. *et al.* Elucidating the Photoresponse of Ultrathin MoS_2 Field-Effect Transistors by Scanning Photocurrent Microscopy. *J. Phys. Chem. Lett.* **4**, 2508–2513 (2013).
248. Peng, K. *et al.* Probing the Dark-Exciton States of a Single Quantum Dot Using Photocurrent Spectroscopy in a Magnetic Field. *Phys. Rev. Applied* **8**, 064018 (2017).
249. Engström, D., Persson, M., Bengtsson, J. & Goksör, M. Calibration of spatial light modulators suffering from spatially varying phase response. *Opt. Express* **21**, 16086 (2013).
250. Fritsch, F. N. & Butland, J. A Method for Constructing Local Monotone Piecewise Cubic Interpolants. *SIAM J. Sci. and Stat. Comput.* **5**, 300–304 (1984).
251. Hao, D. *et al.* Magnetic Field-Induced Polar Order in Monolayer Molybdenum Disulfide Transistors. *Advanced Materials* 2411393 (2024) doi:10.1002/adma.202411393.
252. Simbulan, K. B. *et al.* Twisted Light-Enhanced Photovoltaic Effect. *ACS Nano* **15**, 14822–14829 (2021).
253. Vaquero, D., Salvador-Sánchez, J., Clericò, V., Diez, E. & Quereda, J. The Low-Temperature Photocurrent Spectrum of Monolayer MoSe2: Excitonic Features and Gate Voltage Dependence. *Nanomaterials* **12**, 322 (2022).

254. Wu, C.-C. *et al.* Elucidating the Photoresponse of Ultrathin MoS_2 Field-Effect Transistors by Scanning Photocurrent Microscopy. *J. Phys. Chem. Lett.* **4**, 2508–2513 (2013).
255. Yamaguchi, H. *et al.* Spatially Resolved Photoexcited Charge-Carrier Dynamics in Phase-Engineered Monolayer MoS_2. *ACS Nano* **9**, 840–849 (2015).
256. Singha, S. S., Nandi, D., Bhattacharya, T. S., Mondal, P. K. & Singha, A. Photoluminescence modulation due to conversion of trions to excitons and plasmonic interaction in MoS2-metal NPs hybrid structures. *Journal of Alloys and Compounds* **723**, 722–728 (2017).
257. Lee, B. *et al.* Electrical Tuning of Exciton–Plasmon Polariton Coupling in Monolayer MoS_2 Integrated with Plasmonic Nanoantenna Lattice. *Nano Lett.* **17**, 4541–4547 (2017).
258. Park, Y., Choi, S. H., Lee, G., Yang, W. & Im, H. Effects of contact material on complex excitonic behaviour of monolayer MoS2. *Optical Materials* **84**, 870–873 (2018).
259. Hong, C. *et al.* Ultrafast hot carrier extraction and diffusion at the MoS_2 /Au van der Waals electrode interface. *Sci. Adv.* **11**, eadr1534 (2025).
260. Stier, A. V., McCreary, K. M., Jonker, B. T., Kono, J. & Crooker, S. A. Exciton diamagnetic shifts and valley Zeeman effects in monolayer WS2 and MoS2 to 65 Tesla. *Nat Commun* **7**, 10643 (2016).
261. Xu, X., Yao, W., Xiao, D. & Heinz, T. F. Spin and pseudospins in layered transition metal dichalcogenides. *Nature Phys* **10**, 343–350 (2014).
262. Mak, K. F., He, K., Shan, J. & Heinz, T. F. Control of valley polarization in monolayer MoS2 by optical helicity. *Nature Nanotech* **7**, 494–498 (2012).
263. Stier, A. V., McCreary, K. M., Jonker, B. T., Kono, J. & Crooker, S. A. Exciton diamagnetic shifts and valley Zeeman effects in monolayer WS2 and MoS2 to 65 Tesla. *Nat Commun* **7**, 10643 (2016).
264. Ridolfi, E., Le, D., Rahman, T. S., Mucciolo, E. R. & Lewenkopf, C. H. A tight-binding model for MoS_2 monolayers. *J. Phys.: Condens. Matter* **27**, 365501 (2015).
265. Kadantsev, E. S. & Hawrylak, P. Electronic structure of a single MoS2 monolayer. *Solid State Communications* **152**, 909–913 (2012).
266. Li, Z. *et al.* Momentum-Dark Intervalley Exciton in Monolayer Tungsten Diselenide Brightened *via* Chiral Phonon. *ACS Nano* **13**, 14107–14113 (2019).
267. Quinteiro, G. F. & Tamborenea, P. I. Theory of the optical absorption of light carrying orbital angular momentum by semiconductors. *Europhys. Lett.* **85**, 47001 (2009).
268. Feng, Y.-J. *et al.* Twisted Light-Induced Photocurrent in a Silicon Nanowire Field-Effect Transistor. *ACS Nano* **16**, 9297–9303 (2022).
269. Konzelmann, A. M., Krüger, S. O. & Giessen, H. Interaction of orbital angular momentum light with Rydberg excitons: Modifying dipole selection rules. *Phys. Rev. B* **100**, 115308 (2019).

270. Furchi, M. M., Polyushkin, D. K., Pospischil, A. & Mueller, T. Mechanisms of Photoconductivity in Atomically Thin MoS_2. *Nano Lett.* **14**, 6165–6170 (2014).
271. Simbulan, K. B. *et al.* Twisted Light-Enhanced Photovoltaic Effect. *ACS Nano* **15**, 14822–14829 (2021).
272. Shimazu, Y., Murata, K. & Toda, S. Anomalous hysteresis below 1 K in the transfer characteristics of MoS2 field effect transistors. *Jpn. J. Appl. Phys.* **54**, 031201 (2015).
273. Xie, J. *et al.* Analysis of Schottky barrier heights and reduced Fermi-level pinning in monolayer CVD-grown MoS2 field-effect-transistors. *Nanotechnology* **33**, 225702 (2022).
274. Lee, J. *et al.* Electrical role of sulfur vacancies in MoS2: Transient current approach. *Applied Surface Science* **613**, 155900 (2023).
275. Noh, J.-Y., Kim, H. & Kim, Y.-S. Stability and electronic structures of native defects in single-layer MoS 2. *Phys. Rev. B* **89**, 205417 (2014).
276. Jadwiszczak, J. *et al.* MoS_2 Memtransistors Fabricated by Localized Helium Ion Beam Irradiation. *ACS Nano* **13**, 14262–14273 (2019).
277. Thool, A. S., Roy, S., Misra, A. & Chakrabarti, B. Controllable Defect Engineering in 2D-MoS_2 for high-performance, threshold switching memristive devices. in *2022 Device Research Conference (DRC)* 1–2 (IEEE, Columbus, OH, USA, 2022). doi:10.1109/DRC55272.2022.9855777.
278. Spetzler, B., Geng, Z., Rossnagel, K., Ziegler, M. & Schwierz, F. Lateral 2D TMDC Memristors – Experiment and Modeling. in *2022 IEEE 16th International Conference on Solid-State & Integrated Circuit Technology (ICSICT)* 1–3 (IEEE, Nangjing, China, 2022). doi:10.1109/ICSICT55466.2022.9963350.
279. Shevliakova, H. V. *et al.* Flexoelectric and Piezoelectric Coupling in a Bended MoS2 Monolayer. *Symmetry* **13**, 2086 (2021).
280. Xiao, W.-Z., Luo, H.-J. & Xu, L. Elasticity, piezoelectricity, and mobility in two-dimensional BiTeI from a first-principles study. *J. Phys. D: Appl. Phys.* **53**, 245301 (2020).
281. Ma, X. Y. Study of the Electrical Properties of Monolayer MoS_2 Semiconductor. *AMR* **651**, 193–197 (2013).